Thèse

présentée à

UNIVERSITE LILLE - SCIENCES ET TECHNOLOGIES

Ecole Doctorale Sciences Pour l'Ingénieur

Université Lille Nord-de-France

en vue de l'obtention du titre de Docteur dans la spécialité

Automatique, Génie Informatique, Traitement du Signal et des Images

Par

Sara MOSLEH

Processus de morphotype adaptatif pour un ajustement ergonomique optimal et une modélisation du confort thermique des vêtements pour les personnes souffrant d'un handicap rachidien

Codirigée par Prof. Pascal Bruniaux et Prof. Yan Chen

soutenue le 14 Septembre 2021

JURY

		Président du jury
Imed KACEM	Professeur, Université de Lorraine, France	Rapporteur
Jun LI	Professeur, Université de Shanghai, Chine	Rapporteur
Yan CHEN	Professeur, Université de Soochow, Chine	Directeur
Pascal BRUNIAUX	Professeur, Université de Lille, France	Directeur
Guillaume TARTARE	Maître de conférences, Université de Lille,France	Examinateur
Jiazhen HE	Maître de conférences, Université de Soochow, Chine	Examinateur

Thesis

presented to

LILLE UNIVERSITY - SCIENCES AND TECHNOLOGIES

Doctoral School of Engineering Sciences

Lille Nord-de-France UniversityWith A View To Obtaining The Title Of Doctor In The Specialty Automatic Control, Computer Engineering, Signal And Image Processing

By

Sara MOSLEH

Adaptive morphotype process for optimal ergonomic fit and thermal comfort modelling of garments for persons with spinal disabilities

Directed by Prof. Pascal Bruniaux and Prof. Yan Chen

14 septembre 2021

JURY		
		Jury President
Imed KACEM	Professor, University of Lorraine, France	Reviewer
Jun LI	Professor, University of Shanghai, China	Reviewer
Yan CHEN	Professor, University of Soochow, China	Director
Pascal BRUNIAUX	Professor, University of Lille, France	Director
Guillaume TARTARE	Lecturer, University of Lille, France	Examiner
Jiazhen HE	Lecturer, University of Soochow, China	Examiner

Adaptive Morphotype Process for Optimal Ergonomic Fit and Thermal Comfort Modelling of Garments For Persons With Spinal Disabilities

Abstract

This research aims to design a garment for people with disabilities in terms of ergonomic and thermal comfort. A new design technique for developing a 3D adaptive global garment model from the human skeleton and the anatomical shape of the person is proposed using 3D scanning technologies.

This overall model is made up of a skeleton model, a garment model connected to each other by the person's body shape, and a thermal regulation model. All the parameters of the overall model make it possible to adapt it to the person's skeleton, then to these body shapes in order to produce a comfortable and efficient garment.

The skeleton model has the power to adjust to the morphology and dimensions of the bones of the spine and thorax, to control the relative positions of these bones in the three characteristic planes: sagittal, coronal and transverse. For the person suffering from scoliosis, it was necessary to accurately detect the 3D path of the spine from the images of an EOS medical scanner. A specific landmark detection model for each vertebra is used to automatically obtain the position of the vertebrae calculated according to the height and the 3D polar angle of each vertebra. The bones of the thorax follow the path of the vertebrae.

Once the skeletal model has been adjusted to the person, it then makes it possible to detect the anthropometric points and the morphological contours of the latter. For this, the model was placed in the body shape of the person resulting from a 3D body scanner. The position of the morphological contours is given by reference marks connected to the skeleton. These strong links with the skeleton are essential so that the garment automatically adapts to the evolution of the patient's pathology over time. At this stage, we were able to connect our graphic model of the garment, integrating the 3D ease of the garment, to these anthropometric and morphological data.

The garment's 3D ease control is essential because it manages the air space between the body and the garment in our thermal regulation model. In the context of thermal comfort, a clothing system consists of the human body, a layer of air space under the clothing, a layer of fabric, and a

boundary layer adjacent to the fabric. In addition, for a complete system, one must consider the heat transfer from the skin to the environment, influenced by the thermoregulation of the human body, air gap, tissue and environmental conditions. The thermal regulation model we have proposed can predict the rate of heat transfer and temperature in the garment, skin and air space, which by optimizing the air space allows us to maintain the body in a situation of thermal comfort.

Processus de morphotype adaptatif pour un ajustement ergonomique optimal et une modélisation du confort thermique des vêtements pour les personnes souffrant d'un handicap rachidien.

Résumé

Ces travaux de recherche visent à concevoir un vêtement pour personnes handicapées en termes de confort ergonomique et thermique. Une nouvelle technique de conception pour développer un modèle global 3D adaptatif de vêtement à partir du squelette humain et de l'enveloppe anatomique de la personne est proposée en utilisant des technologies de numérisation 3D.

Ce modèle global est composé d'un modèle de squelette, d'un modèle de vêtement connectés entre eux par l'enveloppe corporelle de la personne, et d'un modèle de régulation thermique. L'ensemble des paramètres du modèle global permettent de l'adapter au squelette de la personne, puis à ces formes corporelles afin de produire un vêtement confortable et performant.

Le modèle de squelette a le pouvoir de s'ajuster à la morphologie et aux dimensions des os de la colonne vertébrale et du thorax, de contrôler les positions relatives de ces os dans les trois plans caractéristiques : sagittal, coronal et transversal. La personne souffrant de scoliose, il a été nécessaire de détecter avec précision le parcours 3D de la colonne vertébrale à partir des images d'un scanner médical EOS. Un modèle de détection de point de repère spécifique à chaque vertèbre est utilisé pour obtenir automatiquement la position des vertèbres calculée selon la hauteur et l'angle polaire 3D de chaque vertèbre. Les os du thorax suivent le parcours des vertèbres.

Une fois le modèle du squelette ajusté à la personne, il permet alors de détecter les points anthropométriques et les contours morphologiques de celle-ci. Pour cela, le modèle a été placé dans l'enveloppe corporel de la personne issue d'un scanner 3D humain. La position des contours morphologiques est donnée par des repères reliés au squelette. Ces liens forts avec le squelette sont essentiels pour que le vêtement s'adapte automatiquement à l'évolution de la pathologie du patient dans le temps. A ce stade, nous avons pu connecter notre modèle graphique de vêtement, intégrant l'aisance 3D du vêtement, à ces données anthropométriques et morphologiques.

Le contrôle de l'aisance 3D du vêtement est essentiel car il gère l'espace d'air entre le corps et le vêtement dans notre modèle de régulation thermique. Dans un contexte de confort thermique, un système de vêtements se compose du corps humain, d'une couche d'espace d'air sous les vêtements, d'une couche de tissu et d'une couche limite adjacente au tissu. De plus, pour un système complet, il faut considérer le transfert de chaleur de la peau à l'environnement, influencé par la thermorégulation du corps humain, l'entrefer, le tissu et les conditions environnementales. Le modèle de régulation thermique que nous avons proposé peut prédire le taux de transfert de chaleur et la température dans le vêtement, la peau et la lame d'air, ce qui, en optimisant la lame d'air, nous permet de maintenir le corps dans une situation de confort thermique.

Mot clé *: Scoliose, modèle adaptatif 3D de squelette, modèle 3D de vêtement, détection de vertèbres, tolérance 3D d'aisance, confort thermique, modèle thermorégulateur.*

Processo di morfotipo adattivo per una vestibilità ergonomica ottimale e modellazione del comfort termico di indumenti per persone con disabilità spinali

Riassunto

Questa ricerca mira a progettare un capo per persone con disabilità in termini di comfort ergonomico e termico. Viene proposta una nuova tecnica di progettazione per lo sviluppo di un modello di indumento globale adattivo dallo scheletro umano e dall'involucro anatomico della persona utilizzando tecnologie di scansione 3D.

Questo modello generale è composto da un modello scheletro, un modello di indumento collegati tra loro dall'involucro corporeo della persona e un modello di regolazione termica. Tutti i parametri del modello complessivo consentono di adattarlo allo scheletro della persona, quindi a queste forme del corpo per produrre un capo comodo ed efficiente.

Il modello scheletrico ha il potere di adattarsi alla morfologia e alle dimensioni delle ossa della colonna vertebrale e del torace, di controllare le posizioni relative di queste ossa nei tre piani caratteristici: sagittale, coronale e trasversale. Per la persona affetta da scoliosi, era necessario rilevare con precisione l'andamento 3D della colonna vertebrale dalle immagini di uno scanner medico EOS. Viene utilizzato un modello di rilevamento del punto di riferimento specifico per le vertebre per ottenere automaticamente la posizione delle vertebre calcolata in base all'altezza e all'angolo polare 3D di ciascuna vertebra. Le ossa del torace seguono il corso delle vertebre.

Il modello dello scheletro, una volta adattato alla persona, permette poi di rilevare i punti antropometrici ei contorni morfologici di quest'ultima. Per questo, il modello è stato collocato nell'involucro corporeo della persona risultante da uno scanner 3D umano. La posizione dei contorni morfologici è data da segni di riferimento collegati allo scheletro. Questi forti legami con lo scheletro sono essenziali affinché l'indumento si adatti automaticamente all'evoluzione della patologia del paziente nel tempo. In questa fase siamo riusciti a collegare il nostro modello grafico del capo, integrando la facilità 3D del capo, a questi dati antropometrici e morfologici.

Parole chiave: *Scoliosi, modello 3D adattivo dello scheletro, modello 3D dell'indumento, rilevamento delle vertebre, indennità di facilitazione, comfort termico, modello termoregolatore.*

用于脊柱残疾人士服装的最佳人体工学合身和热舒适性建模的自适应形态型过程

摘要

这项研究旨在为残疾人设计符合人体工程学和热舒适性的服装。提出了一种使用 3D 扫描技术从人体骨骼和人体解剖学形状开发 3D 自适应全局服装模型的新设计技术。

这个整体模型由骨架模型、通过人的体型相互连接的服装模型和热调节模型组成。整个模型的所有参数都可以使其适应人的骨骼，然后适应这些体型，以生产出舒适高效的服装。

骨骼模型可以根据脊柱和胸部骨骼的形态和尺寸进行调整，控制这些骨骼在矢状面、冠状面和横向三个特征平面上的相对位置。对于脊柱侧弯患者，需要从 EOS 医疗扫描仪的图像中准确检测脊柱的 3D 路径。每个椎骨使用特定的界标检测模型，根据每个椎骨的高度和 3D 极角自动获取计算出的椎骨位置。胸部的骨骼遵循椎骨的路径。

一旦骨骼模型已根据人进行调整，就可以检测人体测量点和后者的形态学轮廓。为此，模型被放置在由 3D 身体扫描仪生成的人的身体形状中。形态轮廓的位置由连接到骨架的参考标记给出。这些与骨骼的紧密联系是必不可少的，因此服装会随着时间的推移自动适应患者病理的演变。在这个阶段，我们能够将服装的图形模型与这些人体测量学和形态学数据连接起来，将服装的 3D 易用性整合在一起。

服装的 3D 缓动控制至关重要，因为它在我们的热调节模型中管理身体和服装之间的空气空间。在热舒适性方面，服装系统由人体、服装下方的空气层、织物层和与织物相邻的边界层组成。此外，对于一个完整的系统，必须考虑从皮肤到环境的热传递，受人体体温调节、气隙、组织和环境条件的影响。我们提出的热调节模型可以预测服装、皮肤和空气空间的热传递率和温度，通过优化空气空间，我们可以使身体保持在热舒适的状态。

关键词：*脊柱侧弯，骨骼 3D 自适应模型，服装 3D 模型，椎骨检测，宽松度，热舒适度，体温调节模型。*

Acknowledgements

Undertaking this PhD has been a truly life-changing experience for me, and it would not have been possible to do without the support and guidance that I received from many people.

I would like to first say a very big thank you to my supervisor Prof. Pascal Bruniaux for all the support and encouragement he gave me, he was more than just a supervisor for me during this period, I could not be luckier to have him as my supervisor, without his guidance and constant feedback this PhD would not have been achievable.

Many thanks also to Dr. Mulat Alubel Abtew who helped me during our many discussions that I should pursue my doctoral degree and who made it possible for me to have my publications with his support .

I gratefully acknowledge the funding received towards my PhD from the European union PhD fellowship. Thanks to Prof. Xianyi Zeng for his hard work during these eight years to manage this program and fellowship.

To my friends, my parents, and my siblings: you put up with me being distracted and missing many events. I am forever grateful for your patience and understanding. I hope to have time now to reconnect with each of you.

Finally, to my partner, Dr. Giuseppe Di Gioia: your love and understanding helped me through the dark times. Without you believing in me, I never would have made it. It is time to celebrate; you earned this degree right along with me.

Sara MOSLEH

12th JULY 2021

Contents

List of Figures

List of Tables

General Introduction

People with disabilities form a social group with unusual morphologies. Scoliosis is a lateral curvature of the spine that often occurs during growth spurts before puberty. While scoliosis can be caused by cerebral palsy and muscular dystrophy, the other cause of scoliosis is unknown. Most cases of scoliosis are mild, but some children develop spinal deformities that worsen as they grow older. Severe scoliosis can be debilitating. The special curve of the spine can reduce the space of the chest and make it difficult for the lungs to function properly. Children with mild scoliosis are usually monitored with X-rays to see if the curve gets worse. In many cases, no treatment is needed. Some children need corset to prevent the curve from getting worse.

Medical clothing products and braces affect the quality of daily life of this group. Having the right clothes can effectively meet the functional, expressive, and aesthetic needs of consumers. General clothing products that do not meet the unique needs of people with unusual morphologies significantly reduce the quality of life and social participation of this group.

Making adapting ready-to-wear garments is strongly required for scoliosis patients. Still, the current design method for the adapted garment can take more time for production and delivery and lead to a harmful aesthetic effect and uncomfortable feeling without considering the garment's ergonomic fit and thermal situation for the human body in different temperatures.

The development of new CAD software, hardware, and other applications supported by the aid of contemporary techniques, including 3D body scanning, 3D human modeling, and 3D garment design for the fashion, were impressive progress in garments technology in these years. In this thesis has been tried to treat the previous methods in terms of adaptation speed and automatization. The proposed procedure is that instead of focusing on the surface of the body by considering the curves of the body, we focused on the skeleton, which plays a vital role in cases of scoliosis. All normal and abnormal curves in the body have logical relationships with the entire skeleton, especially with the vertebrae. A clear overview of the position of the vertebrae in each part and the bones required sufficient knowledge of the anatomy of the skeleton. Thanks to the position and measurement of the vertebrae, the process will be faster than the usual method.

The 3D garment design and virtual try-on garment fit has been an impressive achievement over previous work in predicting 3D ease allowance. In this thesis, ease allowance is linked to

thermal comfort as an effective parameter. This study can be considered as a new methodological concept on optimizing the design of clothing to provide thermal comfort to humans taking into account the physical situation and the environment.

As first in this new process, it was necessary to create a 3D model of the spine having the particularity of adapting to the patient's morphology to model the deformities of the spine. Then, all the parameters of the spine, such as the heights, 3D angular positions, and morphology of vertebrae, the height of disks, defined in the three feature planes: sagittal, coronal, and transverse, are integrated into the 3D model to lead to a result close to the reality.

This model is adjusted with the dimensional and dynamic parameters controlling the 3D evolution of the spine, which comes from EOS imaging of the patient. EOS imaging is a 3D X-Ray imaging system that uses 50 to 80% less radiation than a typical X-Ray. The sterEOS software enables 3D modeling of the bone envelope based on anatomic references defined by the reader and providing specific clinical parameters manually. All these processes have should automatically instead of measuring by sterEOS.

In my thesis, through image processing based on the deep learning system; through an algorithm, each vertebra can be detected to measure. Thus, the data to create the 3D model of the skeleton are available.

To understand the thermal comfort situation for the human body having a thermoregulatory model is required. The thermoregulatory model demonstrates the temperature and wetness of each part of the body in a different environment. To achieve this aim, a multi-node model of thermoregulation is used. This model shows the temperature in 16 parts of the body in four different layers: skin, fat, muscle, and core. One of the important parameters in this model is thermal insulation which is related to ease allowance.

The overall layout of the thesis is organized as follows:

Chapter 1 introduces the problems faced by scoliosis patients, diagnostic, 3D design of skeleton, and thermal comfort solutions. It's going to start by explain about what is the main problem for scoliosis patient, how the garment would effect for bringing the comfort for them in thermal ergonomic and thermal filling. After that there is a review of previous works to design garments for scoliosis and normal people, at the end of this section, we have proposed our idea to

design automatically according to the skeleton. Having a clear view from how we can create 3D model of vertebrae to design garment is important to explain carefully. To create a virtual 3D vertebra obtaining data from x-ray images plays an important role, so through having a good view from previous works and the history of machine learning and machine vision the data issues is solved. The thorax 3D model was so important for connection of vertebrae and acromion points to create garment, at the end of this chapter the previous work to provide thermal comfort is mentioned and the critical parameters of thermal comfort for human body is explained.

Chapter 2 is the general framework and working process of the proposed 3D model of vertebrae. In the beginning the anatomic view of vertebrae is explained well by figure out the difference between each vertebra in each part, after that all steps of creating the 3D vertebrae is explained by detail by dividing each part of vertebrae. At the end, a 3D adaptive model of vertebrae is proposed which is able to be adjusted by x-ray images data.

Chapter 3 is about the diagnostic of scoliosis patients by vertebra detection and analysis. This chapter is going to start by EOS imaging which is used in project and continue about the software which is connected to EOS images to obtain data then we going to explain about the weakness of this methods. In the next section the history of machine learning is explained and how machine vision in this days is effective for diagnostic of diseases in medical fields. At the end, the algorithm of detection of vertebrae is represented and we are going to present how this algorithm is used to calculate all the data automatically.

Chapter 4 is the proposed 3D model of the thorax and its connection with adaptive vertebrae, to integrate acromion points to design garment. This chapter is started by describing the thorax anatomy and ribs, then the method to model the adaptive scapula ribs sternum and clavicula is described, at the end of chapter the thorax model parameterized is proposed.

Chapter 5 is the adaptive garment model. At first, we explain about the analysis of the 2D creation process of the women's block pattern corresponding to previous works and then the analysis of the 3D creation process of the women's block pattern. The critical point in this chapter is the 3D creation process connected with the skeleton from 3D model of the thorax and the detection anthropometric points and morphological curves on the skeleton, and as our result 3D adaptive model of garment with 3D ease allowance.

Chapter 6 is about thermal comfort for human the body by adjusting the ease allowance. A thermoregulatory model for human body is the important point to start in this chapter to calculate temperature and heat transfer for the human body, and in continue the effect of air gap is figure out. At the end of this chapter a model is proposed to calculate the temperature and heat transfer in human body by adding different layers as the garment and also this model is able to predict the temperature of the garment in different part of body.

CHAPTER 1: STATE OF THE ART

In this chapter, we will have a brief overview of each stage of this project. This thesis aims to create a garment for scoliosis patients. At first, having enough knowledge about the human body, human skeleton, and morphology is necessary. As scoliosis is a type of spinal disability, understanding medical issues by considering how we can provide ergonomic and thermal comfort plays an important role. Then the main issue in this process is personalizing clothes according to different curves of their body.

Traditional methods to make 2D patterns for creating a garment for people with disability is almost impossible. Yan Hong, in previous work [1], proposed a new Personalized Garment Design Support System (PGDSS) for People with Atypical Morphology. This system quickly develops garments adapted to their special Functional, Expressive, and Aesthetic needs and atypical morphologies. The proposed Personalized Fashion Recommendation System has been developed by establishing a series of models for quantitatively assessing consumer's needs and characterizing relations between the spaces of consumer's needs and design parameters. Different knowledge acquisition and intelligent computational tools have been used to realize this system. These tools include sensory evaluation, fuzzy modeling, machine learning, etc [2]. A personalized garment product profile is generated by using this system. The proposed Virtual 3D-to-2D Garment Prototyping Platform has been developed to generate personalized garment patterns based on the product profile offered by the Personalized Fashion Recommendation System. New digital 3D technologies have been used to customize a garment for any atypical morphology. The 2D patterns and 3D garments will be provided according to the consumer's requirements [3].

However, even with this novel method, creating the pattern is still time-consuming, especially for that group of scoliosis patients under treatment, so their vertebrae are changing and after almost six months is not the same as before anymore.

After plenty of research to create a perfectly accurate pattern according to the body and customization of garments by the 3D scanner and other tools, this could be solved by integrating the full skeleton, anthropometric point, in general, is a position of the bone. Also, it is the connection between morphologic curves and anthropometric points during the modeling process. Thus, different anthropometric points from the position of bones will bring enough information

to create a garment. To adapt the 3D model for each case, we needed an automatic method to obtain data from a type of x-ray image.

Nowadays, the EOS system allows simultaneous anteroposterior (AP) and lateral 2D images of the whole body to be taken in a calibrated environment, permitting the 3D reconstruction of the spine and lower limb bony structures stereo radiography. The images are taken in the standing position, allowing the spine and lower limbs to be examined under normal weight-bearing conditions. Other publicized advantages of EOS imaging include true-to-size images since the machine scans the body with two 45-cm-wide X-ray beams, unlike the single-source divergent X-ray beam in conventional radiology, which induces magnification of the image (Figure 1.1). The main advantage of using the EOS system in this study is that we could automatically compare the manual data from EOS imaging with the obtained data automatically [4][5].

Figure 1.1: A patient standing in the EOS cabin in the required position for acquisition of orthogonal radiographs.

In order to obtain the data from the EOS image, an algorithm by deep learning is proposed. Image analysis is one of the most prominent fields in deep learning. Images are easy to generate and handle, and they are precisely the right type of data for machine learning: easy to understand

for human beings but difficult for computers. Not surprisingly, image analysis played a key role in the history of deep neural networks. There are lots of complicated algorithms for object detection. They often require huge datasets, very deep convolutional networks, and long training times. With a deep neural network, the computer can learn a generalized pattern of positions and predict corner location accordingly. By having the correct position of each vertebra and their corners, all the data can obtain.

Achieving enough knowledge about the skeleton and their anatomy by understanding the different division and functionalities of the vertebrae helped us have a clear view to model a 3D skeleton. This dramatically makes it possible to find a basic generic model on which it could graft the morphological specificities of each group in three morphological variants. Such a model is developed by considering the root of these specific curves instead of focusing on the human body. Thus, integrations of the full skeleton, anthropometric point, in general, is a position of the bone, and it is the connection between morphologic point, and the anthropometric point would give enough information to further apply in the customizations of garment design for scoliosis patients.

As the first step to model the spine, we need to analyze the different functionalities of the vertebrae, which strongly influence each of them. The goal is to understand why it is divided into three distinct groups (lumbar, dorsal, and cervical vertebrae), generating three types of morphology. However, given that some features could be common, would it be possible to find a basic generic model on which we could graft the morphological specificities of each group. Thus, we would have a generic model that could be derived in three morphological variants. After having a good 3D model of vertebrae, the model of human skeleton deformation that we wish to set up is focused on the trunk, which represents the human body without the head, nor the upper and lower limbs. The trunk consists of the spine, the thorax, and the scapular belt. The deformation of the spinal column is the essential element that transmits the deformation induced by the pathology's evolution to the rest of the skeleton (Figure 1.3Figure 1.2).
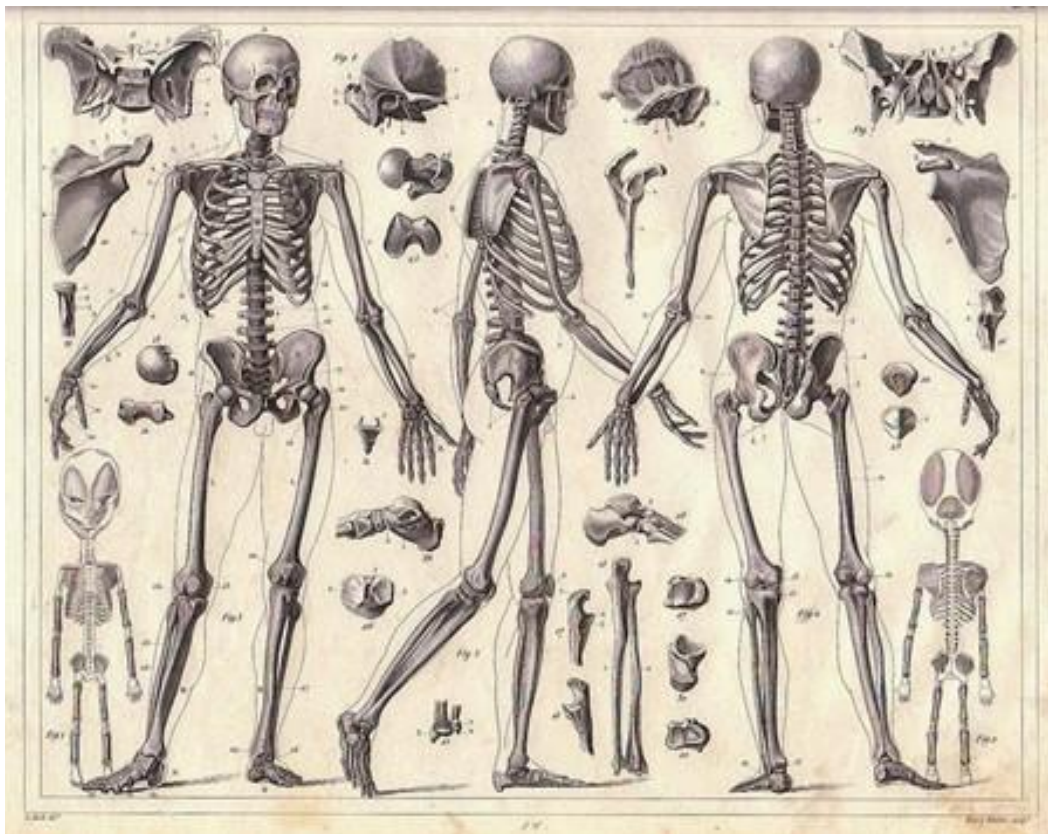
Figure 1.3: Full human skeleton with its components.
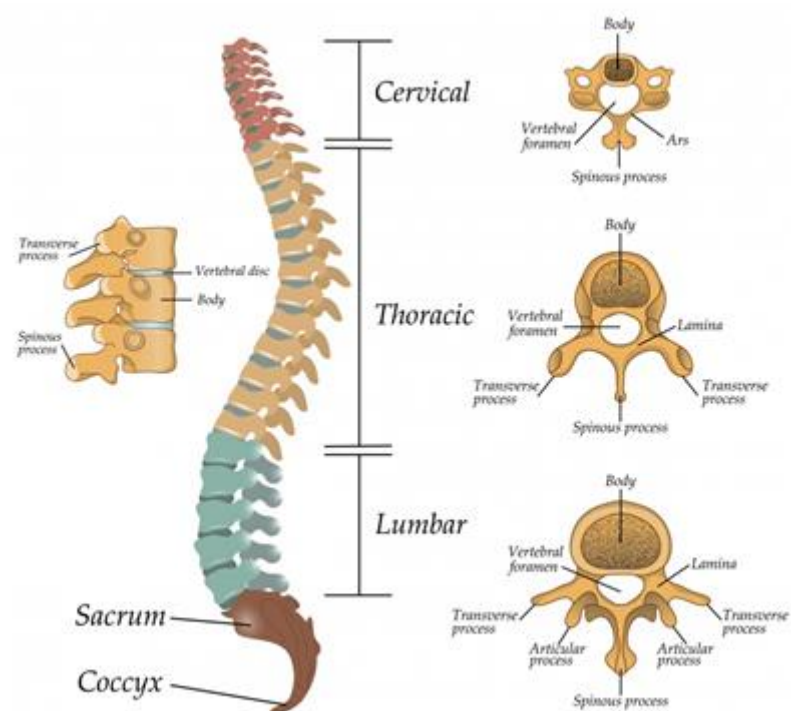
Figure 1.2: Structures and regions of the vertebral spinal column.

Thanks to previous work, we have a brilliant method to locate the morphological contours' position, which will allow positioning the garment relatively relative to the wearer's body. The anthropometric ratios that have been applied to this wearer are those that follow the rules of a woman's ideal proportion described by Loomis. Some primary contours follow the rules directly proportional to the stature (Figure 1.4: red and green contours). Other secondary contours are defined relative to the primary contours (Figure 4: yellow contours). The table of Figure Figure 1.4 shows that the stature manages the set of rules, making it possible to position the morphological contours along the vertical axis [6].

Stature	h	1655
H8	h/8	206
Chin	7*H8	1448
Shoulder	Chin-H8/3	1379
Under arm	6*H8	1241
Chest	Under arm-H8/6	1206
Under chest	Under arm-H8/3	1172
Waist/elbow	5*H8	1034
Navel	Waist-H8/6	999
Low waist	4.5*H8	930
Middle point	4*H8	827
Crotch	Middle point-H8/3	758
Low knee	2*H8	413
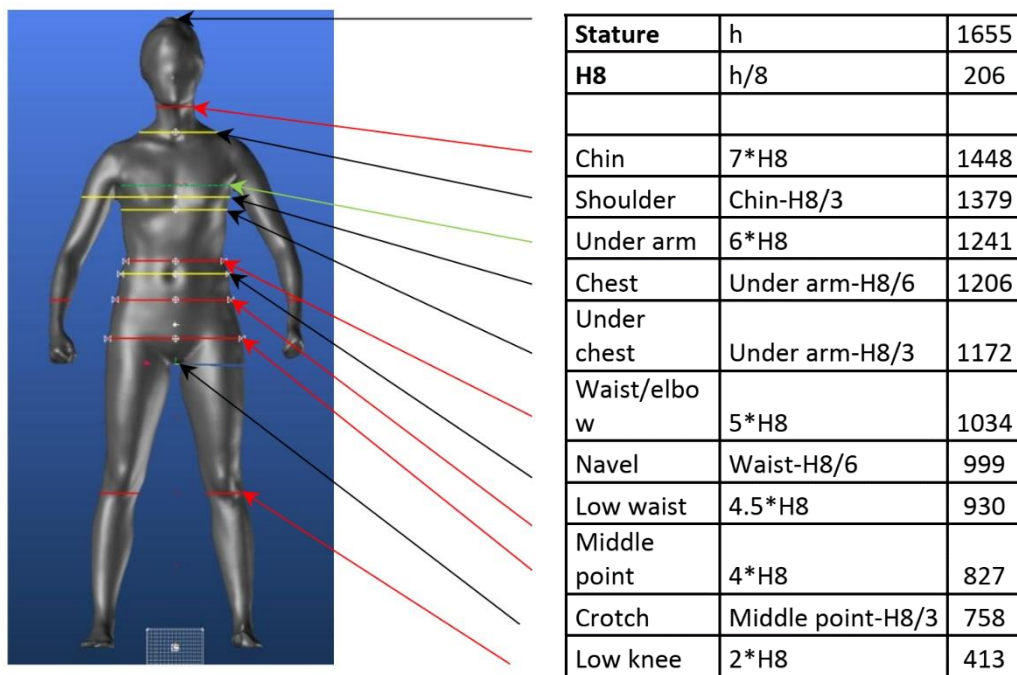
Figure 1.4: Anthropometric ratios of the human body.

The heat and mass transfer within the clothing system comprises several physical processes, such as dry heat exchange (conduction, convection, and radiation), evaporation and condensation, sorption, and vapor and liquid water transfer. In addition, factors associated with the construction and use of the garment, such as air penetration and compression by wind, body posture and movement, and clothing fit, influence these processes.

Significantly, this is achieved mainly by changing the fit and the shape of the layers of air trapped between the skin and clothing, between the clothing layers, and the air layer adjacent to the outer surface of clothing. Thus, the thermal, wicking, and evaporative properties of clothing depend not only on the properties of the fabric used for the garment but also on the magnitude of the contact area and air layers' thickness and change (Figure 1.5).
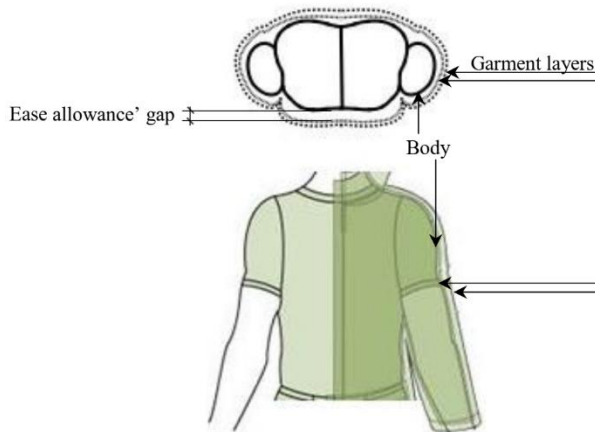
Figure 1.5: Graphic representation of ease allowance.
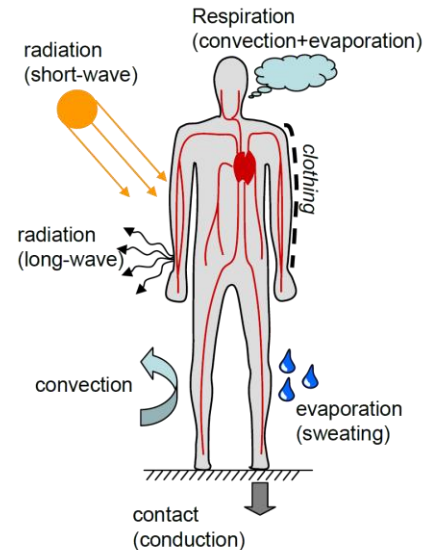
Figure 1.6: Boundary conditions acting on human body including its own regulatory mechanisms.

This air layer, which is ease allowance in garment designing science, is a phenomenon intricately linked to the garment style and fit. It is essential for the development of two- and three-dimensional pattern making (Figure 1.6). For the traditional 2D pattern making, the ease allowance is established as a linear value-added flat pattern. However, remembering that garment is design for a three-dimensional body, some information is missing while using just the body lengths and circumferences [7][8].

1.1 Morphological analysis of scoliosis

Scoliosis, as an atypical morphology, has an enormous influence on the garment design. The morphology of the human body will influence the shape of clothing provides a function (convenience and comfort) and decoration for the human body. For the people with atypical morphology, such as scoliosis, the clothing's function and decoration should be emphasized.

Since scoliosis issues are from vertebrae, the human body's morphological analysis is causally related to vertebrae's three-dimensional morphology (Figure 1.7).

Figure 1.7: Scoliosis deformation.

In recent decades, several studies are done to classify the morphology of scoliosis. The difference between normal vertebrae and scoliosis was unavoidable, such as; [9] distinct vertebral asymmetry: at the apical region of the thoracic curves; in the thoracic spine, the transverse endosteal width of the apical pedicles between 2.3 mm and 3.2 mm on the concave side and between 3.9 mm and 4.4 mm on the convex side, in the lumbar spine, the pedicle width between 4.6 mm at the cephalad part of the curve and 7.9 mm at the caudad part of the curve.

Current human body research (anthropometry) follows the average human body's morphological analysis, so working on scoliosis cases needs a new method to understand their morphology clearly [10][11].

Anthropometry is the interpretive and restrictively method to describe the human body shape. The tools and procedures of anthropometric measuring methods depend on the application. Whether dedicated to measurements for a single person or a broader population, they require adequate know-how. We can distinguish two main anthropometric measuring methods: manual called traditional (for human modeling) and automatically called digital (for digital human modeling). The first is also called the contact method, as it involves both person and the measuring instrument's physical participation. All methods from the second group are called non-contact, and they can be two- or three-dimensional [12][13].

1.1.1   Morphological analysis of normal skeleton and vertebrae

The human skeleton is the internal framework of the human body. This bone forms about 270 bones at birth - after some bones have fused, this enlargement decreases to about 206 bones in adulthood. Bone mass in the skeleton reaches its maximum density at about 21 years of age. The human skeleton can be divided into axial skeleton and appendix skeleton. The axial skeleton is formed by the spine, rib cage, skull, and other related bones. The appendix skeleton, attached to the axial skeleton, is formed by the shoulder girdle, the pelvic girdle, and the bones of the upper and lower limbs [14].

The human skeleton performs six major functions: support, movement, protection, blood cell production, mineral storage, and endocrine regulation.

The human skeleton is not as sexually shaped like many other species of sex mammals. However, there are subtle differences between the sexes in the skull, teeth, long bones, and pelvic morphology. In general, female skeletal elements are smaller and more resilient than the corresponding male elements in each population. The human pelvis is also different from that of men to facilitate childbirth. Unlike most mammals, human males do not have penile bones [15].

The human spine is involved of 24 vertebrae. They are structured in three anatomic groups: cervical (C1-C7), thoracic (T1-T12), and lumbar (L1-L5). Each group shares morphological and functional characteristics motivating their anatomic group classification [16][17]. The three groups are illustrated in Figure 1.7.

Automatic identification of spinal imaging such as: Computed Tomography (CT) and Magnetic Resonance Imaging (MRI), is crucial in the context of clinical diagnosis and surgical planning. While some vertebrae, such as the first cervical (C1), have a distinctive shape, other vertebrae, such as neighboring thoracic or lumbar vertebrae, share a visually similar morphological appearance [17].

1.1.2   Scoliosis Patients Issues

Caring for a patient with scoliosis with a history of more than two thousand years with the treatment of plaster and braces is a relatively recent endeavor. The modern period is almost more than half a century. Scoliosis is where the spine twists and bends sideways. It can affect people of all ages, from infants to adults, but often starts in children 10 to 15 years old. Scoliosis can be cured with treatment, but usually, the symptoms are nothing serious, and treatment is not always necessary. Most people with scoliosis can live naturally and can do most activities, including

exercise. This condition usually does not cause significant pain or other health problems. Having scoliosis or wearing a brace can be challenging and can create bad body image and bad self-esteem, especially for children and adolescents.

Apart from the medical perspective, the morphological figures of disabled people face a great problem in personalized products, including clothing, footwear, and furniture [18]. Clothing products that do not consider people with atypical morphology have significantly reduced the quality of life and social participation of this group. They are also forced to use different clothing design systems than ordinary people, which use standard sizing systems. This customized requirement clothing makes the cloth designing system overly complex, very challenging and leads to unaffordable prices. Be-sides, higher prices with bad quality and limited diversification create important barriers for adapted products [19]. Therefore, the traditional two-dimensional (2D) pat-tern design and garment development systems used for the normal body shape could not satisfy the requirements of disabled peoples such as scoliosis. Thus, developing and using a unique garment design system is vital to give the garment performance and good comfort and fit. Nowadays, 3D virtual mannequin model using three-dimensional computer-aided-design (CAD) technology becomes a commonly used method to obtain anthropometry information, declare ergonomics, and provide appropriate products for various consumers [20]. For example, 3D design software has been used to significantly improve the garment design process by overcoming the limitations of ordinary 2D design methods through developing a virtual 3D virtual mannequin model [21][22][23]. Some researchers are also dedicated to modeling non-adaptive 3D human bodies based on a generic reference model [24][25][26][27]. Basically, a parameterized model of the morphotype is based on a model surface representation defined by many sections of curves derived from the human body scanning. The concept of a set model of the morphotype occurs in these curves' choice and position and the relationship between them and the data from the measurement campaign [10][25][28]. Through these morphologic curves and anthropometric points, a basic pattern of the body will create globally. Some research has also used the correspondence between scanner data and the virtual model of the human body by converting the scanned body's mesh into a volumetric model [28]. Other was proposed an adaptive model adjusted according to the different human body [29].

However, all these improvements were not executable for scoliosis cases; even the recent adaptive methodology to parametrically designed garments on virtual mannequins, which can facilitate design, analysis, and hence to ensure the good consumer fit [30], is not any more adaptive for people with unusual curves in the body. Recently, a researcher was also dedicatedly

worked to develop a full garment designing system for the specific consumer's morphological shape with atypical physical deformations using non-adaptive 3D human modeling [31][32][33]. Such a modeling process is very time-consuming to generate garments when a patient's body changes through time and for patients with different morphologic problems. Besides, designing a garment for the different variations of patients with different morphological problems is a huge problem. This could be solved by integrating the full skeleton, anthropometric point, in general, is a position of the bone, and it is the connection between morphologic point and anthropometric point during the modeling process. Thus, different anthropometric points from the position of bones will bring enough information to create a garment.

Our current research focuses on the modeling of the vertebra to achieve enough knowledge about the skeleton and its anatomy through understanding the different divisions and functionalities of the vertebrae. This greatly makes it possible to find a basic generic model on which it could graft the morphological specificities of each group in three morphological variants. Such a model is developed by considering the root of these specific curves instead of focusing on the human body. Thus, integrations of the full skeleton, anthropometric point, in general, is a position of the bone, and it is the connection between morphologic point and anthropometric point would give enough information to further applications in the customizations of garment design for scoliosis patients.

1.2   Spine generic model (skeleton)

In the Anatomy 3D project at University Lyon 1, Olivier Rastello [34], the 3D designer of the medical team, has created a simplified 3D model of the spine. Authors proposed a 3D model corresponding to the general morphology of the spine and vertebra (Figure 1.8).
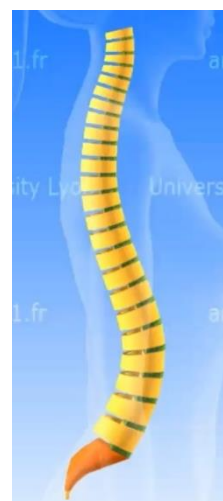
Figure 1.8: Vertebra and vertebrae column designed.

by university Lyon 1.

1.2.1   General morphology of the spine

Their study considered the vertebrae as the central pillar of the trunk, which must support the skull, constraints related to the thorax, and the movements of the shoulder girdle and arms, its lower part enters to the constitution of the pelvis. The tube of the pillar is full in its front half and hollow in the posterior part. The spinal cord is located in this tube, so the vertebra is a slice of the tube (24 movable vertebrae). A vertebra, therefore, presents a full front part and a hollow posterior part. The intervertebral disc (DIV) is located between both full parts. They represent about a third of the spinal column.

Intervertebral discs are deformable and elastic, so the spine is formed of a succession deformable and unreformable. The vertebrae column presents three curvatures that define the cervical region, thoracic region, and lumbar region. Cervical curvature corresponds to the cervical column, consisting of seven vertebrae (C1 to C7), lordosis. The thoracic curvature consists of twelve vertebrae (T1 to T12), kyphosis, and lumbar curvature in the lumbar column consisting of five vertebrae (L1 to L5) which is lordosis. The Vertebrae column comprises 24 mobile vertebrae and 13 intervertebral discs, and these 47 superimposed elements are a mobility factor. Movable vertebrae rest on the sacrum part, and the sacrum is formed of five fused vertebrae.

1.2.2   General morphology of vertebral type

The cervical, thoracic, and lumbar vertebrae are not alike. Their roles are different. They, therefore, have different characteristics. We describe a vertebra that unites all the characteristics common to the vertebrae (and which does not): the typical vertebra.

Consider a slid of the tube as the vertebra body, the upper faces, and lower bodies vertebral are called vertebral endplates. The empty part of the vertebra body makes the vertebral arch, the pedicles, the blades. At the top of the arch, there are joint processes superiors covered with cartilage and lower joint processes. In the side body, like two-hand as transversal processes, then there is the thorny process from the side of arch-like a tail. At the end, the body stacks of the bodies vertebrae and processes posterior joints from tree columns. The two posterior columns have a dynamic role: the articular processes guide and control the movements of the vertebrae during flexion-extension while the discs crash forward or back. The anterior column is mainly subjected to compressive forces. The discs "twist" during rotational movements. A reduction in

the DIV height will modify the ratios of the articular processes and, therefore, the statics vertebral. This explains many pathologies, including osteoarthritis.

1.2.3   The spinal canal, spinal cord, and spinal nerves

The vertebral foramen of a vertebra is limited: forward by the vertebral body back by the vertebral arch. The succession of vertebral foramina forms the vertebral canal (or spinal canal). Its upper orifice opens into the skull. Its lower opening is located at the bottom of the sacrum. The spinal cord is located in the spinal canal.

Spinal nerves originate from the spinal cord. They leave the vertebral canal at the level of the intervertebral foramen (or conjugation hole). A foramen vertebral is an orifice limited by:

- top to bottom: the pedicles,
- forward: the intervertebral disc,
- behind: a posterior column made up of the articular processes.

This 3D model is a single and general model to study anatomy, which is not necessary to customize by data of the human body. The advantage of our 3D model in this study is that an adaptive automatic model can customize by human body data.

1.3 3D modeling of spine by EOS imaging and vertebra detection

EOS imaging is a medical device which is made by a company based in Paris, France, that designs, develops, and markets EOSedge™ and the EOS system, innovative, orthopedic medical imaging systems, related with several orthopedic solutions and the patient care pathway diagnosis to post-operative treatments. The EOS platform targets musculoskeletal disorders and orthopedic surgical care through 2D X-ray scans and 3D skeletal models from stereo-radiographic images of patients in a seated or standing position [4][35].

EOS imaging's philosophy surrounds three main principles: reducing the radiation dose emitted by the technology, relevance and manipulability of calculated clinical parameters, and optimization of the patient care workflow. Over 300 EOS systems are currently installed in medical centers in 51 different countries, including the United States, Japan, Korea, China, and throughout the European Union [36].

The sterEOS workstation enables patient-specific 3D models of the spine and lower limbs from weight-bearing low-dose or MicroDose EOS exams. Once the models are created, clinical parameters are automatically calculated and exported as a patient report, including 2D images and 3D captures. Physicians use this report for diagnosis, post-operative assessment, and patient follow-up. sterEOS also enable the exportation of 3D anatomical biomarkers for pre-operative planning [37].

This technology based on a low-dose X-ray system allows 3D modeling of the spine based on two-dimensional X-rays acquired in an up-right position providing information about scoliosis and sagittal balance. It provides information about pelvic parameters. The X-ray system surrounds the chamber the patient stands within and scans the patient longitudinally in a weight-bearing position over a preset area. The sterEOS software is able to create the 3D modeling of the bone envelope based on anatomic references defined by the reader and providing specific clinical parameters (Figure 1.9).
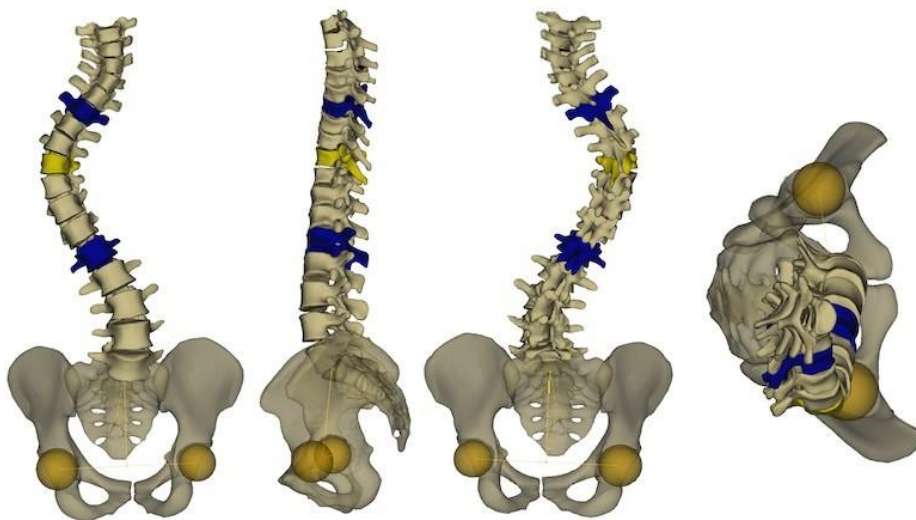
Figure 1.9: 3D model of vertebrae with sterEOS®.

Our research has illustrated a method for constructing an adaptive 3D model of the human vertebrae's complicated anatomical shape, which is accurate enough for several applications, including visualization and constructing statistical shape models. Besides, the models are also used to perfectly detect different anthropometric points and morphology curves on the breast to obtain unique points and scapula. Especial points on scapula play an essential role in creating clothing for scoliosis patients. The study explained previous models of the spine and the methods of obtaining data from radiologic images. The study also discusses how to construct a model of the spine by investigating and understanding the different functionalities of the vertebrae,

especially the lumbar, dorsal, and cervical parts. Later, using the different vertebrae functionalities, an innovative 3D design process was introduced to develop the 3D adaptive model. For each case, the developed adaptive model can ad-just by introducing various data values from the EOS image of the spine.

1.3.1   3D model of Spine

Three-dimensional models of the spine are widely used in spinal deformity applications. They can be used to detect and evaluate the severity of those deformities. They are essential because spinal deformities are three-dimensional and cannot be assessed using two-dimensional images alone. The three-dimensional nature of the models allows analysis that is impossible to do directly on radiography [38]. 3D spine models are usually simple sets of 3D anatomical signs. Depending on the clinical limitations and research objectives, six to fourteen characteristic signs are identified in each vertebra. A trained technician has done the previous work. The only advantage of using symbols is simplicity because the obtained models belong to a vector space in which all conventional statistics and analytical methods can be used.

For surgery to be successful, it is essential to prepare an excellent preoperative schedule and ensure adequate implant delivery. Computer-assisted orthopedic surgery (CAOS) [39] defines a set of techniques that use computers and other devices to plan, guide, and perform surgical interventions. Can be developed for different operating systems [40]. Important components of CAOS are accurate geometric models of damaged human bone and personalized 3D plate implant models that can be used in preoperative planning or surgical guidance during intervention. The first approach implies applying medical imaging technologies, like computed tomography (CT), to provide 3D geometrical models of human organs. Such models can be created in three general ways: using specialized software, which is part of the medical scanner, post-processing of medical images in medical-oriented CAD programs, post-processing in one of the CAD software packages. One of the main problems of this method is the inability to create a model of a complete bone. That is the case when the bone scan is incomplete due to illness (osteoporosis, arthritis, cancer, etc.) or trauma (multiple fractures, crushed bones, etc.) or when the quality of medical images is not good enough. The second approach for creating 3D geometrical models of bones or bone segments is based on the predictive geometrical or statistical model of bones and data obtained from medical images.

One of the possible applications of geometrical models of human bones is for internal fixation. Internal fixation is a surgical technique in which implants (plates, rods, pins, etc.) are

placed inside the human body. For bone fixation and reduction, plate implants are widely used. There are several types of these implants, but the most common are dynamic compression plates (DCP) and locking compression plates (LCP). DCP [41][42] developed healing processes by eliminating external immobilization and providing more stability to the fixation assembly. To perform their function, DCPs should be mounted onto the periosteum (the tissue that surrounds the bone surface) and should be pressed onto the bone to achieve stability [42][43][44][45].

Therefore, the blood supply to the bone can be interrupted, and cortical bone porosis can appear at the site of implant placement. A new plate design, the limited contact-dynamic compression plate (LC-DCP) [42], was introduced to reduce cortical necrosis. In today's practice, locking compression plates (LCP) is the most common [44]. These plates provide locking (locking screws) and nonlocking function, which means that they can combine properties of both the mentioned plates (DCP and LC-DCP). The recontouring of plate shape, i.e., the personalization of plate shape, is a typical operation that can be done before or during the surgical intervention. The need for recontouring is generally determined by a type of plate and bone disease. For example, reconstructive plates require recontouring to achieve mechanical stability. However, LCP with a locking screw is not necessary because the locking screws stabilize the stabilization system. Regardless of the need to redo the work, adjusting the shape of the screen is a good.

In all studies, the reconstructed models of the spines were used to compute 3D geometric curves and indices, considered as defining the shape of that patient's spine in 3D space [46]. To obtain these 3D geometric curves first important parameters are presented as:

- Planes,
- Angles,
- Classic Cobb angles of each curve in the bodily frontal and sagittal planes,
- Cobb angles in PMC [47],
- Rotations.

Between these classification parameters planes need more specific explanation:

The plane of maximal curvature (PMC) (Figure 1.10) is the plane described by the end and apex vertebrae; the curvature computes its orientation concerning the sagittal plane [48][47] in a symmetrical spine PMC lies in the sagittal plane. In the presence of scoliosis, its orientation represents a composition of the coronal plane deformity and of the sagittal plane physiologic kyphosis, which may not always correspond to the projections in the sagittal and coronal planes. The SRS committee introduced a schematic representation of the scoliotic spine called the "da

Vinci representation" (Figure 1.10) that illustrates the orientation of the planes of maximum curvature of the segments in the transverse view [49].
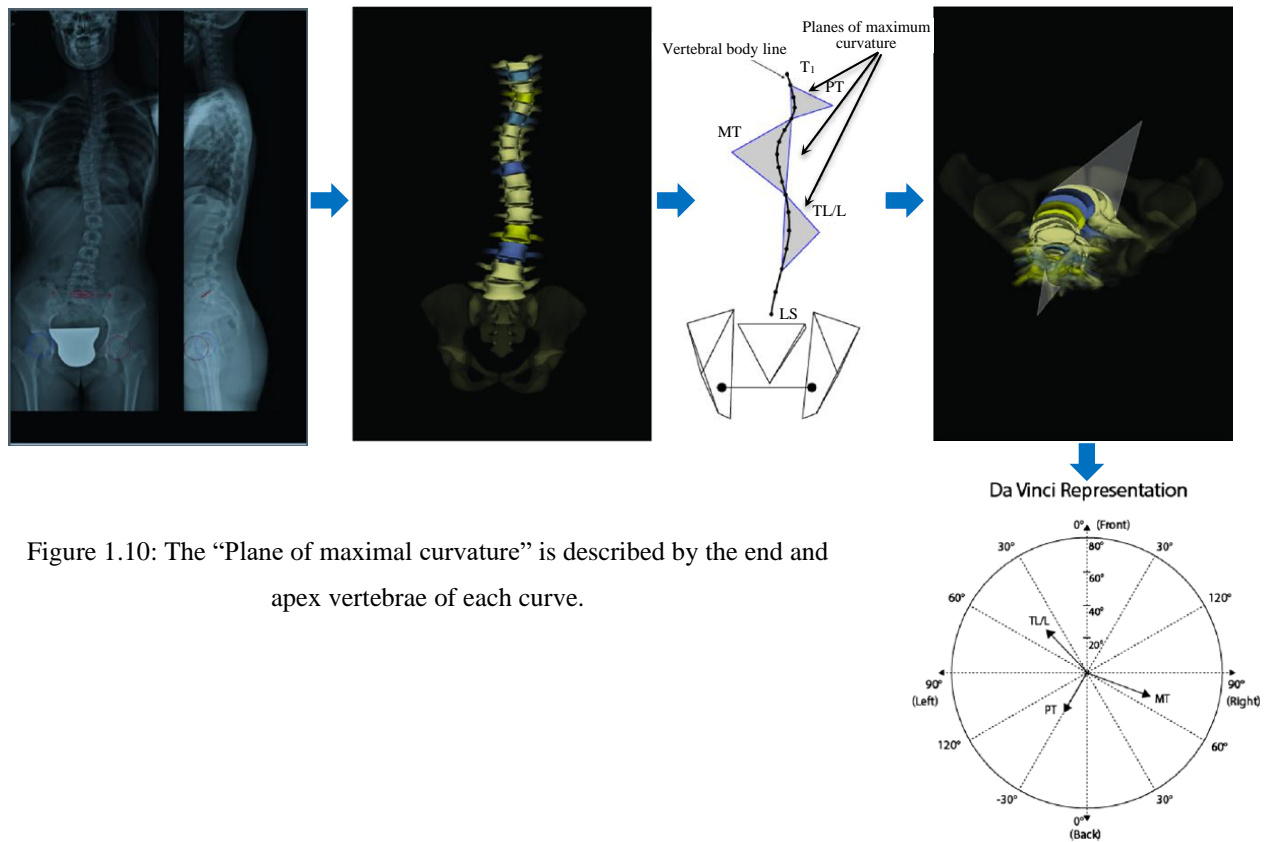
Figure 1.10: The "Plane of maximal curvature" is described by the end and apex vertebrae of each curve.

Best Fit Plane (BFP) [48] (Figure 1.11) is defined as the plane which minimizes the distances between the curve defined by the centroid of each vertebral body of a specified region of the spine.

Also there are two different rotations:

- Axial rotation of the apical vertebra, measured by the Stokes method rotation of the PMC [50][51],

- Geometric torsion [49]: an accurate 3D measurement defined as a local geometric property of the 3D curved line passing through thoracic and lumbar vertebrae that measures the vertebrae's helicoidal deviation without deformation of the vertebrae themselves.

In this thesis, having a model with high accuracy is not the primary goal. In our case, the model's main advantage is automatically adjusting by data from each customer. However, it is

20

accurate enough to use for obtaining the correct position of the anthropometric points. Moreover, the relationship between bones, cartilage, discs, and nerves is exact, even for medical study.
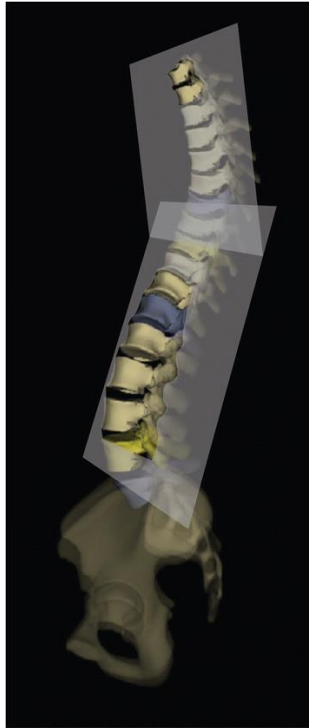
Figure 1.11: The "Best Fit Plane" (BFP) is the plane which minimizes the distances between the curve defined by the centroid of each vertebral body of a specified region of the spine.

1.3.2　Vertebrae Detection and Measuring

In this thesis, instead of using EOS software, an automatic method is proposed to obtain data rapidly. After studying image processing and detection methods, we understood that most of the process through filters and image treatments is a case study. We need to use different treatments for different images according to quality, contrast, and gender. These days most of the work about machine vision and detection is tanks to deep learning.

1.3.3　Scoliosis Pathologies

People with disabilities constitute a social group with atypical morphologies. Scoliosis is a sideways curvature of the spine that occurs most often during the growth spurt before puberty. While scoliosis can be caused by cerebral palsy and muscular dystrophy, the cause of most scoliosis is unknown. Most scoliosis cases are mild, but some children develop spine deformities that continue to get more severe as they grow. Severe scoliosis can be disabling. An especially severe spinal curve can reduce the amount of space within the chest, making it difficult for the

lungs to function properly. Children who have mild scoliosis are monitored closely, usually with X-rays, to see if the curve is getting worse. In many cases, no treatment is necessary. Some children will need to wear a brace to stop the curve from worsening.

Pisa syndrome is defined as a reversible lateral flexion of the trunk and tends to bend to one side. It is a recurrent and often debilitating complication of Parkinson's disease. It has also been described in several irregular forms of Parkinson's and neurodegenerative disorders after exposure to medication and surgery. Although no fixed diagnostic criteria are available for Pisa syndrome, cutting at least 10 degrees of lateral flexion to diagnose the syndrome is optional in most studies [52][53].

1.3.4   Manual Methods to Obtain Data for Scoliosis Patients

Physicians use the cobb angle as a gold standard for assessing and diagnosing scoliosis. Over the last several decades, the Cobb measurement performed on radiographs has been the most universally used method to characterize a spinal deformity. However, the Cobb measurement does not describe all of the important characteristics of a spinal deformity. This procedure is usually measured based on posterior-anterior radiography (X-ray) by selecting the most inclined vertebra at the top and bottom of the spine. The Cobb angle is the angle between the upper endplate and the lower endplate of the two vertebrae at the assessed curvature's extremes. It is used to distinguish between normal and pathologic conditions of the spine. Cobb angle can be reliably measured from a 3D reconstruction of the spine [54]. Orientation is relative to the imaging plane and the 3D/2D projection bias.13 Nevertheless, 3D imaging capabilities in weight-bearing positions are not yet widespread, and 2D Cobb angle remains an important and widely used radiologic measure in clinical practice. 2D Cobb angle is measured manually on a coronal x-ray by drawing intersecting perpendicular lines to the endplates mentioned above or, more commonly, by fixing landmark points parallel to these endplates in a picture archiving and communication system (PACS), automatically calculating the Cobb angle [55].

Some radiography practitioners should be attended as observers in this kind of study. Computer-aided Cobb angle measurements were performed on the Philips DICOM viewer [56]. Once the observers determine the superior and inferior end vertebrae location by placing two lines crossing the endplates, the Cobb angle will be automatically calculated using the software. Consensus and training on the measurement technique make among the observers beforehand to familiarize them with the software program and minimize measurement bias. Observers allow

adjusting the image contrast, brightness, and magnification to assist in the measurements. Each radiograph evaluates by each observer at an interval of 2 weeks. The end vertebrae determine and recorded by every observer for each radiograph at their first trial, so that the same end vertebrae use for their later-on trial.

The software SPSS [57] use for statistical analysis. Descriptive statistics, including the mean, standard deviation, and range of measurement report. Interobserver and interobserver reliability of measurements for each imaging method assess by the intraclass correlation coefficient (ICC) models 2 and 3, respectively. Reliability regard as inferior for less than 0.24, low for 0.25–0.49, moderate for 0.5–0.69, good for 0.70–0.89, and excellent for greater than 0.9 [57]. A statistically significant difference present between the two values of Comparison when their 95% confidence intervals do not overlap. A Bland–Altman plot also distinguishes whether the variation between radiographic techniques would significantly impact clinical performance. CR, DR, and EOS compare with each other using the Bland–Altman plot. For each Comparison, 95% limit of agreement use. Linear regression analysis performs for predicting the Cobb angle measurement by EOS using CR, or DR. Statistical significance was defined by p-value< 0.05 for all tests [58].

Most of the study to obtain data for scoliosis are based on cobb angle, which also we could use them to obtain all the data to create a 3D model of a skeleton. However, in this case, all these methods are too complicated and time-consuming. An automatic method to detect vertebra, their position, angles, and measure is necessary.

1.3.5   Calculation of data for Scoliosis Patients automatically

Recently artificial intelligence brought machine vision to calculate data from any kind of images and videos. This technology is able to help specialist in orthopedic field to detect cancer and any kind of health issue more accurate and quickly. Moreover, it is the best method to calculate skeleton parameters automatically instead of all manual methods.

1.3.5.1   Image Analysis by Deep Learning

Generally, it can be challenging for beginners to distinguish between different related computer vision tasks. For example, image classification is straightforward, but the differences between object localization and object detection can be confusing, especially when all three tasks

may be just as equally referred to as object recognition. Image classification involves assigning a class label to an image, whereas object localization involves drawing a bounding box around one or more objects in an image. Object detection is more challenging and combines these two tasks and draws a bounding box around each object of interest in the image and assigns them a class label. Together, all these problems are referred to as object recognition.

Deep learning technology has become a buzzword nowadays due to the state-of-the-art results obtained in image classification, object detection, natural language processing. The popularity of deep learning is two-fold, viz. large availability of datasets and powerful Graphics Processing Units. As deep learning requires large datasets and powerful resources to perform training, both requirements have already been satisfied in this current era.

Deep neural architectures handle complex models efficiently than shallow networks. CNNs (convolutional neural network) is less accurate for smaller data but show significant/record-breaking accuracy on the large image datasets. However, CNNs require a large number of labeled datasets to perform computer vision-related tasks (recognition, classification, and detection).

1.3.5.2   Object detection as a foremost step in visual recognition activity

Object detection is the procedure of determining the instance of the class to which the object belongs and estimating the object's location by outputting the bounding box around the object [59]. Detecting a single instance of class from image is called single-class object detection, whereas detecting the classes of all objects present in the image is known as multi-class object detection. Different challenges such as partial/full occlusion, varying illumination conditions, poses, scale, etc. are needed to be handled while performing the object detection. As shown in Figure 1.12, object detection is the foremost step in any visual recognition activity [60].

Verification	Detection & Localization	Classification	Naming	Description
Verify the presence of object in the image	Detect presence of object & provide its accurate location	Decide possible categories of object and classify objects	Determine the location & labels of the objects in the image	Describe actions & relationship of objects according to image context
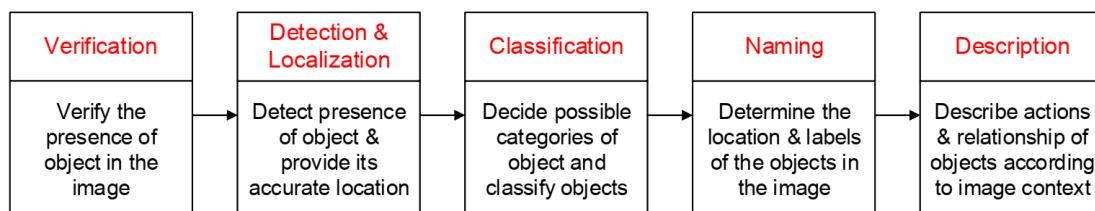
Figure 1.12: Object detection as foremost step in visual recognition activity.

1.3.5.3   Object detection using CNN

Deep CNNs have been extensively used for object detection. CNN is a type of feed-forward neural network and works on the principle of weight sharing. Convolution is an integration showing how one function overlaps with other functions and combines two functions being multiplied. Figure 1.13 shows the layered architecture of CNN for object detection [61].
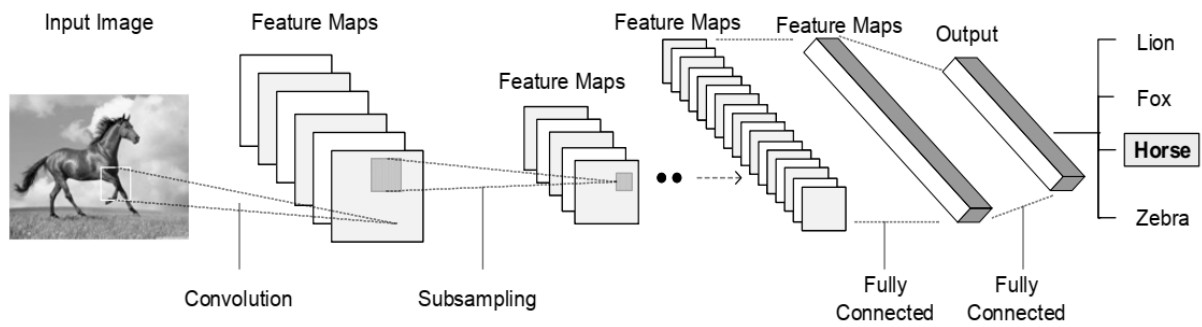
Figure 1.13: Use of Convolutional neural network for object detection.

Image is convolved with activation function to get feature maps. To reduce the spatial complexity of the network, feature maps are treated with pooling layers to get abstracted feature maps. This process is repeated for the desired number of filters, and accordingly, feature maps are created. Eventually, these feature maps are processed with fully connected layers to get image recognition output showing confidence scores for the predicted class labels. To ameliorate the network's complexity and reduce the number of parameters, CNN employs different kinds of pooling layers as shown in Table 1.1. Pooling layers are translation-invariant. Activation maps are fed as input to the pooling layers. They operate on each patch in the selected map.

1.3.5.1   Landmark Detection Focus on Vertebra

Existing regression-based methods for vertebra landmark detection [62] typically suffer from sizeable dense mapping parameters and inaccurate landmark localization. The segmentation-based methods tend to predict connected or corrupted vertebra masks. In this thesis, we have used a novel vertebra-focused landmark detection method. This model first localizes the vertebra centers, based on which it then traces the four corner landmarks of the vertebra through the learned corner offset. In this way, the method can keep the order of the landmarks.

Table 1.1: Pooling layers used for object detection.

Pooling layer	Description
Max pooling	It is widely used pooling in CNNs. It takes maximum value from the selected image patch and place in the matrix storing the maximum values from other image patches.
Average pooling	This pooling averages the neighborhood pixels
Deformation pooling [63]	Deformable pooling has ability to extract deformable properties, geometric constraints of the objects
Spatial pyramid pooling [64]	This pooling performs down-sampling of the image and produces feature vector with a fixed length. This feature vector can be used for object detection without making any deformations on the original image. This pooling is robust to object deformations.
Scale dependent pooling [65]	This pooling handle scale variation in object detection and helps to improve the accuracy of detection

1.4 Thorax model (skeleton)

The difficulties in quantifying the 3D form and spatial relationships of the skeleton components of the ribcage present a barrier to studies of the growth of the thoracic skeleton. Thus, most studies to date have relied on traditional measurements such as distances and indices from single or few ribs.

The thoracic cage is conical in shape narrow, above and broad below. Run your hands down the back of your ribs. Can you feel the shape of the cage? It is relatively flat; the anterior part of the cage is noticeably curved to accommodate organs within it. If you look at the cage in the transverse inferior, you will notice it is shaped somewhat like a kidney, which this kidney-like shape is ideal for protecting the heart and lungs. The 12 ribs that form the cage are uniquely shaped. Most have a head (articulates with the bodies of the vertebrae), a neck (flattened section of bone), and a shaft (serves as the attachment site for several muscles), The shape of the head is ideal for articulating with the vertebrae [34].

1.4.1   Anatomy and movements of the ribs

Each rib has its own special movement; rib cage transfers occur with the movement of the spine. During column extension, the rib cage migrates anteriorly, and the ribs are elevated. During spinal flexion, the rib cage moves posteriorly, and the ribs are depressed—lateral flexion results in a right or left shift of the rib cage in the frontal plane. Moreover, rotation of the vertebral column results in one side of the rib cage moving posteriorly and movement of the opposite side anteriorly in the transverse plane [66][67].

1.4.2   Thoracic Cage Anomalies

The thoracic cage is the skeleton of the thoracic wall. It is formed by the twelve thoracic vertebrae, twelve pairs of ribs and associated costal cartilages and the sternum. The three large parts of the rib cage can present certain abnormalities not assimilated to scoliosis:

- Cervical Rib
    - While most of us are born with 12 sets of ribs, it is not uncommon to have a normal variance or two. There is a chance, dear reader, that you may have more than the normal number of ribs. Crazy, right? Supernumerary ribs can be a harmless variant in most cases, but it can cause issues in some cases [68].
    - A cervical rib is a normal variant. A cervical rib is a congenital disorder in which one extra rib arises before the first normal set of ribs (01). It is small and is often called a "neck rib" due to its location. A cervical rib is present in only 0.5% of the population and is more common in females than in males. In rarer cases, an individual can present an extra set of cervical ribs.
    - A cervical rib is usually asymptomatic, but in some cases it can cause thoracic outlet syndrome by compressing the brachial plexus or subclavian vessels. Symptoms include pain almost always and discoloration of the hands, weakness of the hand or arm, and stiffness [69].
- Short Rib
    - A short rib is not a clinically significant variant and is named for when a mid-thoracic rib arch is shorter than it should be through no fault of trauma or surgery. A short rib occurs in approximately 16% of the population, and out of those instances, only 8% occur on the right side [70].

27

- Funnel Chest
    - o In contrast, pectus excavatum or funnel chest is a depression of the sternum, which causes the skin to be concave. In some cases, funnel chest is a cosmetic issue, but in others, it can lead to impaired breathing, heart displacement, decreased heart density, and chest pain.
    - o Now I want you to put your hands back on your chest and take a deep breath. Feel the 12 sets of bone expand against your fingers. If you ever get stuck on what it is your thoracic cage does, think of it as your body's police force: it shapes and protects [71].

1.4.3   Ribs and Scapula Geometric model

After the 3D model of vertebrae, the model of human skeleton deformation that we wish to set up is focused on the trunk, which represents the human body without the head, nor the upper and lower limbs. The trunk consists of the spine, the thorax, and the scapular belt. The deformation of the spinal column is the essential element that transmits the deformation induced by the evolution of the pathology to the rest of the skeleton.

Rib cage, in vertebrate anatomy, is a basketlike skeletal structure that forms the chest or thorax and is made up of the ribs and their corresponding attachments to the sternum (breastbone) and the vertebral column. The rib cage consists of the 12 thoracic vertebrae and the 24 ribs, and the sternum. With each succeeding rib, from the first or uppermost, the curvature of the rib cage becomes more open. The small joints between the ribs and the vertebrae permit a gliding motion of the ribs on the vertebrae during breathing and other activities [72].

Pocket Anatomy has been developed as a 3D Human Anatomy Model [73]. The skeletal system was built with aid from the visible human database from the Database Center for Life Science, University of Tokyo. The image data is loaded in 3dslicer, a free and open-source software package for image analysis and scientific visualization cropped to contain the area in which you wish to build a model. A labeled map is then created on the area of interest using the 'editor' tools in 3dSlicer.

Also, the result of 3D printing depends on the type of modeling method and process used to prepare a CAD model for 3D printing. Normally in CAD system, 3D scanning is one of the reverse engineering methods used to acquire 3D data by using a 3D scanner. The next stage of the modeling process is data processing. It consists of several parts. The non-contact scanner would capture the whole object with a series of scans from various angles and align the scans from

various angles. The previous model by CAD system CATIA V5-6R22 software was used [74][75] to develop the surface model of bone. A digitized shape editor was used at the initial stages of the reverse engineering cycle. In reverse engineering, the geometry of an existing physical object is captured by scanning. The result is obtained in the form of digitized data. Digitized shape editor allows various operations on this digitized data.

3D Model of the ribs and scapula in this thesis are entirely conceded to vertebrae data; they have been modeled step by step from ribs which are set upped a generic model identical for all vertebra after ribs sternum model plays an important role to create ribs case. The clavicle model has critical performance for connection between ribs case to the scapula. The scapula model is complex, and the correct shape of the scapula and the anatomy of the spine bring the acromion process with a complex 3D shape.

1.5   3D Garment model

The traditional pattern-making process is very time-consuming and requires professional fashion design knowledge. To develop a fitting garment to meet customer's individual needs, pattern makers must rely on a "trial and error" procedure until the customer is satisfied [76]. In the past four decades, the personalization of garments has been a successful business model for many fashion brands [77]. Concepts such as tailor-made design for the customer are gaining importance and leading to personalized consumer profiles. However, it should be noted that the larger problem of tailoring clothing to the customer's sizes and shapes has not been resolved. Modeling the 3D garment on the virtual body is one of the critical techniques needed to implement such a goal [78]. Previous works have proposed an approach of 3D modeling of the garment with relation to the virtual fitting. This method has set up a 3D wireframe model of the garment connected to the wearer by its morphological contours and its anthropometric points. The method is examined for gradation of the spatial distance between a body surface and a real and virtual test garment used to determine the value of the 3D fluency allowance relative to the correct adjustment (Figure 1.14) [79][77].

The new fitting garment design process is in a digital 3D environment. Nowadays, the design of a new garment is done directly on a mannequin or wooden mannequin with many precise and repetitive adjustments [25]. This step, commonly known as the draping technique, requires expert manual know-how [33]. Other design methods such as 2D model creation methods exist and are widely used as they are heavily practiced today in a digital environment. On the other hand, what

can be criticized is that they do not take into account the morphological and anthropometric data of the client because they are based solely on his measurements. By analyzing the needs of the clothing industry, it is imperative to reduce the time of the design stage following an increasing demand to change the collection imposed by fast fashion quickly [80]. In addition, the complete digitization of the garment design process is a possible solution, even cost-effective if implemented in a 3D environment [23][81].
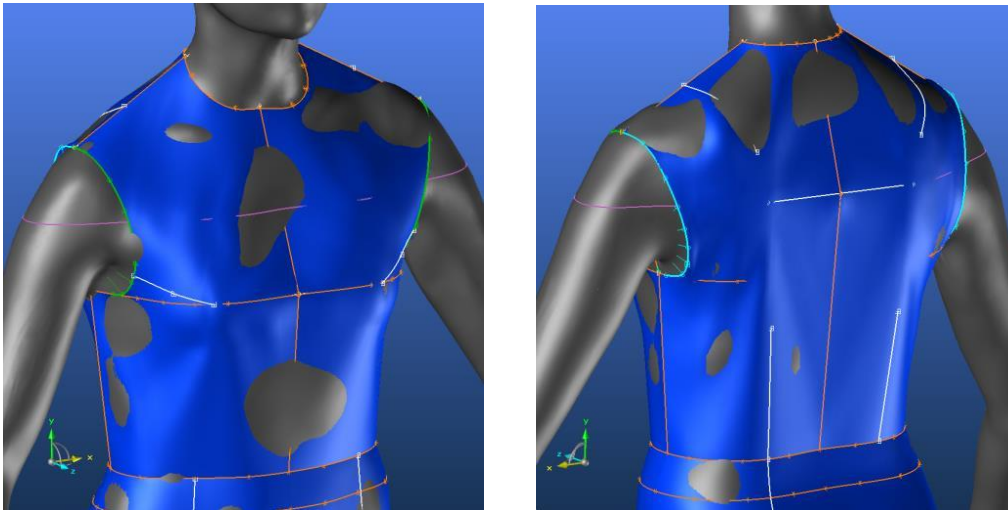
Figure 1.14: 3D garment surfaces.

1.6 The Human Comfort

Comfort is a subjective feeling, depending on the external ambient, by the clothing and physical activity. Comfort can be divided into two main types, psychological and physiological comfort. Psychological comfort refers to the need for each person to wear specific garments in terms of colors and design features to make them feel well. In contrast, physiological comfort is mainly affected by the thermal balance, namely the relationship between body heat production and losses [82].

Three main parameters influence human comfort:

- The external ambient,
- The human body,
- The clothing.

One of the main parameters that affect human comfort is the thermal behavior of clothing; this is a complex behavior that many researchers have studied [83][84][85][86]. Many factors can influence the thermal behavior of clothing, such as dry thermal insulation, air permeability, water vapor permeability, moisture adsorption, etc...
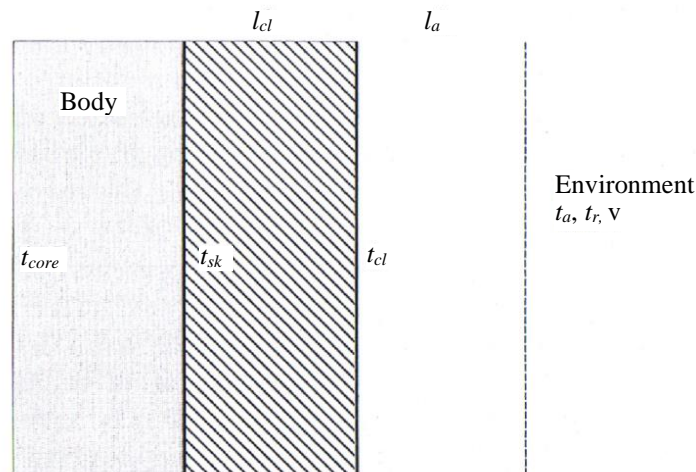
Figure 1.15: Thermal model with a layer of clothing insulation.

Dry thermal insulation is one of the most important parameters in the analysis of the clothing behavior; the most simple model is composed of a heated body with a layer of insulation clothing, as shown in Figure 1.15: Thermal model with a layer of clothing insulation [87], with :

t_{core} : mean core temperature

t_{sk}:   mean skin temperature

t_{cl}:   surface temperature of the clothed body

t_a: air temperature

t_r: mean radiant temperature

v: air velocity

I_{cl}:   intrinsic clothing insulation

I_a: thermal resistance of the environment

At the skin surface is placed the clothing layer that can be seen as a resistance to the heat flow from the body to the environment; this layer can be simplified using an intrinsic clothing insulation value (I_{cl}) that is the reciprocal of the clothing conductivity.

1.6.1   Heat and moisture transfer through ease allowance

Heat and moisture transfer in clothing occurring under wearing conditions depend on environmental conditions, human thermoregulatory reactions, thermal and evaporative resistance

of clothing layers, and distribution of the air layers adjacent to the clothing surface and entrapped in clothing ensembles. The bulk of thermal and evaporative resistances in clothing results from the thermal properties of textiles and the thickness of the enclosed air layers between clothing layers [88][89]. Besides, factors associated with the construction and use of a garment, such as air penetration and compression by wind, body posture and movement, and clothing fit, influence the distribution and thickness of air layers and affect the heat and mass transfer processes significantly. That is mainly due to the changing size and shape of the layers of air trapped between the skin and clothing, between clothing layers alone, and in the layer adjacent to clothing's outer surface. Thus, the thermal, evaporative, and wicking properties of clothing depend not only on the properties of the fabric used for the garment but also on the magnitude and the temporal change of the contact area and air layer thickness.

A garment is a 3D form created from the 2D pattern on the flat fabric to cover the human body's complex geometry. This fact, together with the fabric properties, entails draping and sagging of the garment. Effectively, the air layer's thickness is inhomogeneous, varies over body parts, and changes with body shape, posture, and movement. The example in Figure 1.16 illustrates the significance of the air gap thickness for thermal and evaporative resistances of an ensemble calculated according to Wissler's model. The air trapped beneath garments adjacent to the outer layer provides the bulk of both the thermal and evaporative resistances.

Moreover, it increases noticeably with only a slight change of 5 mm in the air gap thickness (Figure 1.16). Internal convection will take place if the air layer is larger than about 8-13 mm [90][91]. Therefore, determining the extent and location of air layers larger than 8-13 mm allows the analysis of possible air circulation. Moreover, analysis of the air gaps' distribution enables the assessment of thermal protection of protective garments from heat and flame since the thickness of the air layer influences energy transfer to the skin during flash fire conditions.
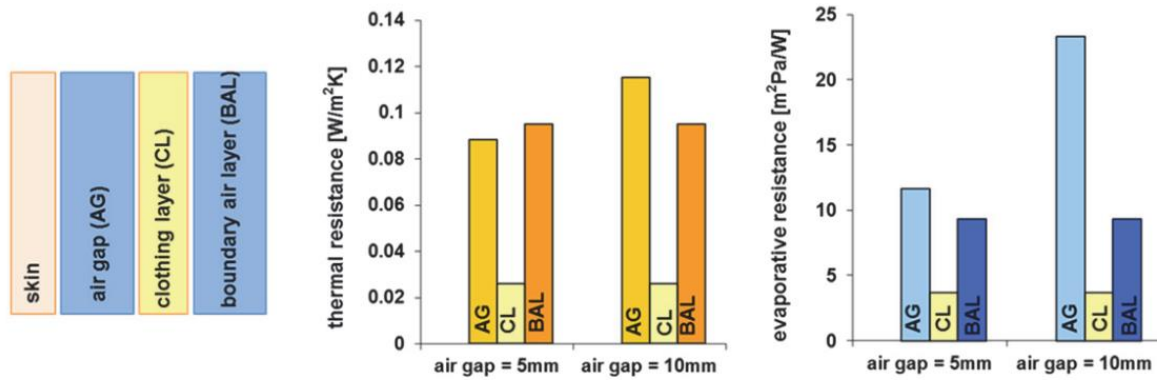
Figure 1.16: Thermal and evaporative resistances of the layers in a clothing system consisting of a cotton fabric (227g/m^2, 1mm thick) separated by an air gap as in scheme and obtained for environmental conditions as follows: Tskin= 34˚C, RHskin= 99%, Tambient= 10˚C.

In this study, instead of obtaining an optimized fit by experimental methods, a mathematical model is simulated to predict heat transfer along the air gap based on the multi-node model.

The mathematical model is set up to simulate the heat and moisture transfer from skin to microelement to fabric and fabric to the environment, including the radiation heat transfer. The multi-node thermoregulation model was developed based on the Stolwijk model [84]. The model has 16 body segments corresponding to the thermal manikin, consisting of four core, muscle, fat, skin, the inner layer of clothing, and the outer layer of clothing.

1.7 Conclusion

In this chapter, we have presented the state of the art of the different stages of an adaptive process for an optimal ergonomic fit and thermal comfort model of clothing for people with scoliosis. In addition, this model can be used for people without spinal problems, depending on their skeleton and their needs, considering that one objective is to obtain the desired thermal comfort.

The implementation of this process goes through the knowledge of the atypical morphology or not of the person, the creation of various digital models of the spine, the thorax, the garment, the latter integrating the concept of 3D ease allowance connected with a thermal model.

Reading this first chapter, the reader may be inclined to think that each step may seem distant from the others. However, all of these models and methods are closely interconnected: one model makes a critical contribution to the next model in a transversal and interdisciplinary spirit.

In order to bring a clear vision of this research, Figure 1.17 illustrates the adaptive process showing the connections between each model.
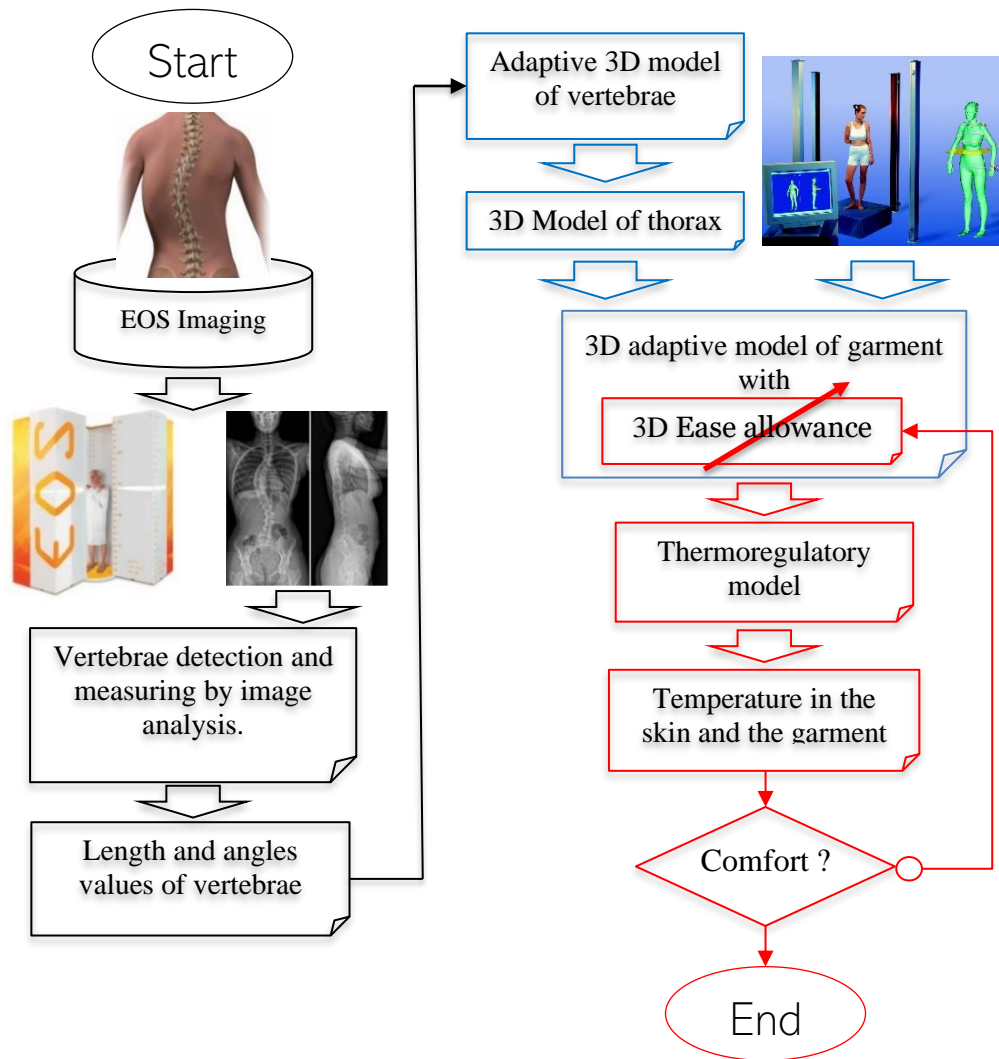
Figure 1.17: Global Process.

CHAPTER 2: 3D SPINE ADAPTIVE MODEL

The goal of this chapter is to develop a 3D vertebra model that has the ability to deform in 3 dimensions in order to follow the path of a person's spine, especially in the case of those suffering from scoliosis. Among other things, this model must adapt to the size of this person. To do this, we must understand the mobility of the vertebrae in relation to each other, as well as the limits and constraints of their movements in a 3D space.

Spine modeling therefore requires an in-depth analysis of the different functionalities of the vertebrae, which strongly influence the morphology of each of them [92][93]. The objective is to understand why the spine is divided into three distinct groups (lumbar, dorsal and cervical vertebrae), which generate three types of morphology. Since some characteristics seem to be common, the development of a basic generic model on which we could graft the morphological specificities of each group seems to be a priority in order to reduce the complexity of the modeling, in particular during the parameterization acting on the volume and the relative position of each vertebra. This generic model will be declined in three morphological variants knowing that the variant of the cervical vertebrae will require to take into account the morphological specificities of each of them.

2.1 A generic model of different vertebrae morphology

As we previously reported, spine modeling requires a thorough analysis of the different functionalities of the vertebrae. The spine not only provides vertical stability in the trunk and neck, but it also has a protective role of sensitive organs such as the spinal cord, ventral and dorsal nerve roots, nerve roots of the spine, vertebral arteries. The spine's modeling must consider all morphological constraints imposed by different functional, mobility, and stability criteria.

Each vertebra has an anterior and posterior arch. The posterior arch forms a hole called the foramen. The spinal cord passes through the foramen of each vertebra. The vertebral bodies de-fined by the anterior arches are connected among themselves by the intervertebral discs. The posterior arch is composed of the pedicles, laminae, and processes. The pedicles can be represented by two short cylinders of bone that extend from the vertebral body. Laminae are two plates of bones that form the walls of the posterior arch. The transverse processes extend out on

either side of the laminae. The spinous process is very variable in function of the vertebra type. We can be felt it through the skin in the body's back.

The spinous process will allow defining the exact position of the spine when inserted into the body. Figure 2.1 schematizes the relationship between the spinal cord and the nerve roots coming out on either side of the spine. This connection towards the whole nervous system acts on the morphology of the vertebrae by excavations.
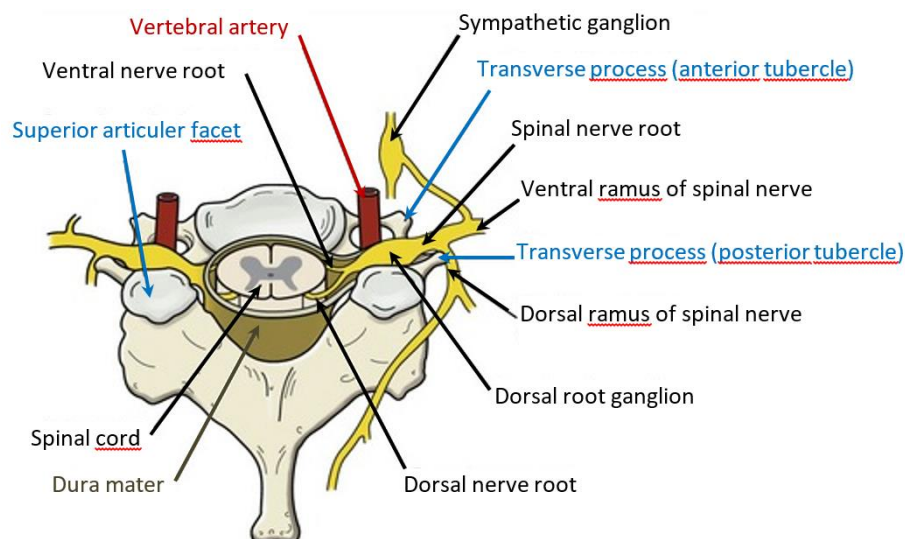
Figure 2.1: Relationship among the neural tissues, components of vertebra and the vertebral artery.

Similarly, each vertebra's stacking and adjustment (Figure 2.2(a)) on top of each other contributes strongly to their morphology by prominences leading to the upper and lower facets representing the joint process's contact zones. Other contact zones are located at the intervertebral disc level, whose role is to ensure the spinal column's damping against heavy loads and bring the mobility or 3D deformation of the spine.

The spine's modeling has to consider all these morphological constraints imposed by these different functional, mobility, and stability criteria. Other physical constraints are more specific to the group to which the vertebra belongs. For example, the lumbar rachis has a protective role in the spinal cord but also of support. It guarantees the posture of the trunk and the standing support. For this, the lumbar vertebrae structure is robust to allow the trunk to twist, bend or stretch.

On the other hand, the dorsal rachis is not very mobile and carries the thoracic cage. For this purpose, is provided with a specific transverse process and costovertebral joint to allow each

rib's hanging and positioning. The cervical rachis is concerned. It has excellent mobility like the lumbar rachis without having this important supporting role. Its particularity is that each cervical vertebra presents notable differences that will lead to different vertebrae models for this rachis. Although the vertebrae have slightly different appearances, they all have the same basic structures with the same names, as shown in the previous analysis. The lumbar vertebrae have the particularity of grouping all the common points of each vertebra because they represent the spine's starting point. Thereby, the vertebra's generic model can be set up from the morphology of the lumbar vertebrae described below (Figure 2.2(b)).
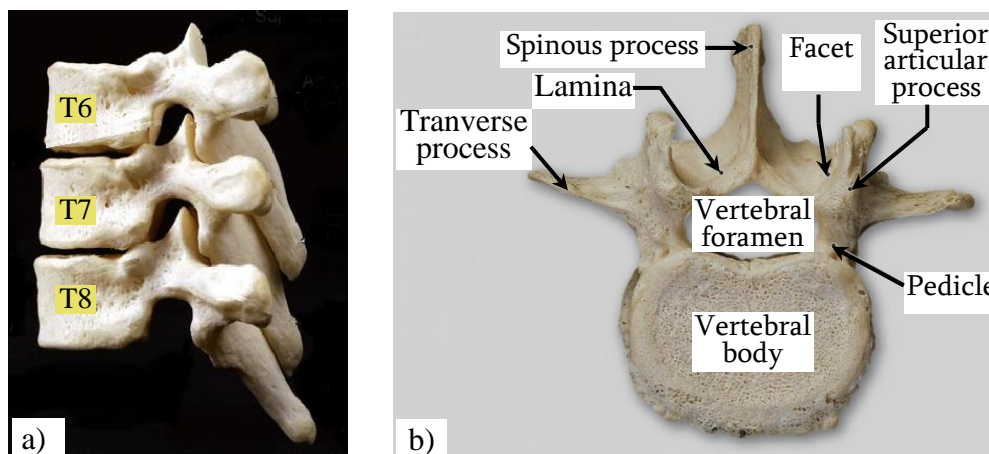
Figure 2.2: Lumbar vertebra assembled and in upper view.

Each vertebra has an anterior and posterior arch. The posterior arch forms a hole called the foramen. The spinal cord passes through the foramen of each vertebra. The vertebral bodies de-fined by the anterior arches are connected among themselves by the intervertebral discs. The posterior arch is composed of the pedicles, laminae, and processes. The pedicles can be represented by two short cylinders of bone that extend from the vertebral body. Laminae are two plates of bones that form the walls of the posterior arch. The transverse processes extend out on either side of the laminae. The spinous process is very variable in the function of the vertebra type. We can be felt it through the skin in the body's back. The spinous process will allow defining the exact position of the spine when inserted into the body.

2.2 3D Adaptive Vertebrae Model

2.2.1 Generic model

Lumbar vertebrae model
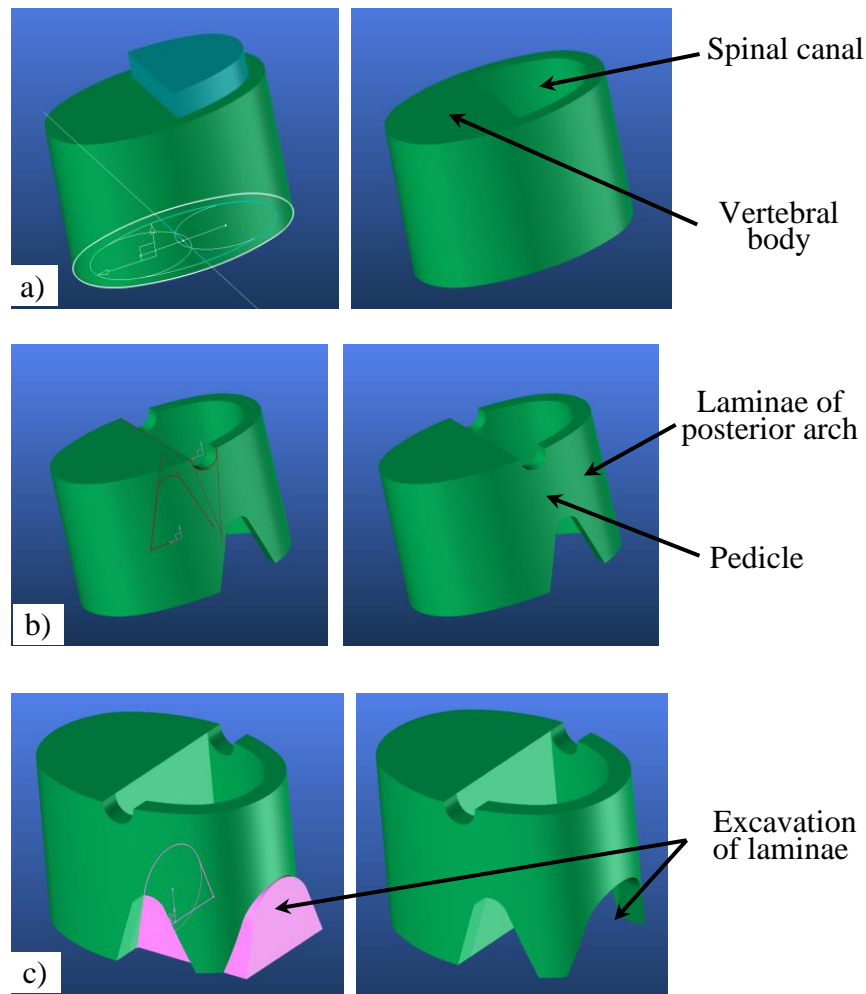
Figure 2.3: The modeling process of a lumbar vertebra: (a) vertebral body and spinal canal creation, (b) pedicles creation and (c) improvement of the laminae of posterior arch.

The modeling process of a lumbar vertebra begins with creating its vertebral body Figure 2.3(a). A first extruded circle at the vertebra's height creates the two upper and lower vertebral plates and the volume of the vertebral body. Another eccentric circle at first is partially used to define the spinal canal (blue shape). The diameters of these two circles are proportional to their extrusion height to adjust their dimension to the lumbar vertebrae number. Thus, the vertebra volume is managed by its height, which is defined proportionally to the total length of the spine according to an anthropometric report that we will specify later.

The next step is to dig the lateral part of the 3D model into designing the pedicles (Figure 2.3(b)). Two half-circles extended on each side by two inclined lines (red) make it possible to define and dimension the pedicles' upper and lower openings. The diameters of the circles and the inclination of the lines associated with these circles allow the pedicles to be adjusted according to
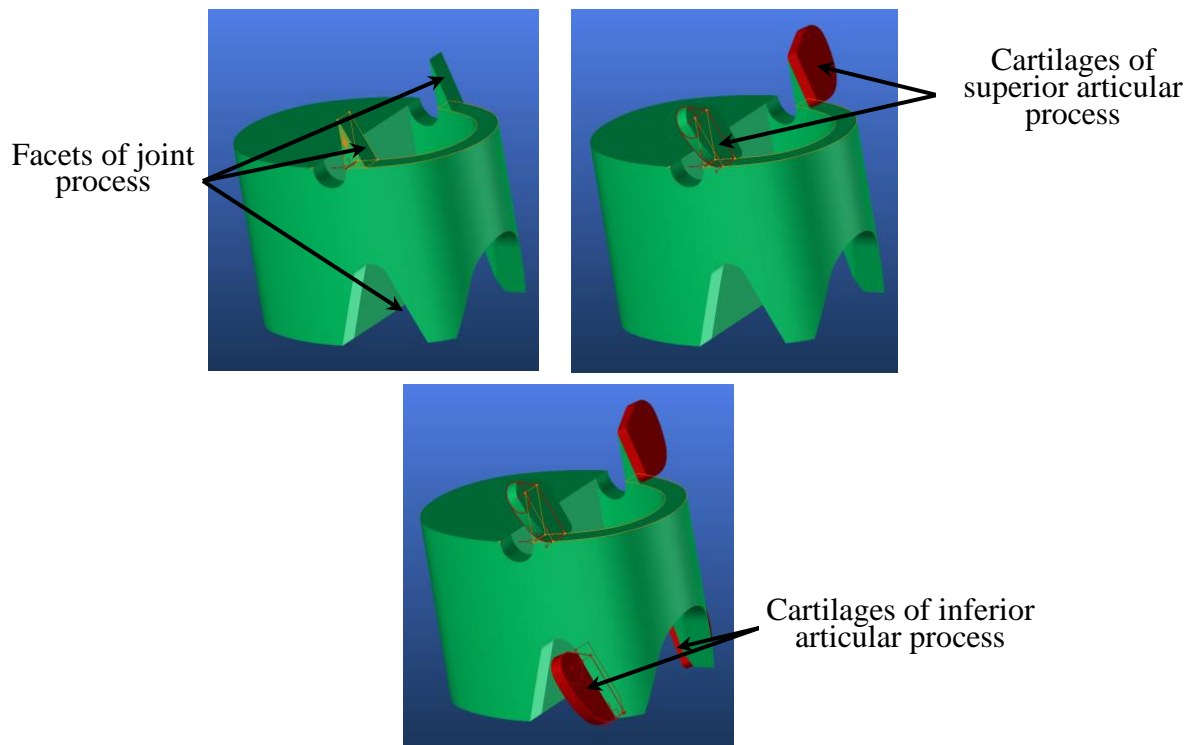
Figure 2.4: Superior and inferior articular process creation.

the height of the vertebra. The figure clearly shows the vertebral arch composed of the two pedicles and the two frontal laminae.

A recess has been made in the laminae of the posterior arch to get as close as possible to their final shape (Figure 2.3(c)).

Then we defined the superior articular process. It was positioned at the frontal end of the upper part of the pedicle. This inserted element allows us to manage the height, width, and inclination of the superior articular process. The inclined facets are then covered with two cartilages, which are morphologically managed by four circles located at the four corners of the basic surface, which generates the cartilage volume (red) (Figure 2.4). Concerning the inferior articular process, the inclined facets of the lower part of the pedicle.

The process of modelling the lumbar vertebra begins with the creation of its vertebral body then the vertebrae volume is controlled by its height, which is proportional to the total length of the spine according to an anthropometric report that we will find out later. The next step is to the lateral part of the 3D model into designing the pedicles. Then we defined the superior articular process. It was positioned at the frontal end of the upper part of the pedicle. This inserted element allows the method to manage the height, width, and inclination of the superior articular process.

An essential element in the vertebrae overall dimensioning is the spinous process with a curved and long shape.

About the inferior articular process, the inclined facets of the lower part of the pedicle are also covered with two cartilages that are managed in the same way as the upper cartilages since the stacking of the different vertebrae imposes a perfect alignment of the upper and lower part of the pedicle and the upper articular process.

The transverse process is positioned laterally and perpendicularly to the vertebra's upper surface (Figure 2.5). Thus, we can manage the transverse process by its frontal and dorsal inclination, its volume by the two basic circles that generated this volume, and its extrusion length. An important element in the vertebrae overall dimensioning is the spinous process with a more or less curved and long shape (Figure 2.5). To do this, we have created a guide curve that manages both the length and curvature of the spinous process. A base surface created by two eccentric circles runs perpendicularly along this curve, gradually reducing when it reaches the spinal process's tip.
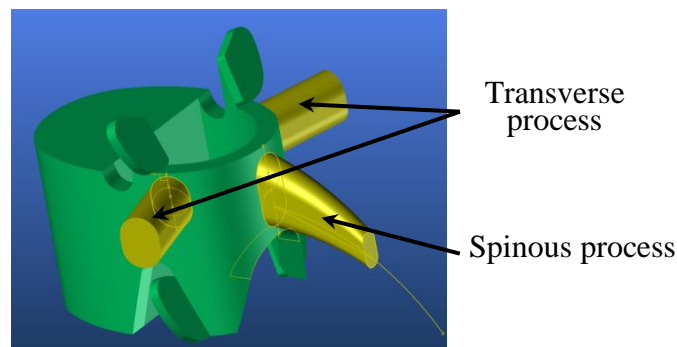
Figure 2.5: Transverse and spinal process creation.

Finally, Figure 2.6(a) shows our final generic model representing three-dimensionally controllable lumbar vertebrae by the different green dimensions (Figure 2.6(b)). These dimensions are concerning to have only one parameter allowing this model to evolve from the lumbar vertebra L5 to the lumbar vertebra L1 (Figure 2.6(c)).
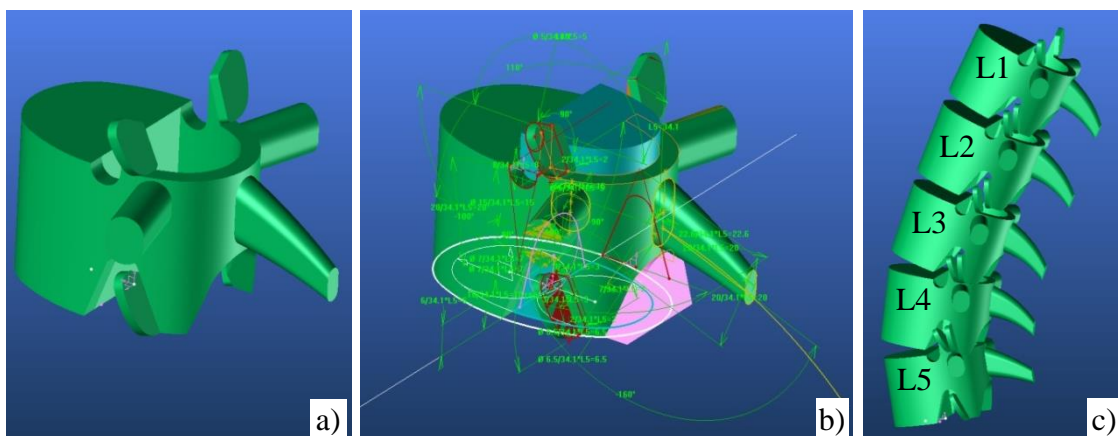
Figure 2.6: (a) and (b) Adaptive vertebra modelling process and (c) lumbar vertebrae L1 to L5.

Dorsal vertebrae model

The dorsal vertebra model is like the lumbar vertebra model. Apart from the size of the vertebrae, which gradually reduce from the D12 to the D1, they different morphologically from the lumbar vertebrae in their spinous process, straighter for the D12, more curved and shorter for the D11, more marked and imposing in length for the following ones (D10 to D1) (Figure 2.7(a)). To do this, we act on the curvature of the guideline that gives this curved shape. Another difference is in the transverse process, which is shorter and slightly closer to the spinous process (Figure 2.7(b)).
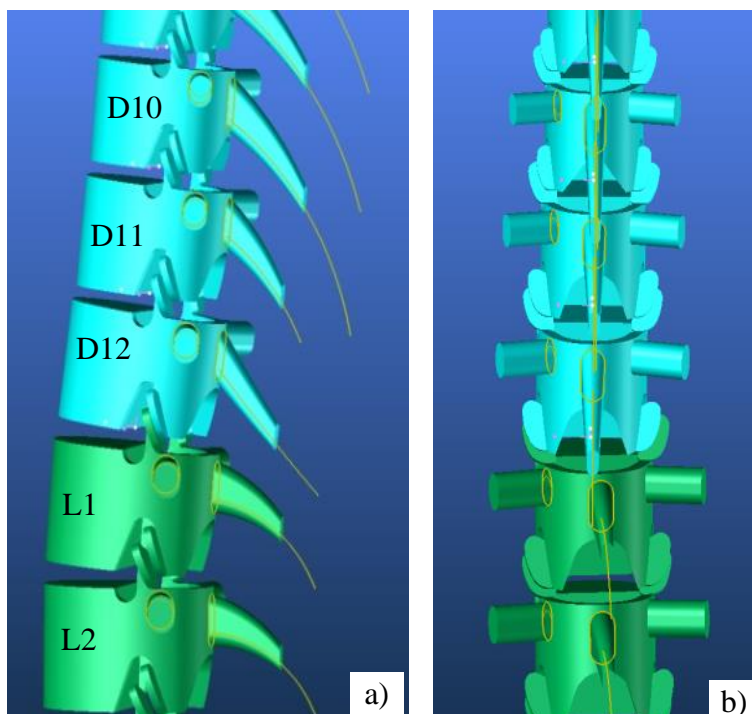
Figure 2.7: Dorsal vertebrae model (a) side and (b) back view.

Cervical vertebrae model

The modeling of cervical vertebrae is very complex because each of them presents morphological differences. For example, the stacking of the vertebrae one on the other shows a very marked overlapping in the area of the intervertebral discs (Figure 2.8). The search for similarities, which will later allow us to set up a generic model that can be modified according to the vertebra, shows that each vertebra has a transverse foramen located within the transverse processes. Figure 2.1 shows that the vertebral artery rises through this foramen to supply blood to the brain. The length and shape of the spinous process are also very specific from one vertebra to another.
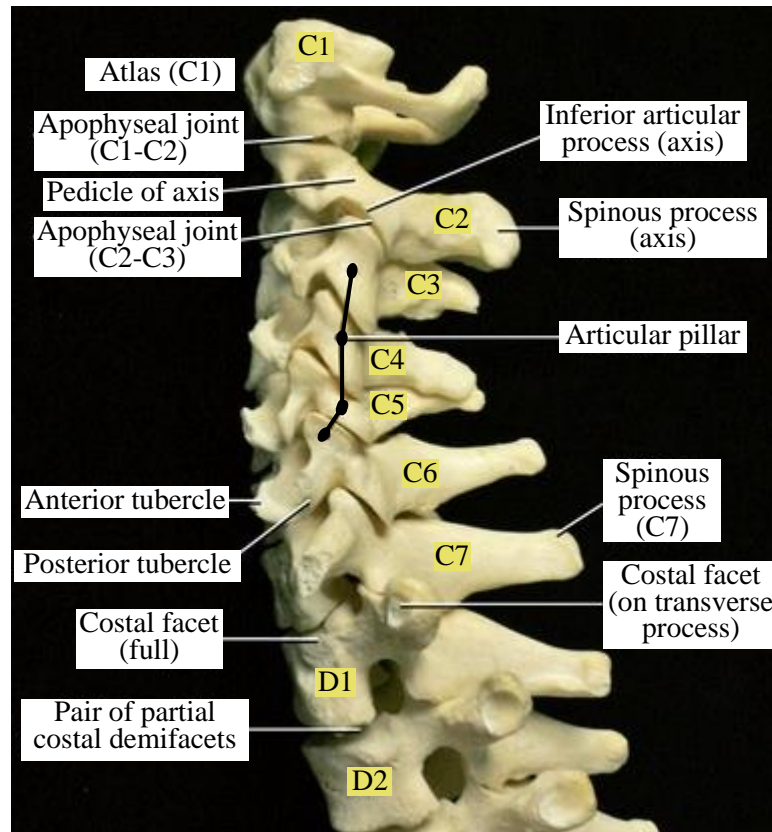
Figure 2.8 Lateral view of the cervical vertebral column.

These similarities and distinctions lead us to consider four types of models. The first is dedicated to the C7, the second is common between the C6, C5, C4, C3, the third model is specific to the C2, and the last model is exclusively dedicated to the C1.

> ➤ C7 Cervical vertebrae model

C7 is atypical because it is at the interface between the dorsal and cervical vertebrae, which imposes two types of contact morphology with the upper and lower intervertebral discs (Figure 2.9(a)). Starting from the C1 dorsal vertebra model, we added a purple block and inclined the

upper part of the new transverse process to obtain a suitable connection with the C6 vertebra (Figure 2.9(b)). The transverse process was modified in his posterior part to get a better seating of the vertebrae on each other and completed by anterior and posterior tubercles to define the transverse foramen. The spinous process has been adapted given its very prominent presence.
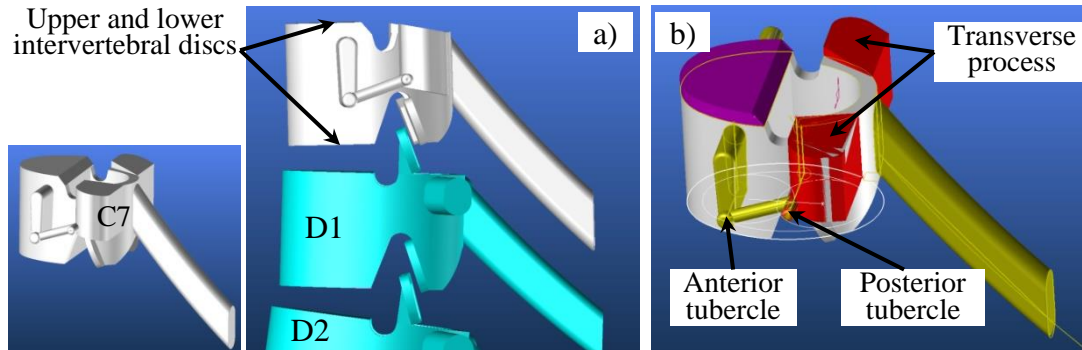
Figure 2.9: C7 cervical vertebra model.

> ➢ C6, C5, C4, C3 Cervical vertebrae model

As we mentioned earlier, the C6, C5, C4, C3 cervical vertebrae are very similar (Figure 2.10(a)). Their vertebral body is generally smaller while their spinal canal is larger, managed by the two lower white circles (Figure 2.10(b)). The pedicles have been adjusted thanks to the basic red circles and inclined red lines and repositioned due to the decrease of the vertebral body. The superior and inferior surfaces of the vertebral bodies are not as flat as those of most other vertebrae but have been curved with the purple and yellow blocks. The transverse process has been adjusted to create a new articular process that defines a continuous articular pillar (Figure 2.10(a)). The spinous process of C6 has been reduced if we compare it with the C7, more reduce and cursed for the C5, C4, C3.
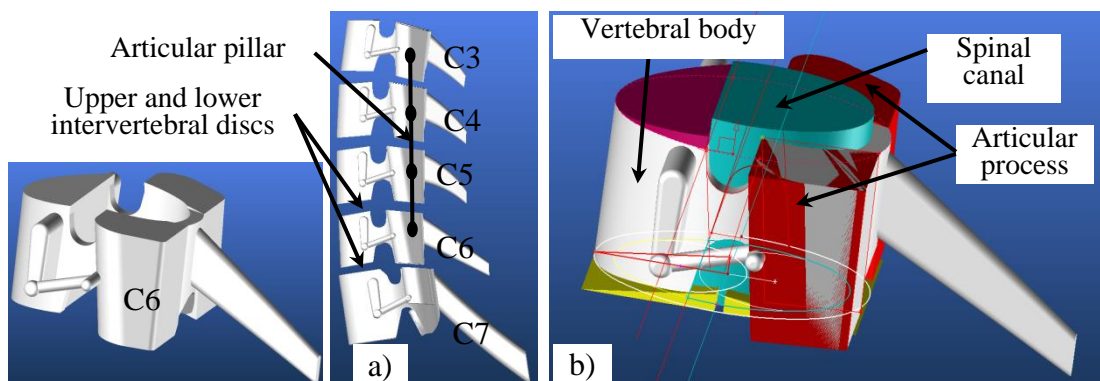
Figure 2.10 : C6, C5, C4, C3 cervical vertebra model.

➢ C2 Cervical vertebrae model

The vertebral body of the C2 is quite imposing due to higher inclination on his superior part, which is in opposition with the one of his inferior part. It has to support axially the dens serving as the axis of rotation for the C1, modeled by a red cone (Figure 2.11). Two articular processes have been designed laterally on the vertebral body. The first in yellow corresponds to the upper articular process connected with the C1 and modeled by two curved blocks located on either side of the body. The second in red is like C3, C4, C5, C6. Changes were made to the posterior tubercle that we reduced to the anterior tubercle that we moved upwards to obtain an inclination in opposition to the C3. Transversal processes have been shortened. The spinous process expands more and more towards its end. However, the bifid characteristic has not been considered. (Figure 2.11)
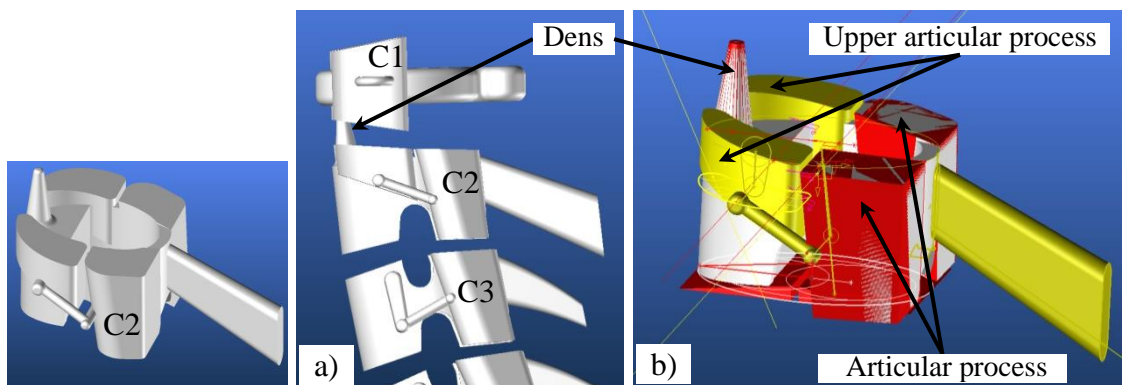
Figure 2.11: C2 cervical vertebra model.

➢ C1 Cervical vertebrae model

It can be represented by a ring on which we laterally grafted two blocks. These blocks represent the joint process that must support the skull in its upper part. A judicious positioning and dimensioning of these blocks make it possible to describe two anterior and posterior arcs. The posterior arch is larger than the anterior arch and has a small tuber at its tip. Two transverse processes must be grafted onto the two blocks to hook the different muscles controlling the fine movements of the cranium (Figure 2.12).
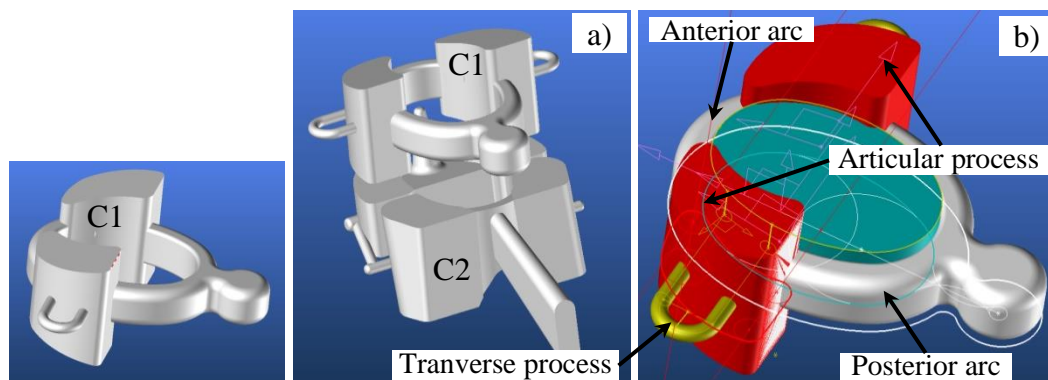
Figure 2.12: C1 cervical vertebra model.

2.3   Results and discussion

2.3.1   Virtual and real model of cervical vertebrae

Models we have created do not pretend to represent the morphology of vertebrae perfectly, but they aim to be dimensionally and functionally close to them. The dimensional aspect will only be carried out later on certain specific blocks of the models. For example, the height, width and height of the vertebral body, the length of the overflow towards the outside of the transverse processes, of the spinous process will be parameters that we will obtain during the image processing, in the frontal and coronal plane, of the radiographs of the patient's spine. Thus, they are dynamic models that have the faculty to approach the shape of the vertebrae thanks to a specific parameter setting of each of them and that for any type of person of typical or atypical morphology.

Figure 2.13(a)(b) shows that the generic model we have created from the shape and specificities of the lumbar vertebrae is close to reality. We could criticize that the position of the articular processes of our model is farthest back toon the posterior part. But this is not a problem because the joint process can slide and follow the upper curve of the laminae of posterior arch. This model which we slightly modified to adapt it to the dorsal vertebrae follows relatively well the shape these last. We can notice on the Figure 2.13(c)(d) that the stacking of D6, D7 D8 is well respected. A critique could be made on the shape of the spinous process which tends strongly downwards in the real case. But still, our model manages this aspect by modifying the shape and the inclination of the director (yellow curve of Figure 2.5) which defines this 3D shape.

45
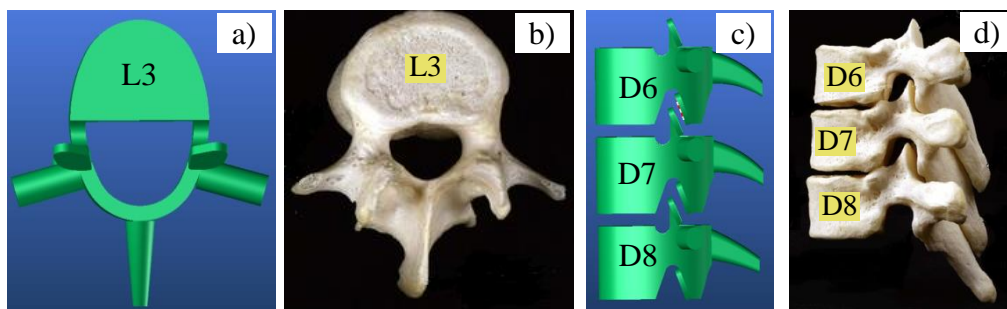
Figure 2.13: Virtual and real model of lumbar and dorsal vertebrae.

As already mentioned, the cervical vertebrae have a very specific articular process which leads to a strong overlapping in each other. The real world of the stacking of the 7 cervical vertebrae in Figure 2.8 shows that we are fairly close to reality (Figure 2.14(a)). Each specific model integrates well all the morphological specificities of their category. C7 has a very important spinous process, as well as a transverse process very different from that of the generic lumbar and dorsal vertebrae model Figure 2.14(b)(c)).
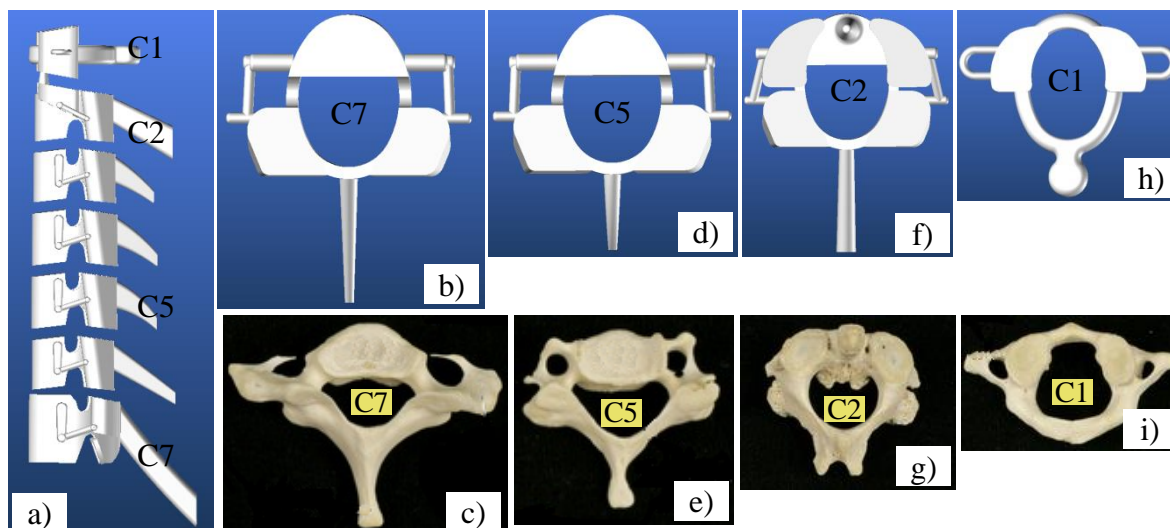
Figure 2.14: Virtual and real model of cervical vertebrae.

The C6, C5, C4, C3, C4, C3 have a slightly smaller vertebral body which leads to a more important spinal process (Figure 2.14(d)(e)). The articular process is higher que la C7 (Figure 2.14(a)). The C2 is very imposing following the integration of the two articular processes designed laterally on the vertebral body Figure 2.14(f)(g)). The dens are perfectly positioned in the axis of the vertebral body. The transverse processes follow correctly the external morphology of the vertebral body. The whole gives a compact overall shape respecting the morphology of the C2. The spinous process is more pronounced at its tip but needs to be reduced by adjusting the length of the director curve as for the dorsal vertebrae. the modelling of the C1 by a ring is very representative of it

(Figure 2.14(h)(i)). The addition and proper sizing of the joint process give it its overall shape. The two transversal processes perfectly complete the whole.

The addition and proper sizing of the joint process gives its overall shape. The two transversal approaches properly complete the whole part. As it is already noticed, the spinal column is an exact stack of vertebrae evolving according to a defined curve in a 3D space. This curve characterizes the morphology of the person, in particular the posture. To describe the 3D path of this kinds of the curve, we have chosen to portray it in the two main planes, namely the sagittal plane and the coronal plane. Our model segmented such path into 24 portions represented by a set of line D_{tn} on which it will align the 24 vertebrae of the spine. t represents the type of vertebra (*C*: cervical, *D*: dorsal, *L*: lumbar) and *n* the number of vertebra in its category. Each line is defined by polar coordinates (l_{tn}, α_{tn}, β_{tn}) in reference located at the lower end of the line. l_{tn} represents the length of the line equal to the height of the vertebra and its upper intervertebral disc. α_{tn}, β_{tn} respectively represents the two polar angles of the lines projected on the sagittal and coronal planes. It is important to note that the rising dependency of vertebrae from their stacking is created when developing straight lines one after the other in the rising direction of the spine. This dependence is obtained by creating the coordinate system of the next (upper) vertebra at the end of the right of the previous (lower) vertebra.

The total length L_t of the spine is the only parameter to give the model for parameterizing the length l_{tn} of each vertebra/disk. The modelling process has used the vertebral ratios of research work as shown in Table 2.1[6][35]. To take into account the 3D deformation of the spine in atypical cases of scoliosis, each vertebra can rotate by an angle γ_{tn} on the axis of the line assigned to it (Figure 2.15(b)). The first tests were carried out with a spine perfectly aligned vertically with different lengths L_t (Figure 2.15(a)). The test has used different length of a spine from L_t=750mm to L_t=550mm. These values are very representative of reality. The results of Figure 2.15(a) shows that all vertebrae re-align perfectly with each other while reducing their volume. The first part of the table represents each vertebra's height based on the ratios. The three other tests separately show the spinal column's deformation in the three characteristic planes: sagittal, coronal, and transverse.

Table 2.1: Relative lengths of human vertebral bony segments.

Segment	Percentage of spine	Cumulative percentage of spine
C1	3.2	3.2
C2	3.2	6.4
C3	2.8	9.1
C4	2.7	11.9
C5	2.7	14.6
C6	2.6	17.2
C7	3.1	20.2
D1	3.4	23.6
D2	3.7	27.3
D3	3.4	31.1
D4	3.9	34.9
D5	3.9	38.8
D6	4.2	42.9
D7	4.3	47.3
D8	4.5	51.7
D9	4.6	56.3
D10	4.8	61.2
D11	5.1	66.2
D12	5.4	71.7
L1	5.7	77.3
L2	5.8	83.1
L3	5.7	88.8
L4	5.7	94.6
L5	5.5	100

These deformations were carried out with the same length of spine L_t =750mm to show its impact on the overall height of the person following the first two deformations, the third is not affecting the height. This parametric independence will be beneficial to represent all types of scoliosis deformations in the next process. Table 2.2 represents the rotation angle of each vertebra in the sagittal plane. The third part of the Table 2.2 represents the angle of rotation of each vertebra in the coronal plane. The last one represents the rotation of each vertebra in its transverse plane, i.e., its rotation on itself.
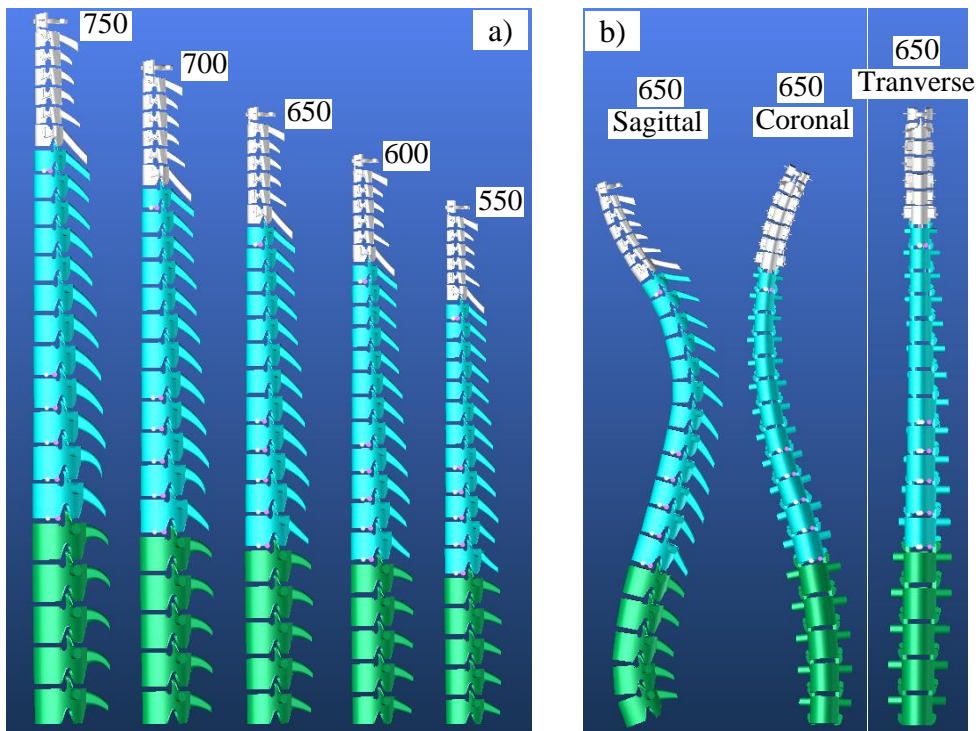
Figure 2.15: (a) Straight spines with different values of L_t and, (b) Spine deformation in the 3 planes.

2.3.2   Developing adaptive vertebra model in a body

The advantage of our adaptive spine model is its ability to integrate with the human body with or without scoliosis. In order to facilitate such process, we have scanned a patient with specific deformability in the Human Solutions body scanner and obtain its 3D digital representation. After cleaning the data from the scanner, it is then imported the particular person's surface model, representing the outer shell of their body into the 3D Design Concept software that we used to create our spine model. The integration of the spine into this body was carried out in several stages. The first step was to assign the correct L_t value to the spine model Figure 2.15: (a) Straight spines with different values of Lt and, (b) Spine deformation in the 3 planes. Since, the person was scanned by the EOS scanner, the value was calculated the height L_t of the spine (L_t =620mm).

The second step was to position the start of the spine in the right place. The vertebra L5 was our reference vertebra, which was placed as close as possible on the sacrum's high part. This position is somewhat imprecise vertically but is more easily located between the two buttocks. This position will evolve slightly until the positioned the C7 vertebra were achieved in its right position, a position where very easily perceptible.

Table 2.2: Values of l_{tn} for the different values of L_t, Values of the deformation angles α_{tn}, β_{tn}, γ_{tn} in sagittal, coronal, transverse planes.

Segment	H_{750}	H_{700}	H_{650}	H_{600}	H_{550}	Sagital	H_{650}	Coronal	H_{650}	Transverse	H_{650}
l_{C1}	18	16,8	15,6	14,4	13,2	α_{C1}	10	β_{C1}	-26	γ_{C1}	15
l_{C2}	18,75	17,5	16,25	15	13,75	α_{C2}	15	β_{C2}	-23	γ_{C2}	12
l_{C3}	19,5	18,2	16,9	15,6	14,3	α_{C3}	20	β_{C3}	-20	γ_{C3}	9
l_{C4}	20,25	18,9	17,55	16,2	14,85	α_{C4}	25	β_{C4}	-17	γ_{C4}	6
l_{C5}	20,25	18,9	17,55	16,2	14,85	α_{C5}	28	β_{C5}	-14	γ_{C5}	3
l_{C6}	19,5	18,2	16,9	15,6	14,3	α_{C6}	30	β_{C6}	-11	γ_{C6}	0
l_{C7}	23,25	21,7	20,15	18,6	17,05	α_{C7}	36	β_{C7}	-8	γ_{C7}	-3
l_{D1}	25,5	23,8	22,1	20,4	18,7	α_{D1}	33	β_{D1}	-6	γ_{D1}	-6
l_{D2}	27,75	25,9	24,05	22,2	20,35	α_{D2}	27	β_{D2}	-3	γ_{D2}	-9
l_{D3}	27,75	25,9	24,05	22,2	20,35	α_{D3}	17	β_{D3}	0	γ_{D3}	-12
l_{D4}	29,25	27,3	25,35	23,4	21,45	α_{D4}	14	β_{D4}	3	γ_{D4}	-15
l_{D5}	29,25	27,3	25,35	23,4	21,45	α_{D5}	8	β_{D5}	6	γ_{D5}	-18
l_{D6}	31,5	29,4	27,3	25,2	23,1	α_{D6}	1	β_{D6}	9	γ_{D6}	-21
l_{D7}	32,25	30,1	27,95	25,8	23,65	α_{D7}	-10	β_{D7}	12	γ_{D7}	-24
l_{D8}	33,75	31,5	29,25	27	24,75	α_{D8}	-13	β_{D8}	15	γ_{D8}	-27
l_{D9}	34,5	32,2	29,9	27,6	25,3	α_{D9}	-14	β_{D9}	18	γ_{D9}	-24
l_{D10}	36	33,6	31,2	28,8	26,4	α_{D10}	-15	β_{D10}	21	γ_{D10}	-21
l_{D11}	38,25	35,7	33,15	30,6	28,05	α_{D11}	-16	β_{D11}	18	γ_{D11}	-18
l_{D12}	40,5	37,8	35,1	32,4	29,7	α_{D12}	-18	β_{D12}	15	γ_{D12}	-15
l_{L1}	42,75	39,9	37,05	34,2	31,35	α_{L1}	-15	β_{L1}	12	γ_{L1}	-12
l_{L2}	43,5	40,6	37,7	34,8	31,9	α_{L2}	-11	β_{L2}	9	γ_{L2}	-9
l_{L3}	42,75	39,9	37,05	34,2	31,35	α_{L3}	-8	β_{L3}	6	γ_{L3}	-6
l_{L4}	42,75	39,9	37,05	34,2	31,35	α_{L4}	4	β_{L4}	3	γ_{L4}	-3
l_{L5}	41,25	38,5	35,75	33	30,25	α_{L5}	20	β_{L5}	0	γ_{L5}	0

The third step was to follow the path of the vertebral column by gradually gluing the spinous process of each vertebra into the significant hollow which was created by at the back of the body. The angular parameters of each vertebra α_{tn}, β_{tn} have been adjusted gradually from bottom to top (Table 2.3). The parameters γ_{tn} have been set to zero since it is impossible to determine their specific value at this point. However, the analysis of the two coronal views shows that the double deflection of the spine forming, and S is similar. Since there was a front view obtained from the EOS scanner and a back view in the Design concept software, it is possible to have a symmetrical visual of the S orientation. The analysis of the two sagittal views shows that the path of the spine in the patient's back follows in an identical way of the significant hollow. Figure 2.16 shows the values obtained for patient using the EOS images and the integrations of model spine in the patient's body.

Table 2.3: Patient's values of l_{tn}, α_{tn}, β_{tn}, γtn for $L_t = 620$mm.

Segment	H_{620}	Sagital	H_{620}	Coronal	H_{650}	Transverse	H_{620}
l_{C1}	14,88	α_{C1}	10	β_{C1}	1	γ_{C1}	0
l_{C2}	15,5	α_{C2}	15	β_{C2}	1,5	γ_{C2}	0
l_{C3}	16,12	α_{C3}	20	β_{C3}	2	γ_{C3}	0
l_{C4}	16,74	α_{C4}	25	β_{C4}	2,5	γ_{C4}	0
l_{C5}	16,74	α_{C5}	28	β_{C5}	3	γ_{C5}	0
l_{C6}	16,12	α_{C6}	30	β_{C6}	3,5	γ_{C6}	0
l_{C7}	19,22	α_{C7}	36	β_{C7}	4	γ_{C7}	0
l_{D1}	21,08	α_{D1}	33	β_{D1}	0	γ_{D1}	0
l_{D2}	22,94	α_{D2}	27	β_{D2}	2,5	γ_{D2}	0
l_{D3}	22,94	α_{D3}	17	β_{D3}	7,5	γ_{D3}	0
l_{D4}	24,18	α_{D4}	14	β_{D4}	12,5	γ_{D4}	0
l_{D5}	24,18	α_{D5}	8	β_{D5}	10	γ_{D5}	0
l_{D6}	26,04	α_{D6}	1	β_{D6}	7,5	γ_{D6}	0
l_{D7}	26,66	α_{D7}	-10	β_{D7}	5	γ_{D7}	0
l_{D8}	27,9	α_{D8}	-13	β_{D8}	2,5	γ_{D8}	0
l_{D9}	28,52	α_{D9}	-14	β_{D9}	0	γ_{D9}	0
l_{D10}	29,76	α_{D10}	-15	β_{D10}	-2,5	γ_{D10}	0
l_{D11}	31,62	α_{D11}	-16	β_{D11}	-2,5	γ_{D11}	0
l_{D12}	33,48	α_{D12}	-18	β_{D12}	-2,5	γ_{D12}	0
l_{L1}	35,34	α_{L1}	-15	β_{L1}	-2,5	γ_{L1}	0
l_{L2}	35,96	α_{L2}	-11	β_{L2}	0	γ_{L2}	0
l_{L3}	35,34	α_{L3}	-8	β_{L3}	2,5	γ_{L3}	0
l_{L4}	35,34	α_{L4}	4	β_{L4}	2,5	γ_{L4}	0
l_{L5}	34,1	α_{L5}	20	β_{L5}	2,5	γ_{L5}	0

Figure 2.16: EOS images of patient (a) side and (d) front view, and spine integrated in the patient's body (b) side and (c) front.

51

2.4 Conclusion

This chapter has proposed a method of constructing a 3D spine model come from of complicated anatomical shape of human vertebrae.

The first step was to analyze the different functions of the vertebrae in order to understand this very complex part of the body. This analysis led us to 3 types of 3D representation, already specified by the medicine, associated with the lumbar, dorsal and cervical part.

Then, the parameterization of a vertebra being complex in itself, it was necessary to find a common morphology to the 3 types leading us to the development of a generic 3D vertebra model. Further developments had to be carried out for the cervical vertebrae given their very specific morphology.

In order to validate the 3D spine adaptive model, a medical scan of a person from the EOS scanner was performed. The size and position of each vertebra were measured manually from 2D images of that person's spine. These measurements were imported into the 3D adaptive model in order to adjust the size and position of each vertebra to finally obtain a 3D representation of the person's vertebral column. It was by comparing the results of this 3D path with that taken from real images from the EOS scanner that the entire modelling was validated.

At this point, we notice that a weak point exists which is the manual measurement of the size and position of each vertebra. This brings us to the next chapter which is the implementation of a measurement strategy from the digital processing of images from the EOS scanner.

CHAPTER 3: EOS IMAGING AND VERTEBRAE DETECTION

The main purpose of this chapter is propose an automated method to calculate the length and angles of vertebrae from diffrent kind of radiology images(in our cas EOS image) for scoliosis patients to acquire the parameters needs of our parametric model, these data generally being obtained by an operator using software such as a "DIACOM reader" and "emedia". This automation by image processing therefore has a dual purpose, facilitating the work of hospital staff and making the link between the patient and our spine3D model.

In the context of the diagnosis of idiopatic scoliosis as well as its evolution, the Cobb angle plays a major role and can be deduced from the parameters of our model. The measurement of this angle is usually done manually from an anteroposterior radiograph by selecting the most oblique vertebra at the top and bottom of the spine. Here we will use an automatic method based on the Keypoint methods. The results of these methods, which are relatively close to deep learning methods, make them an interesting alternative solution without the need for a gigantic database. This method also makes it possible to use the details of the image to its full capacity, so there is no downsizing and while maintaining speed of execution. The algorithm learns to differentiate the different vertebrae by directly locating the vertebral centers. After capturing the vertebrae, the four corner marks of each vertebra are regressed using convolutional layers. We therefore obtain the size and angle positions of the vertebrae which are the input data for our model.

3.1 EOS Imaging

Based on a Nobel Prize-winning invention in physics in the field of particle detection, the EOS X-ray machine EOS™ can capture two-screen direct X-ray images by scanning the entire body gap in a vertical and physiological load [94]. Tolerance position, using very low doses of radiation. Capturing old mechanically calibrated posterior and lateral images can reconstruct the three-dimensional (3D) skeletal system's surface using special software. Parts of the skeletal system appear in 1: 1 scale X-ray images and reconstructed 3D models for actual size and volume, so the parameters of the spine and vertebrae, lower limb axes and angles, as well as any relevant clinical parameters in practice Orthopedics can be very accurately measured and calculated. Visualization of 3D reconstructed models in different views by sterEOS 3D software provides top view images to analyze the rotational conditions of the lower limbs, joints, and spinal deformities

in the horizontal plane, which provides revolutionary new possibilities in Provides orthopedic surgery, especially in spinal surgery.

George Sharpack was awarded the Nobel Prize in Physics in 1992 for his research into particle detection for his invention of a multi-wire fitting chamber and a gas X-ray detector. The most common way to detect modern particles is to measure numbers. Electrons separate from atoms after colliding with elementary particles (such as X-ray photons) are called ionization measurements. Suppose ionization occurs in a particular gas mixture. In that case, the X-ray photons break the gas atom's electrons, the number of which is proportional to the kinetic energy of the photons. These released electrons accelerate in an electron field and collide with other gas atoms from which many extra electrons are broken, significantly increasing the detectable number of electrons. The avalanche's electron beam creates an electrical discharge in a system consisting of several thin wires pulled together.

This complex grid system forms a typical multi-stranded enclosure that provides a uniform electron field needed to collect electrons. In this way, a well-proportioned wire enclosure can count particles and show the level of their rotation circuit.

Although extremely sensitive to the surface of a photon, this new method of X-ray detection is not affected by scattered radiation. This feature has created an opportunity to create a new diagnostic radiograph, which can significantly reduce X-rays while increasing the quality of X-rays. This new technology has made it possible to create higher-quality images with a wider dynamic range. Images with specific shades of gray have increased to 30-50 thousand compared to traditional X-ray images with only a few hundred images. It also produces images with higher contrast and resolution, meaning the pixel resolution of the image increases to 254 micrometers. Full digital image processing provides an opportunity similar to the "window" process in computed tomography (CT), in which images are digitally enhanced after processing to show only a predefined gray spectrum with radiation-absorbing characteristics in the body. Be more appropriate or user interest [95].

The X-ray machine includes this new diagnostic technology consisting of two interconnected pairs of a linear radiation source and a 45 cm wide detector placed perpendicular to each other, in front and side positions (Figure 3.1). Inside this X-ray machine, called the EOS ™ 2D / 3D, two-screen X-ray images are captured simultaneously by the simultaneous vertical motion of two pairs of X-ray tubes and a detector. During this vertical movement, an area 170 cm high and 45 cm wide is covered, resulting in high-quality X-ray (AP) and lateral (LAT) X-ray images in just ten to 25 seconds Figure 3.1Figure 3.2 [37].

Figure 3.1: Operational principles of the EOS™ 2D/3D system. Perpendicularly placed, vertically moving, co-linked units of X-ray tubes producing very thin collimated X-ray beams collected by unique line detectors with Nobel Prize winning technology result in simulation.

The machine with two part of perpendicularly positioned radiation sources and detectors not only allows simultaneous capture of AP and LAT radiographs but also enables a precise three-dimensional (3D) reconstruction of vertebrae, pelvis, and other parts of the skeletal system because images are captured in a spatially calibrated manner (Figure 3.3).This 3D reconstruction is also a result of a new technical achievement, developed in collaboration by the Biomechanical Laboratory (Laboratoire Bioméchanique [LBM]) of the Arts et Métiers ParisTech in Paris, France and the Orthopaedic and Imaging Laboratory (Laboratoire de Reherche en Imagerie et d'Orthopédie [LIO]) of the École de Technologie Supérieure de l'Université du Québec in Montreal, Canada [96].

Figure 3.2: Two-dimensional digital X-ray images captured by the EOS™ 2D/3D system. From left to right and top to bottom: full body biplanar lateral and posteroanterior (PA) images; PA thorax; PA pelvis; and PA right knee images. 1:1 scale, high contrast.

Figure 3.3 Full-body surface reconstructed 3D model based on an EOS™ 2D examination. Simultaneously captured, spatially calibrated biplanar X-ray images enable performing surface 3D reconstruction of the spine, pelvis and lower limb providing visual and parametric.

The reconstruction method is based on virtual and general reconstruction of the natural human skeleton. The three-dimensional shape of the bones in the three-dimensional virtual skeleton was determined by the three-dimensional coordinates of specific points on the bone surface. Depending on the shape's complexity, the number of points to accurately describe a three-dimensional envelope of the corresponding bones varies from 400 to 9000. Using homothetic transformation, the law of parallel similarity, combined with complex statistical inference, is required to define so-called reference points necessary for determining the exact shape of bones. 3D theoretical models were created based on 3D CT models and statistical finite element models using these reference points. One of the most complex models is the spine, whose reference points and theoretical three-dimensional models have been created by measuring 1628 individual vertebrae and reconstructing 96 separate vertebrae in three dimensions [95][97][98].

Visual information obtained from X-ray and LAT X-ray images recorded simultaneously also allows the reference points (e.g., the geometric center of the femoral head) to be identified in X-ray images. Some reference points can be detected in X-ray AP and LAT (so-called stereo reporter) images and correspond to specific descriptive sources. Other reference points can be attached to a descriptive reference but are only visible on the one-page image and not on the other. Hence, their exact location depends on the spatial orientation of the object.

In addition to the reference points, the bone contour (e.g., the femoral head contour) can also be displayed by the general 3D model. The virtual model overlaps on both X-ray images. Radiological lines and virtual bone lines do not necessarily overlap in three dimensions. The virtual model can use its reference points and lines, using nonlinear deformation, translation, or rotation as long as the radiological and virtual bone lines match. The virtual bone model best matches the modeled bone Figure 3.4.

EOS's three-dimensional reconstruction for various bones (vertebrae, femur, tibia) has been confirmed first using dry anatomical preparations in vitro and in vivo. A three-dimensional volumetric reconstruction based on CT images with 1 mm incisions for the limbs and 2 mm incisions for the spine was performed and used as a reference in each case. 3D surface reconstruction was then used in the same patients and anatomical dummies similar to EOS, then the results of the two methods were compared.

Figure 3.4: EOS™ 3D models of the spine with pelvis (left) and lower limbs with pelvis (right). Reconstructed 3D models can be displayed by a patented software in predefined standard planes (frontal, sagittal, horizontal) or freely rotated through 360° to present on.

The mean difference in 95% of cases was 0.9 mm with a maximum deviation of 2.4 mm. In vivo measurements, the most significant difference was less than 1.5 mm, even in severe clinical deformities such as ample scoliotic curves or severe osteoarthritis of the knee, i.e., the results were comparable to direct measurements based on 3D CT reconstruction of dry anatomy specimens. The final results of all validation studies proved that EOS ™ 3D surface reconstruction is equally accurate and easily related to 3D reconstruction while using only a fraction of the radiation dose. The dose of radiation absorbed by different organs during the whole-body examination EOS ™ 2D / 3D required for three-dimensional surface reconstruction was shown to be 800-1000 times less than the amount of radiation during the CT scan required for 3D volumetric reconstruction. Due to the known biological side effects of ionizing radiation, the benefits of EOS are easily understood, especially in pediatric orthopedic surgery.

The most important practical advantage of EOS ™ in everyday work is the ability to produce high-quality full-body digital X-rays that are directly available for diagnostic purposes without further processing, with a single examination performed in ten to 25 seconds. To achieve the same results as conventional X-ray radiography, multiple exposures and image processing

(such as suturing) are required, leading to significantly longer examination times with reduced patient efficiency and higher radiation doses per examination Becomes. Due to the significantly higher detector sensitivity and insensitivity to scattered diffuse radiation, the image quality increases dramatically, regardless of the body's area being examined. Another advantage is that images were taken at a 1: 1 scale, objects of actual size, without magnification and distortion, show adverse effects on conventional radiography, which are detected by X-ray detection, and digital processing of raw images disappears. Further processing is optimized for the type of examination performed, with more possibilities to apply the grayscale range and no need for repeated reviews. The system is DICOM compliant; for example, captured images may be stored by standard digital radiology systems and subsequently used or retrieved for 3D reconstructions on a dedicated digital workstation.

3.2   Machine learning

"Machine learning" is one of the "artificial intelligence" methods that gives the system the ability to learn automatically and without explicit planning. In other words, the goal of machine learning is to build intelligent machines that learn from a set of data and experiences. The primary purpose of machine learning is to design and develop intelligent applications to access data and learn.

The first study of neural networks was in 1943, when neurophysiologist Warren McCulloch and mathematician Walter Pitts wrote a paper about neurons. They created a model of this using an electrical circuit, and then the neural network was born. Alan Turing created the world-famous Turing Test in 1950. This test is simple for a computer to pass, it had to be able to convince a human that it is a human and not a machine. In 1952 the first computer program was seen which could learn as it ran by Arthur Samuel. It was a game which played checkers.

Another very prototype of the neural network occurred in 1959, when Bernard Widrow and Marcian Hoff developed two models of them at Stanford University. The first case was called ADELINE and could detect binary patterns. For example, in one bit, it can predict the next. The next generation was called MADELINE and could eliminate echoes in telephone lines, so it had a useful application in the real world. It is still used today. Despite the success of MADELINE, for many reasons, mainly the popularity of Von Neumann architecture, little progress was made until the late 1970s. It is an architecture in which instructions and data are stored in the same

memory, which is understandably simpler than a neural network, and many people built on these programs [99].

In recent years, the availability of large datasets combined with the improvement in algorithms and the exponential growth in computing power led to an unparalleled surge of interest in the topic of machine learning. Nowadays, machine learning algorithms are successfully employed for classification, regression, clustering, or dimensionality reduction tasks of large sets of especially high-dimensional input data[100]. In fact, machine learning has proved to have superhuman abilities in numerous fields (such as playing go [101], self-driving cars [102], image classification [103], etc). As a result, huge parts of our daily life, for example, image and speech recognition [104][105], web-searches [106], fraud detection [107], email/spam filtering [108], credit scores [109], and many more are powered by machine learning algorithms.

3.2.1   Machine learning methods

The field of artificial intelligence (AI) is quite extensive and includes various aspects of logic through text rotation analysis methods. Traditionally, strong artificial intelligence and weak artificial intelligence are distinguished from each other. The first is aimed at creating highly intelligent systems at the human level and ultimately creating thinking machines. Such developments are funded by DARPA [110] for instance. The weakness of AI is to create programs that do this human or animal intellectual ability. For example, the ability to move safely across the country, beehives (ants) or distributed intelligence [111].

During development, AI, being at the cutting age of scientific research, is gradually changing its matter as a science. If in the first steps of the development, its scope of interests included such problems as bio-identification, text recognition, etc., later they transformed into the scope of technologies used in applied sciences, developments and industries [112]. One of the most successful aspects of AI is machine learning (ML). ML has been used successfully to solve a variety of problems.

3.2.2 The difference between deep learning and machine learning
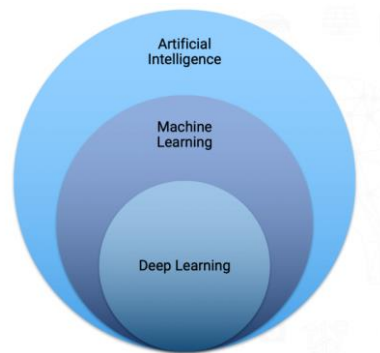
The 3 concepts of artificial intelligence (AI), machine learning (ML), and deep learning (DL) are often confused and sometimes confused. Deep Learning includes concepts and algorithms inspired by the artificial neural networks that make up the human brain's structure. In other words, Deep Learning is a subset of machine learning, and machine learning itself is considered as a subset of artificial intelligence. The image below clearly shows the relationship between these three concepts.

Deep learning algorithms are both a sophisticated and mathematically problem evolution of machine learning algorithms. This field is getting lots of attention these days for good reason: Recent developments have led to results that were not thought to be possible before. In-depth learning describes algorithms that analyze data with a logical structure similar to human inference. Note that this can happen through supervised and unsupervised learning. Deep learning programs use the layered structure of algorithms called artificial neural networks (ANNs) to achieve this. The design of such an ANN is inspired by the biological neural network of the human brain and leads to a learning process that is far more capable than standard machine learning models (Figure 3.5).

Deep learning algorithms are machine learning algorithms. Therefore, it is better to think about what makes deep machine learning special. Answer: The structure of the ANN algorithm, less need for human intervention, and larger needs for data. First and foremost, while traditional machine learning algorithms have a relatively simple structure such as linear regression or decision trees, deep learning is based on an artificial neural network. This multilayered ANN is as complex and intertwined as the human brain.
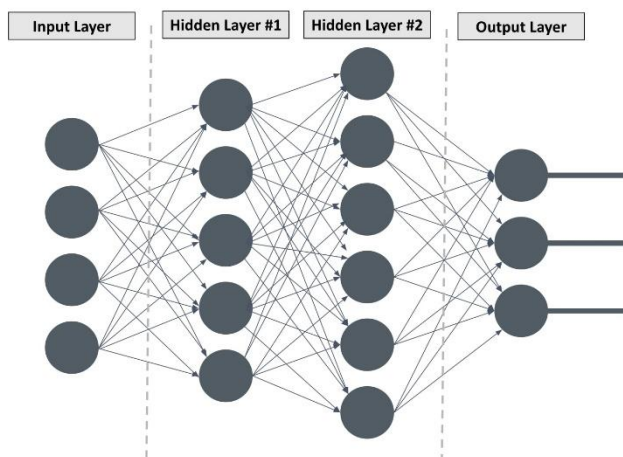
Figure 3.5: A simple artificial neural network.

3.2.3   Deep Learning

Deep Learning has evolved in the digital age, which has created data called Big Data. This data is collected from social media websites, search engines, and e-commerce platforms. This big data is available and shared through supercomputers.

The idea of deep learning can be described as follows:

However, this big data is usually unstructured. It may take years for humans to discover and extract relevant information from it. Relying on some AI-based systems, companies realize the potential they need and avoid wasting capital. Computers with sufficient capacity for deep learning models and big data are now available to train deep learning neural networks. It is called deep learning because neural networks have different and deep layers that make learning possible. Almost any problem that needs to be thought about; Deep learning can be trained [113].

The function of neural networks is improving daily because they are constantly fed and trained with more information. This distinguishes deep learning from other machine learning techniques. In addition to increasing information, deep learning algorithms take advantage of the more powerful computing power available today. The development of artificial intelligence has also had a significant impact on this process. Artificial intelligence as a service has given smaller

organizations access to artificial intelligence technology and the artificial intelligence algorithms required for deep learning.

Feature learning refers to a set of techniques that can be used to learn a feature—for example, classifying raw data. Feature learning works in the form of an artificial intelligence hierarchy. In addition to scalability, Deep Learning allows us to learn features. In general, it makes it easy for machines to learn complex steps. Deep learning helps to use unknown structures in the input data. In the higher layers, the deep learning features are divided into several layers. Multi-level learning features help machines understand complex deep learning systems.

One of the most common AI-based techniques for big data processing is the learning machine. The self-consistent algorithm is constantly improving and educating itself based on patterns. Deep learning allows machines to solve complex problems even when using a genuinely diverse, unstructured, and corresponding data set. The deeper the learning algorithms, the better the performance.

If a digital payment company is trying to detect fraud in its payment system, it can use machine learning tools. The computational algorithm built into the system can check all transactions. Therefore, according to different data sets, the pattern of anomalies in the system can be observed. These tools do the work automatically and prevent unauthorized access to the systems. Deep Learning is a subset of the Learning Machine network that uses an artificial neural network (ANN) to perform processes.

Artificial neural networks function like human brains made up of neural nodes connected to a network. Analysis in traditional applications is linear; however, deep learning's hierarchical feature analyzes data using nonlinear techniques.

A traditional approach to detecting fraudulent access to a digital system is based on transactions. The first layer of the deep neural network processes data, such as the transaction amount, and transfers it to the next layer. The IPs assigned to users are checked and then sent to the next layer in the second layer. The next level receives and processes the information obtained in the previous layer. In this layer, their geographical location is checked and then transferred to the next layer. In this method, Deep Learning examines patterns and identifies abnormalities. Data is better processed when it comes to this hierarchy. They usually get more data sets to get better returns.

3.2.4   Object detection with deep learning

Object detection is an extremely popular research direction in the vision field. Launched in the 70s, object detection began to be on track until the 90s when computers became powerful and applications plentiful. It is easy for us to recognize objects in the images. After that, however, things become difficult for computers. Adding the different posture of objects and the complex environment around them, object detection is more ambiguous [114][115].

With the increasing amount of detection data, the traditional detection method performance will become saturated [113]. As a result, the detection performance will gradually improve, yet the improvement decreases after a certain amount of data [116]. However, the method of deep learning is different. While the data of the scene distribution accumulates, the detection performance promotes continuously [117].

3.2.5   Classical Object Detection Methods Based on Regression

Currently, the classical object detection methods based on regression are YOLO and SSD. YOLO is a single neural network that can perform object region detection and object classification simultaneously. Unlike early object detection methods based on region proposals, YOLO achieves end-to-end object detection without dividing the detection process into several stages. SSD is a single shot multibox detector that integrates the regression approach of YOLO with the anchor mechanism of Faster R-CNN [118]. On the one hand, the regression approach can reduce the computational complexity of a neural network to improve real-time performance.

On the other hand, the anchor mechanism helps extract features at different scales and different aspect ratios. Moreover, the local feature extraction method of SSD is more reasonable and practical than YOLO's general feature extraction method concerning object recognition. Furthermore, because the feature representations corresponding to different scales are different, a multi-scale feature extraction method [119] has been applied in SSD, thereby enhancing the robustness of object detection at different scales.

Because YOLO divides each image into a fixed grid, the number of detected objects will be limited. For example, consider a grid-scale of $S \times S$, where $S = 7$. Because each grid yields 2 predicted bounding boxes, only 98 predicted bounding boxes are observed in a single detection, which means that no more than 98 objects can be detected at one time. Moreover, because one

grid cell can produce predictions for only one class when objects of two or more classes are in the same grid cell, they cannot simultaneously be identified. For example, if the input image scale is 448×448, no more than two objects can simultaneously be identified in a single 64×64 grid cell, and their classes must be the same. In addition, concerning YOLO, once the input image has passed through twenty-four convolution layers and four pooling layers, little detailed information can be observed in the resulting feature map. Therefore, YOLO has a relatively poor ability to detect dense small objects.

Unlike YOLO, SSD adopts a multi-scale approach, which means that the feature maps that are used to detect different objects are at different scales. Because each feature map is produced from convolution results at the same level, the convolution receptive fields of the different levels must be different in size. In particular, the receptive field of a high-level convolution layer is significantly larger than those of lower layers, and the extracted information corresponding to a high-level feature layer is more abstract. The more abstract the feature extraction information is, the less detailed the information will be thus, SSD detection is also insensitive to small objects.

The formula for calculating the convolution receptive field is as follows:

$$S_{RF}(i) = (S_{RF}(i-1) - 1)N_s + S_f \tag{3.1}$$

where $S_{RF}(i)$ is the size of the convolution receptive field of the i-th layer, is the step length, and S_f is the size of the filter.

SSD adopts the anchor mechanism, for which the detection results are directly related to the size of the default bounding box produced from the anchors. The ratio of the default bounding box to the input image can be calculated according to the formula given in [112]. Furthermore, the relationship between the default bounding box and the input image can then be used to determine the region mapped to the input image. To measure the detection capability of a feature map, the minimal default bounding box scale is selected to observe the minimal region mapped to the input image in the feature map.

The mapping of the default bounding box coordinates to the original image coordinates on the feature map is as follows:

$$x_{min} = \frac{c_x - \frac{w_b}{2}}{w_{feature}} w_{img} = \left(\frac{i + 0.5}{|f_k|} - \frac{w_k}{2} \right) w_{img} \tag{3.2}$$

$$y_{min} = \frac{c_y - \frac{h_b}{2}}{h_{feature}} h_{img} = \left(\frac{j + 0.5}{|f_k|} - \frac{h_k}{2} \right) h_{img} \tag{3.3}$$

$$x_{max} = \frac{c_x + \frac{w_b}{2}}{w_{feature}} w_{img} = \left(\frac{i - 0.5}{|f_k|} + \frac{w_k}{2} \right) w_{img} \tag{3.4}$$

$$y_{max} = \frac{c_y + \frac{h_b}{2}}{h_{feature}} h_{img} = \left(\frac{j - 0.5}{|f_k|} + \frac{h_k}{2} \right) h_{img} \tag{3.5}$$

where (c_x, c_y) denotes the center coordinates of the default bounding box, h_b is the height of the default bounding box, w_b is the width of the default bounding box, hfeature is the height of the feature map, wfeature is the width of the feature map, $|f_k|$ is the size in the k-th feature map, h_{img} is the height of the original image, w_{img} is the width of the original image, and $(x_{min}, y_{min}, x_{max}, y_{max})$ denotes the mapping coordinates of the default bounding box, which is centered at $(\frac{i+0.5}{|f_k|}), (\frac{j+0.5}{|f_k|})$ and scaled to a height of h_k and a width of w_k in the k-th feature map.

If the SSD_300×300 model is adopted, such that the size of the input image is 300×300, the feature maps of the model are mainly produced from the Conv4_3, Conv7, Conv8_2, Conv9_2, Conv10_2, and Conv11_2 layers.

3.2.6   ResNet and its Variants

After AlexNet [62] victory at the LSVRC2012 classification contest, deep Residual Network [119] was arguably the most ground breaking in the computer vision community. ResNet makes it possible to train up to hundreds or even thousands of layers and still achieves compelling performance. Powerful advantage of its representational ability, the performance of many computer vision applications other than image classification have been boosted, like object detection.

Given the global approximation theorem, given the sufficient capacity, we know that a feedforward network with a single layer is sufficient to represent any performance. However, the layer can be huge, and the network is prone to overlying data. Therefore, there is a common trend

in the research community that our network architecture needs to be deepened. Since AlexNet, CNN's most advanced architecture has been delving deeper and deeper. While AlexNet had only 5 layers of convolution, VGG [120] and GoogleNet (codenamed Inception_v1) [121] had 19 and 22 layers, respectively.

3.2.6.1 Variants and Interpretations of ResNet

As ResNet becomes more and more popular in the research community, its architecture is being studied extensively. In this section, I will first introduce several new ResNet-based architectures. Xie et al. [122] proposed a variant of ResNet that is codenamed ResNeXt with the following Figure 3.8:
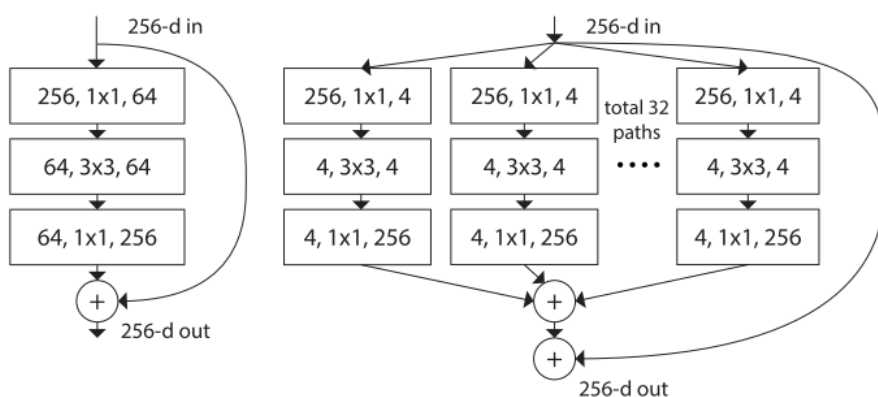
Figure 3.6: left: a building block of [2], right: a building block of ResNeXt with cardinality = 32.

This may seem familiar to you because it is very similar to the Inception module [121], both follow a split-conversion-integration pattern, except in this type, the output of different paths are merged by adding them. While in [121] they are interconnected. Another difference is that in [121], each path is different (1x1, 3x3 and 5x5 convolution) with each other, while in this architecture, all paths have the same topology.

The authors introduced an extraordinary parameter called cardinality - the number of independent paths to provide a new way to adjust the capacity of the model. Experiments show that with increasing cardinality, accuracy can be achieved relatively more efficiently than deep or wider. The authors state that compared to Inception, this new architecture is easier to adapt to new datasets / tasks because it has a simple pattern and only one parameter is too customizable, while

67

Inception has too many parameters. (Such as the core size of the convolution layer of each path) to adjust. This novel building block has three equivalent form as follows in (Figure 3.9):
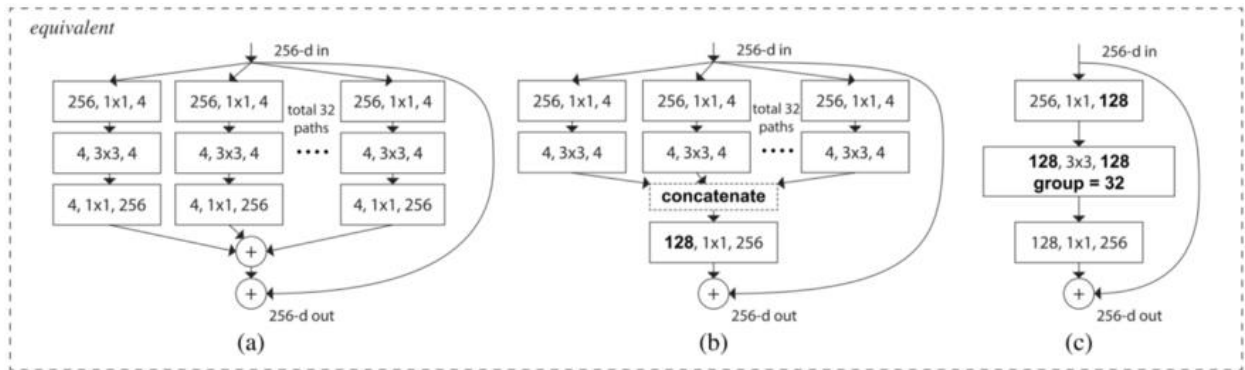
Figure 3.7: Three equivalent form from a building block of ResNeXt with cardinality = 32.

In practice, "split-convert-merge" is usually done by a point grouped convolution layer, which divides its input into groups of feature maps and performs novel convolution, then, the outputs are fed into concatenated by the depth and fed into a 1x1 convolution layer [123].

3.3   Vertebra Detection Method

Recently, critical point-based methods have achieved remarkable performance in human pose joint localization and object detection. An essential step in understanding people in images and video is accurate gesture estimation. By considering an RGB image, we want to determine the exact pixel location of important parts of the body. Gaining an understanding of body posture and limb expression is helpful for higher-level tasks such as performance recognition and serves as an essential tool in areas such as human-computer interaction and animation [124] (Figure 3.8).
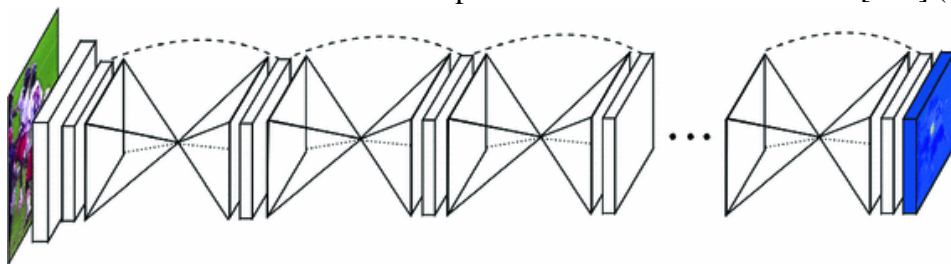
Figure 3.8: Network for pose estimation consists of multiple stacked hourglass modules
which allow for repeated bottom-up, top-down inference.

This work is a convolutional network architecture for the task of human pose estimation. Features are processed across all scales and consolidated to best capture the various spatial relationships associated with the body. It shows how repeated bottom-up, top-down processing used in conjunction with intermediate supervision is critical to improving the network's

performance. This network refers to the architecture as a "stacked hourglass" network based on the successive steps of pooling and upsampling to produce a final set of predictions.

As a well-established problem in vision, pose estimation has plagued researchers with various formidable challenges over the years. A sound pose estimation system must be robust to occlusion and severe deformation, successful on rare and novel poses, and invariant to appearance changes due to factors like clothing and lighting. Early work tackles such difficulties using robust image features and sophisticated structured prediction [125][126][127][128][129][130][131]: the former is used to produce local interpretations, whereas the latter is used to infer a globally consistent pose.

Unlike the regression-based methods, the key point-based methods localize the points without dense mapping. Therefore, it simplifies the network and can consume the higher-resolution input image. In this study, we have used a vertebra-focused landmark detection. A method based on keypoint detection [vertebra-focused landmark detection for scoliosis assessment]. We make the network learn to differentiate different vertebrae by localizing the vertebra centers directly. After capturing the vertebrae, we regress the four corner landmarks of each vertebra using convolutional layers. In this way, we keep the order of the landmarks. Experimental results demonstrate the superiority of our method compared to the regression and segmentation-based methods.

As is shown in Figure 3.9, the Cobb angles are determined by the locations of landmarks. The X-ray images used as the dataset contain 17 vertebrae from the thoracic and the lumbar spine. Each vertebra has four corner landmarks (top-left, top-right, bottom-left, and bottom-right), and each image has 68 landmarks. The relative orders of landmarks are crucial for accurately localizing the tilted vertebrae.

Considering this, we do not localize the 68 points directly from the output feature map since the model cannot guarantee that the detected points will stay at the correct positions, especially when there are false positives, which would lead to incorrect landmark ordering. One strategy is to separate the landmarks into different groups to address this issue, giving an output feature map with channel number $17 \times 4 = 68$. However, since each channel of the output feature map has only one positive point, this strategy suffers from the class imbalance issue between the positive and negative points, which will hurt the model performance.

Another method proposes to first localize the 17 vertebrae by detecting their center points. One advantage of this approach is that the center points will not overlap. Therefore, the center points can identify each vertebra without suffering from the touching problem in segmentation-based methods. After the vertebrae are localized, we then capture the four corner landmarks of each vertebra from its center point. In this way, we can keep the order of landmarks.
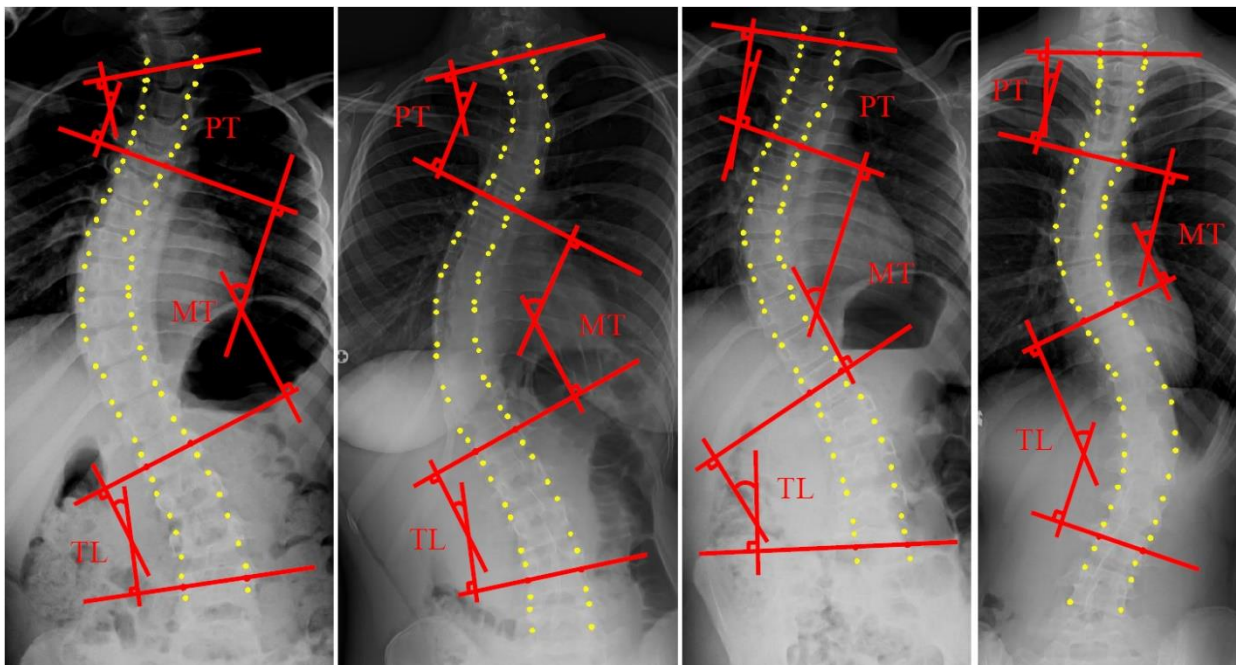
Figure 3.9: Illustration of the anterior-posterior (AP) X-ray images. The ground-truth landmarks (68 points in total, 4 points per vertebra) are shown in yellow points. The coronal Cobb angles of proximal thoracic (PT), main thoracic (MT), and the thoracolumbar (TL).

The landmark detection network is illustrated in Figure 3.10. The inputs of the network are gray-scale images with a size fixed to 1024×512. First, we use ResNet34 [132][133] conv1-5 to extract the high-level semantic features of the input image. Deeper neural networks are more difficult to train by a residual learning framework to ease the training of networks that are substantially deeper than those previously. Then we use the skip connections to combine the in-depth features with the shallow ones to exploit both high-level semantic information and low-level fine details, similar to [133][134]. At layer D2, we construct the heatmap, center offset, and corner offset maps using convolutional layers for landmark localization.

(a) Vertebra-Focused Landmark Detection Network

(b) Landmark Decoding
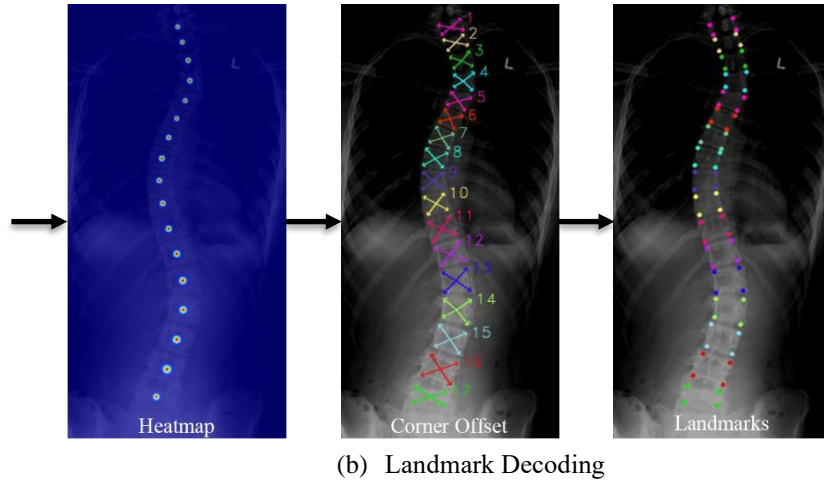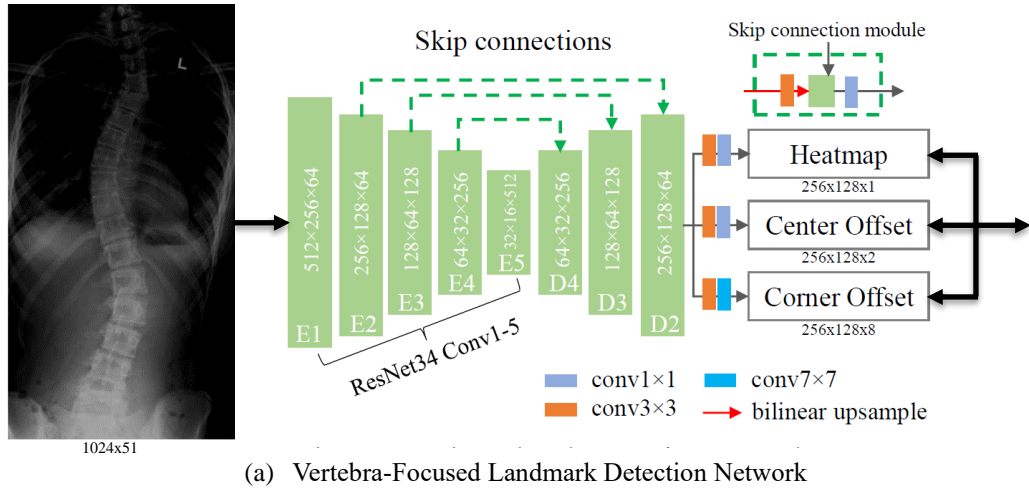
Figure 3.10: (a) The framework of the vertebra-focused landmark detection network. The backbone of the network (i.e., conv1-5) is from ResNet34 [11]. (b) The sizes of the feature maps are presented as height×width×channels. E and D represent encoder and decoder, respective.

3.3.1   Heatmap of Center Points

The key point heatmap is generally used in pose joint localization and object detection. For each point k, its ground truth is an unnormalized 2D Gaussian disk (Figure 3.10(b)) which can be formulated as $\exp\left(-\frac{x^2+y^2}{2\sigma^2}\right)$. The radius σ is determined by the size of the vertebrae [135]. We use the variant of the focal loss to optimize the parameters, the same as [136]:

$$L_{hm} = -\frac{1}{N}\sum_i \begin{cases} (1-p_i)^\alpha \log(p_i) & y_i = 1 \\ (1-y_i)^\beta (p_i)^\alpha \log(1-p_i) & \text{otherwise} \end{cases} \tag{3.6}$$

Where *i* indexes to each position of the feature map. *N* is the total number of positions on the feature map, p_i and y_i refer to the prediction and ground-truth values, respectively. We set the parameters $\alpha = 2$ and $\beta = 4$ [135].

3.3.2   Center Offset

As shown in Figure 3.10(a), the output feature map of the network is downsized compared to the input images. This saves computational cost and alleviates the imbalance between the positive and negative points due to the reduced output resolution. Consequently, a position (*x,y*) on the input image is mapped to the location ($\left\lfloor \frac{x}{n} \right\rfloor, \left\lfloor \frac{y}{n} \right\rfloor$) of the downsized feature map, where *n* is the downsampling factor. After extracting the center points from the downsized feature map, we use the center offset to map the original input image's points. The center offset is defined as:

$$\left(\frac{x}{n} - \left\lfloor \frac{x}{n} \right\rfloor, \frac{y}{n} - \left\lfloor \frac{y}{n} \right\rfloor \right) \tag{3.7}$$

The center offsets at the center points are trained with L_{hm} loss.

3.3.3   Corner Offset

When the center points of each vertebra are localized, we trace the four corner landmarks from the vertebra using corner offsets. The corner offsets are defined as vectors that start from the center and point to the vertebra corners (Figure 3.10(b)). The corner offset map has 4×2 channels. We use L1 loss to train the corner offsets at the center points.

3.4   Experimental Details

3.4.1   Dataset

We use training data (580 images) of the public AASCE MICCAI 2019 challenge as our dataset. All the images are anterior-posterior X-ray images. Specifically, we use 60% of the dataset for training (348 images), 20% for validation (116 images), and 20% for testing (116 images). Each image contains 17 vertebrae from the thoracic and lumbar spine. Each vertebra is located by 4 corner landmarks. The ground-truth landmarks (68 points per image) are provided by local clinicians. The Cobb angle is calculated using the algorithm provided by AASCE. The input images vary in sizes ($\sim 2500 \times 1000$).

3.4.2   Implementation

We implement our method in PyTorch with NVIDIA K40 GPUs. The backbone network ResNet34 [19] is pre-trained on ImageNet. Other weights of the network are initialized from a standard Gaussian distribution. We fix the input resolution of the images to [137] 1024×512, which gives an output resolution of 256×128. We adopt the standard data augmentation to reduce overfitting, including random expanding, cropping, contrast, and brightness distortion. The network is optimized with Adam (an algorithm for first-order gradient-based optimization of stochastic objective functions, based on adaptive estimates of lower-order moments, [137] with an initial learning rate 2:5×10−4. We train the network for 100 epochs and stop when the validation loss does not decrease significantly.

3.5   Results

The vertebra-focused landmark detection model has the ability to identify the vertebra according to their global morphology features through center localization. After using the model for the EOS image, it localizes the vertebra centers, based on which it then traces the four corner landmarks of the vertebra through the learned corner offset. Through the corners, the length of each vertebra is the average distance between two points of the corners on the left side of the vertebra and the right side (Figure 3.11(b)). The vertical axis is passed from the vertebra center (Figure 3.11 (d)).
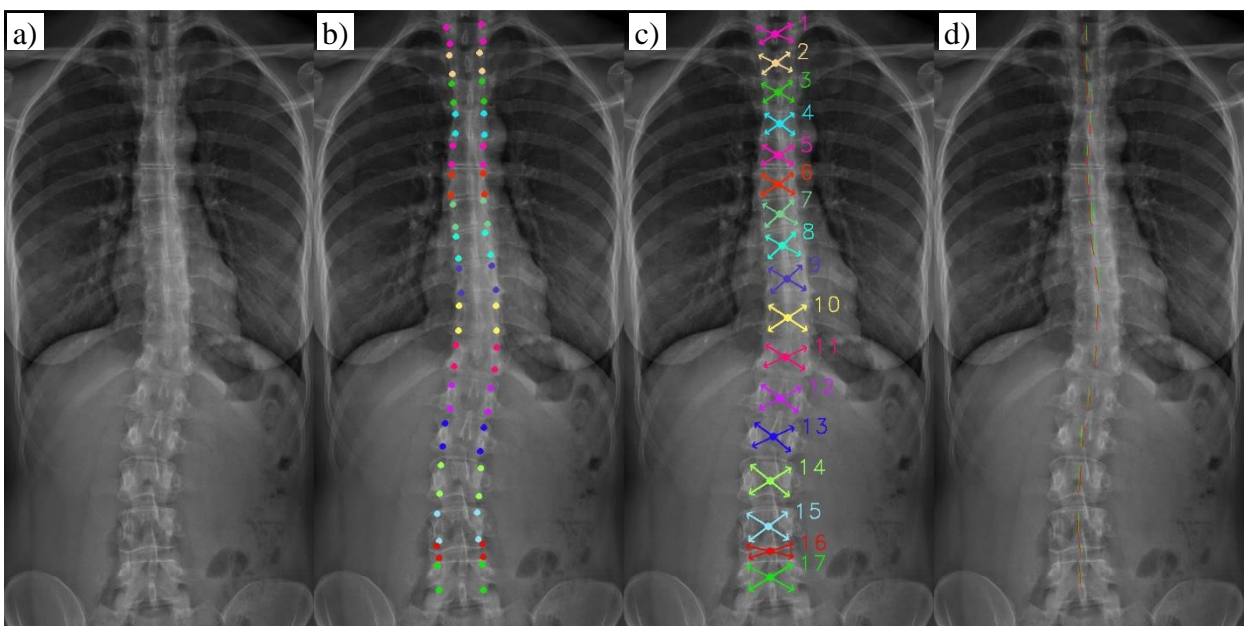
Figure 3.11: a) EOS image. b) Four corner landmarks of the vertebra. c) Location the vertebra centers. d) The angles of vertebra on the vertical axis (coronal angle).

73

3.5.1   Comparison between Manual and Automatic Model

This section compares the data calculated by the vertebra-focused landmark detection model with the data obtained manually by *scan plus* software from *e.media*.

As it can be seen from Figure 3.12 and **Error! Reference source not found.**, there is a mismatch between the data extrapolated from the model and the data obtained manually. This can be attributed to a number of factors. One such factor is the resolution of the sample images used to train the model. The low resolution of a jpeg image cannot compare to that of a DICOM image, and this results in a loss of information which imparts some uncertainty in the final result. Moreover, human error mast be taken into account for what concerns the manually measured data: for each vertebra, the operator must select the relative horizontal axis of reference in order to be able to extrapolate the corresponding angle. Therefore, the chance of error (due to the fact that no human possesses perfect vision) increases. Nonetheless, after having taken into account all these considerations, we can state that the calculated data and the manually measured data (both the angles and the lengths of the vertebrae) presents a good level of agreement.

Figure 3.12 shows that the value of coronal angles in some vertebra is almost the same, like L_4, L_5, D_6. In this case, as in Figure 3.11 is shown the vertebra's edges in these vertebras are sharper, detecting from the model, and especially for an operator to calculate manually, would be more accurate. The significant difference is in those part of image which the vertebra's edge is not distinguishable from the edge of the organs, such as lung and heart in the chest for third, fourth and nineth dorsal vertebra. Moreover, for vertebrae length there are significant difference in D_3,
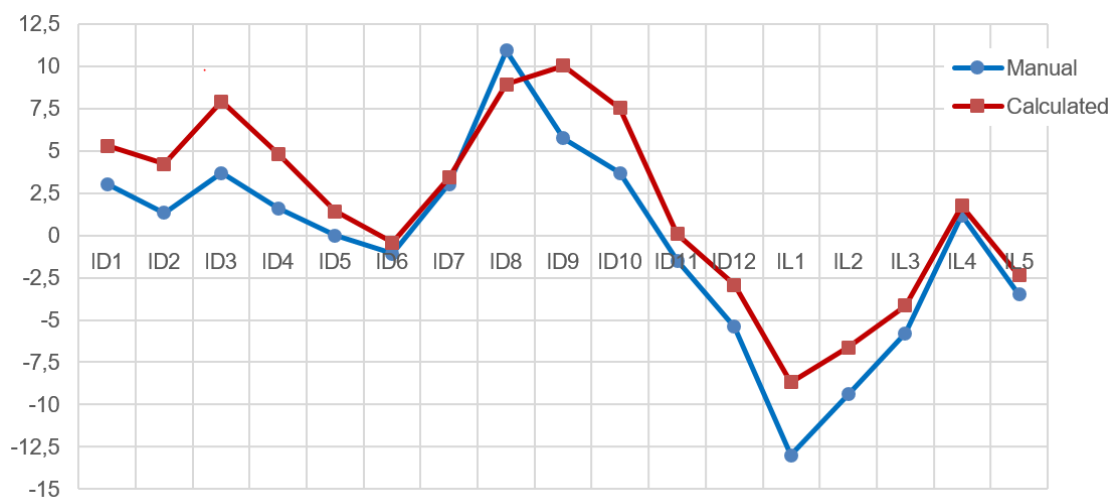
Figure 3.12: Coronal angles.

D_{10} and L_3 (**Error! Reference source not found.**). These errors have same reason of errors in Figure 3.12, which is the four corner landmarks detection as the first step.
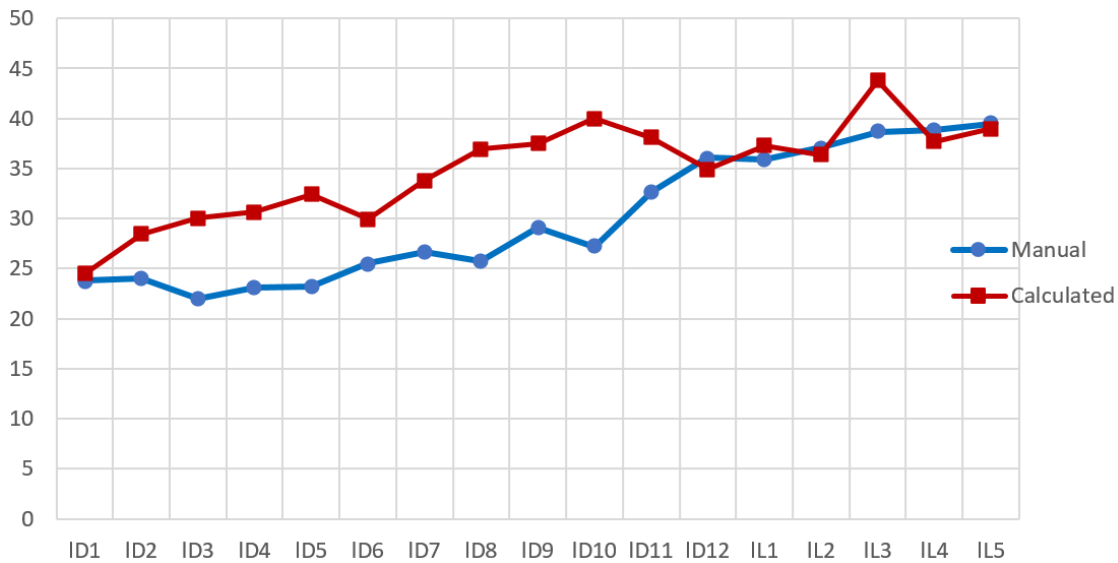
Figure 3.13 : Length of vertebra.

3.6 Conclusion

In this chapter, we have used a vertebra-focused landmark detection method that traces the corner landmarks of a vertebra from its center point. The strategy of predicting center heatmaps enables this model to identify different vertebrae and allows it to detect landmarks robustly from the low contrast images and ambiguous boundaries. However, the accuracy of detection depends on the number of images the model is trained with. At the end, by having the corners of each vertebra, the length and the angle of vertebra is calculated.

By comparing the results with manual data which are obtained from a software tool, we can approve our result and we can also propose the model to calculate the angle and length vertebra especially in our case and in general for designing garment from vertebrae data. However, we should consider deep learning algorithm are strongly depends on quality of databased, such as the image's resolution and the number of images, as much as possible, databased should be vast to train algorithm with high accuracy. The main difficulty in this chapter was finding an acceptable database for sagittal view, at least as much as coronal view to calculate sagittal angles. Unfortunately, this databased was not accessible, so in next chapter for sagittal angles the manual data is used.

CHAPTER 4: 3D PARAMETRIC ADAPTIVE TRUNK MODEL

The objective of this chapter is to develop a 3D parametric adaptive trunk model that has the ability to deform in 3D depending on the path of the spine of a person suffering from scoliosis.

For this, each rib is connected to each vertebra as nature requires. So, naturally, the slightest change in the position of a vertebra causes a change in the position of the associated rib. The morphological analysis of each rib is essential to define the model of each one, which can be grouped into different generic models according to their category.

As the sternum closes the thoracic cavity via the costal cartilage, its analysis, modeling, and association with models of the spine and ribs leads to a deformable 3D model of the thoracic cavity. This deformable 3D model managed by the spine must also be managed by the compressibility or extensibility of the costal cartilage. The sternum was considered non-deformable in our study setting.

The mobility of the scapular girdle, made up of the clavicles and scapulae, reflects the strong deformations in the back by the offset of the scapulae and at the level of the shoulders by the offset of the clavicles. This phenomenon is mainly transmitted by the top of the sternum, the position of which is managed by the first two ribs and the rotation of the sternum imposed by the other ribs. Taking these deformations into account requires developing precise models of the clavicles and scapulae, but also managing the position of the scapulae in relation to the related ribs to avoid their interpenetrations. This comes down to taking into account the role of the muscular system associated with the scapulae.

The different models must be adaptive to adapt to the size of a given person. For this, a common and unique parameter must manage the dimension of each model. We took the one that similarly manages the dimension of the vertebrae of the spine.

4.1 Trunk analysis

A morphological analysis of each entity of the trunk must be carried out to set up the different generic models of the thorax. This scapular belt will be connected and to the model of the spine.

4.1.1   The Thorax

One of the essential functions of the rib cage is to protect the vital organs of our body. The rib cage protects the lungs and the mediastinum, which is the area between the two lungs. The heart, esophagus, trachea, and the two bronchial tubes are the most important organs in this area. Other organs such as the large blood and lymphatic vessels and nerves also pass through this area. This protection is conical in shape to adapt perfectly to the overall shape of these different vital organs, guided essentially by the shape of the lungs. The rib cage is made up of 12 pairs of ribs, which, when attached to the sternum (Figure 4.1(a)), must be classified into three categories: true, false, and floating ribs. The first seven ribs (true ribs) are connected to the sternum (sternocostal joints) through a fibrous tissue called costal cartilage. The next three (false ribs) are connected indirectly to the sternum via the seventh costal cartilage (costochondral joint). The last two ribs (floating ribs) are not connected to the sternum and are also called distal ribs.
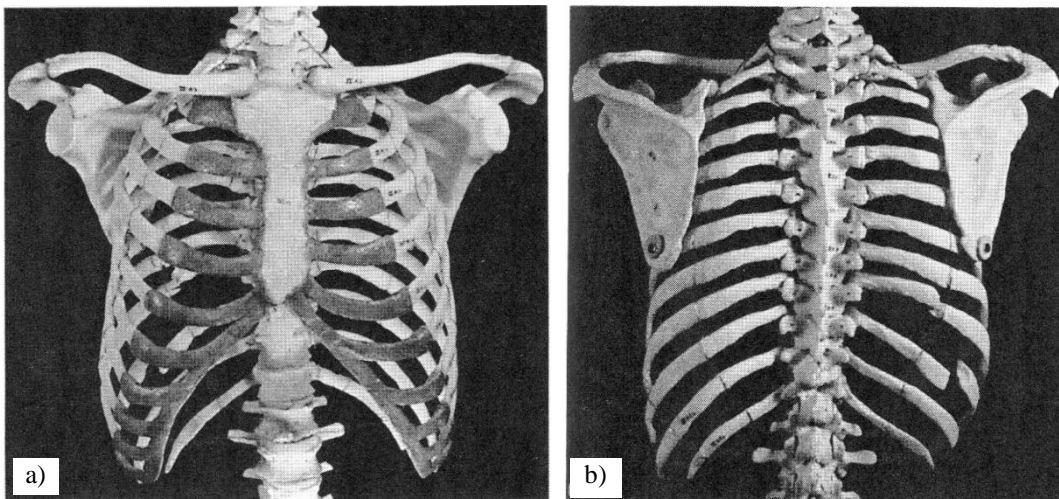
Figure 4.1: (a) Thorax frontal , (b) Dorsal view.

The main function of the costal cartilage is to manage the volume variations of the rib cage during the inhalation and exhalation phases of the air in the lungs. Also, the trunk consists of the spine, the thorax, and the scapular belt. The deformation of the spinal column is the essential element that transmits the deformation induced by the evolution of the pathology to the rest of the skeleton of scoliosis; the spinal column deforms and transmits this deformation to the thoracic cage via the ribs, which largely absorbs this deformation thanks to the elasticity of the fibrous tissue of the costal cartilage. As a general rule, each rib articulates on the spine (Figure 4.1 (b)) (costovertebral joints) with two dorsal vertebrae (Figure 4.2(a)) except for the first rib, which articulates only with the first dorsal vertebra (D1). Apart from this first rib, the anatomy of the ribs (Figure 4.2(b)) is as follows: vertebral end (1) with one vertebral demi facet (9) for the next

vertebra (12), head (2), neck (3), tubercle (4) with one vertebral facet (10) for the current vertebra, angle (5), the body of shaft (6), shaft (7), sternal end (8) with one facet for costal cartilage.
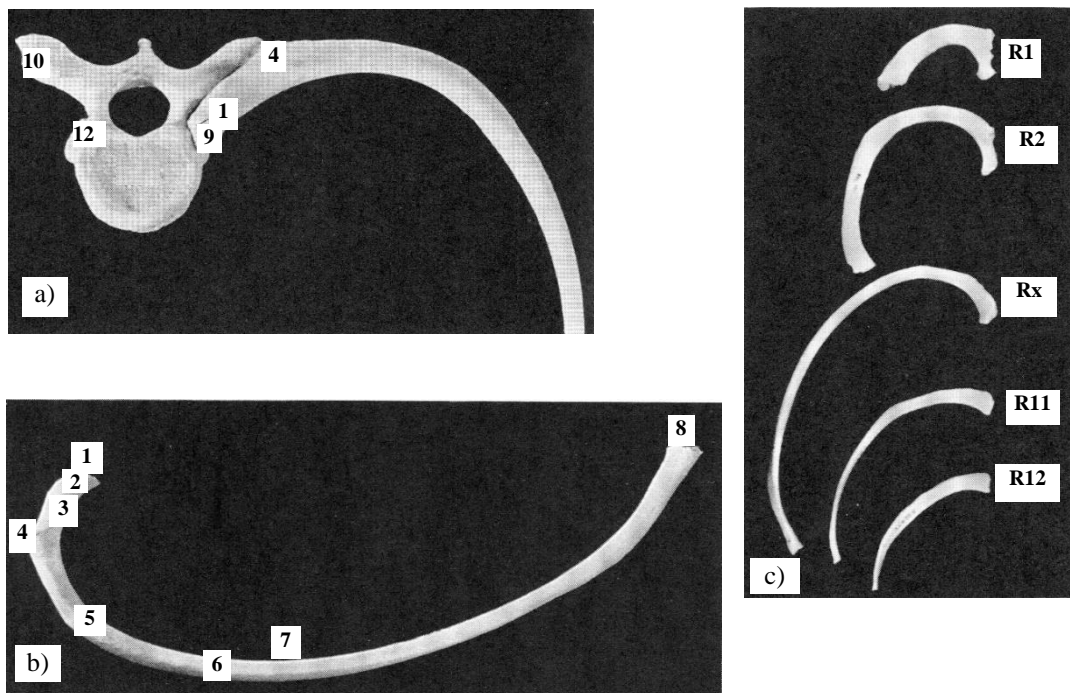
Figure 4.2 (a) Articulation of vertebra and left rib, superior, (b) Right central and superior view of the rib, and (c) Comparative view of ribs.

Depending on their position, the ribs appear to be very different if we compare their shape and method of attachment to the vertebrae and sternum (Figure 4.2(c)). Starting from the rib at the top of the thorax, the first rib (R1) is relatively short, flat, broad, and crescent-shaped, with one joint facet. Another special feature is that it is the only one connected to the clavicle by the costoclavicular joint, hence its robustness. The second rib (R2) shape is an intermediate shape between the first rib and the central ribs (Rx: R3 to R9). This rib is thinner but twice as long as the first rib with a large tuberosity (tubercle) to attach the serratus anterior muscle near the midpoint on the external surface of the shaft.

The R10 rib is a rib that resembles the central ribs with its tuber, angle and costal groove. The difference is that its head has only one proximal joint facet. On the other hand, this rib follows the trend of the central Rx ribs. The length of the neck gradually increases. Finally, it is the rib that has the longest neck. Ribs R11 and R12 have only one facet with a neck, tuberosity, and a hardly noticeable angle. The R12 rib, which is smaller than the R11 rib, loses its costal groove.

Another important element of the rib cage is the sternum located on the midline of the ventral surface of the chest. It is a flat bone with a blade-like contour, likened to a short sword by

many anatomical specialists. It is composed of three atypically shaped bones (Figure 4.3(a)): the manubrium sternal (1), the body (2), the xiphoid process (3). The manubrium (1) is the largest and thickest of the three bones making up the sternum. In the front view, its shape can be likened to an inverted triangle with the lower end truncated by the joint with the body (2). On the upper part, there is a large saddle-shaped articular surface of the clavicular facet (4) and the jugular (suprasternal) notch (5) between the two clavicular facets. Immediately below the clavicular facet is a cavity representing the costal notch 1 (6) to receive the costal cartilage of the first rib R1. The costal notches 2 (7) of the costal cartilage of the second rib R2 are located between the lower part of the manubrium and the upper part of the body.
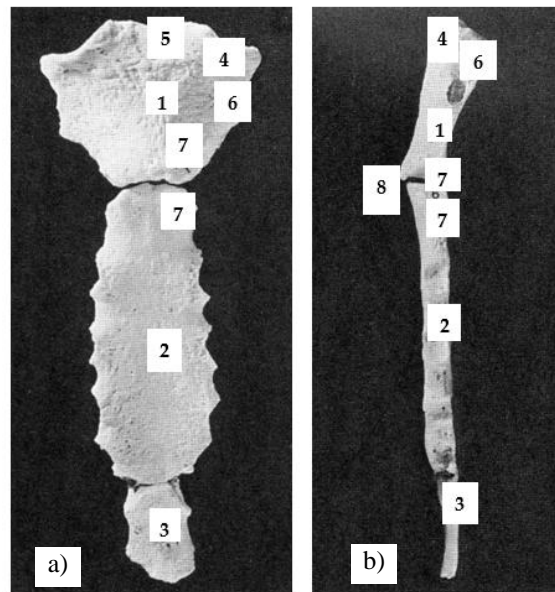
Figure 4.3: (a) Sternum, anterior view, (b) Left lateral view.

The body (2), about twice as long as the manubrium with a generally thinner thickness (Figure 4.3(b)), is divided into four segments. Each segment joint is marked by a costal notch to which the costal cartilage of the five central ribs (R3 to R7) is attached. The lateral border of each segment is concave between coastal notches. The manubrium and body are articulated at an obtuse angle called the sternal angle (8). The xiphoid process (3) is a small, thin bone. It is much thinner than the last lower segment of the body (2). A costal notch on the upper part also serves to reattach the costal cartilage of the R7 rib. The lower end is a surgical landmark to detect the diaphragm, the upper surface of the liver, and the lower border of the heart.

4.1.2   The shoulder girdle

Although the manubrium is a bony part of the sternum, it is one of the three bones that make up the shoulder girdle, i.e., the clavicles, the shoulder blades, and the manubrium. One of the essential functions of the shoulder girdle is to attach the upper limbs to the upper part of the sternum to contribute to the mobility of the arm through the humerus. Thus, the humerus can move in all directions thanks to a fixed point on the scapula, which is considered a pivotal connection. The shoulder girdle also contributes to the orientation of the scapula via the joint between the manubrium and the clavicle (another pivot point). The range of motion of the humerus is then considerably increased.

The clavicle is a long bone with a very significant S-shape that can be touched and followed because it is in contact with the skin and hugs/follows the ventral contour of the chest (Figure 4.4). On each side are the facets of the joints with the sternum (1) and the acromion of the scapula (5). The sternal facet is very broad, massive and is attached to a curved shaft that is approximately circular in cross-section. The acromion facet is situated at the end of the flattened acromial segment. The anatomy of the clavicle (Figure 4.4) can be summarised as follows: sternal facet (1), shaft (2), the acromial portion (3), attachment for the deltoid muscle (4), acromial facet (5), costal tubercle (6), conoid tubercle (7), trapezoid oblique line (8), groove for the subclavius muscle (9).
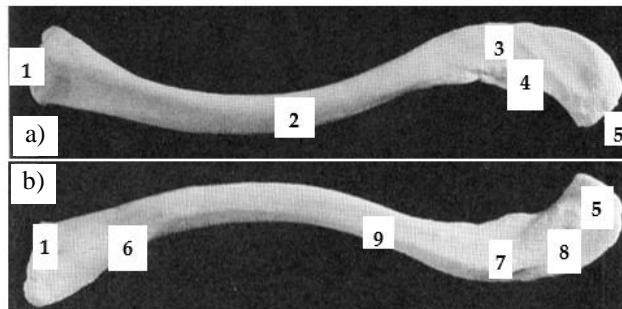
Figure 4.4: (a) Clavicle, left superior view, (b) Left inferior view.

The Scapula can be compared to a large flat triangle at the back of the shoulder between ribs R2 and R7. (Figure 4.5(a)(c)). At the end of the upper side corner (Figure 4.5(a):(1)) of the scapula fits the upper head of the femur into a shallow cavity called the glenoid cavity (Figure 4.5(a):(13), Figure 4.5(b):(1)).

One of the main morphological characteristics of the scapula is its transverse crest which runs along its posterior surface to form the scapula spine. (Figure 4.5(c):(1)). Two cavities called over-spiny and under-spiny pits (Figure 4.5(c):(2), (3)) located on either side of the scapula spine allow the attachment of many muscles. At the widened end of this spine is the acromion (Figure

4.5(b):(2), Figure 4.5(c):(4)) on which the clavicle is articulated. The acromion (Figure 4.5(b):(2)) and the coracoid process (Figure 4.5(b):(3)) have a curved shape to create a vault encompassing the head of the humerus. The purpose of this arch is to limit arm movement.
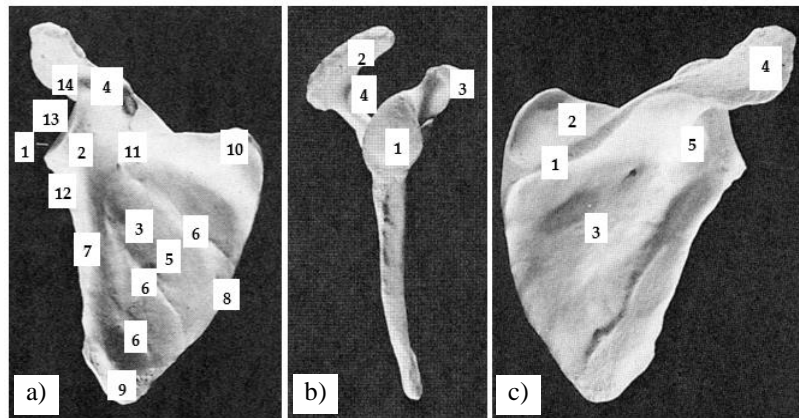
Figure 4.5: (a) Scapula, right ventral view, (b) Right lateral view, (c) Right dorsal view.

In summary, the anatomy of the ventral scapula (Figure 4.5(a)) can be summed up as follows: head (lateral angle) (1), neck (2), body (3), coracoid process (4), subscapular fossa (5), lateral line (6), lateral border (7), vertebral border (8), inferior angle (9), superior angle (10), suprascapular notch (11), infraglenoid tubercle (12), glenoid cavity (13), tubercle for the coracoclavicular ligament (14). Similarly, the anatomy of the dorsal scapula (Figure 4.5 c) can be summed up as follows: spine (1), supraspinous fossa (2), infraspinous fossa (3), acromion process (4), greater scapular notch (5). The anatomy of the lateral scapula (Figure 4.5 b) can be summed up as follows: glenoid cavity (1), acromion process (2), coracoid process (3), greater scapular notch. (4).

4.2   3D adaptive thorax model

4.2.1   Generic model – Ribs model

Despite the few (notorious) differences we detected between the first two ribs R1, R2, the central ribs (R3 to R9 and R10), and the ribs R11, R12, we set up a generic model identical all vertebrae. To take into account the morphological differences of each vertebra, the generic model requires the integration of morphological parameters (Figure 4.6: green dimensions). As this model should also be applied to people of different statures, dimensional parameters are also integrated into the model. The parameter D_n, where n is the number of a vertebra, makes it possible to manage the overall dimension of a rib with the dimension of the vertebra n associated with it, which itself depends on the dimension of the spine. This parameter manages the differences in

stature between each person. The parameter ccx allows managing the relative dimension of a rib with another rib for the same body. The multiplicative coefficients assigned to the ccx parameters make it possible to manage the morphology of the rib in 3D. Thus, in the transverse plane, these coefficients control the dimension of each grey line i.e. the morphology of the orange curve (relative to its projection on the transverse plane). In the vertical planes of each mark affected at the end of these different grey lines, the coefficients ccx control the dimension of each yellow line of the morphology of the orange curve (relative to its projection on the sagittal plane). This orange curve represents the median curve of the coast in its initial state without deformation. The attachment of each rib to the vertebra associated with it (common vertebra) is carried out identically by a cylindrical shape of variable size. We have not considered the attachment to the next vertebra for ribs with two half-facets to avoid making the representation of the model more cumbersome. The hypothesis we have taken is that the 3D evolution of the position of a rib depends mainly on its current rib.
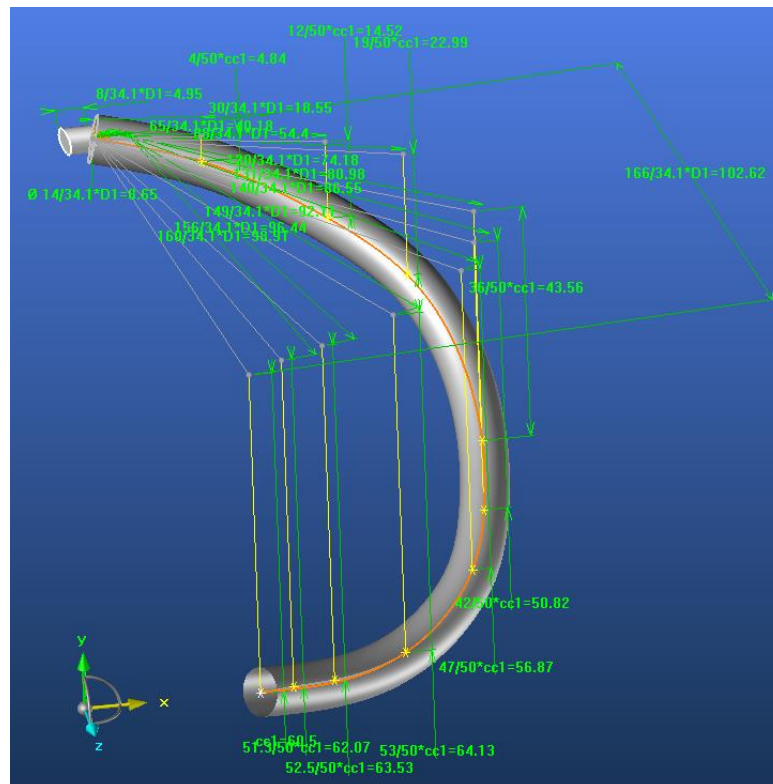
Figure 4.6: Adaptive rib model.

As the vertebrae, ribs, and sternum form a closed cage by the connection of these different bony parts, the dimension of this model is also impacted by the width S_n of the sternum. (Figure 4.7(a)). The distance S_n between two ribs of the same rank n controls the extreme position of each of the ribs of the same rank connected to the sternum.

82

At this stage of modeling, we have not yet taken into account the deformation of the costal cartilage between the ribs and the sternum. For this reason, we decided to integrate it into the continuity of each rib at its extremity (Figure 4.7(b)). To impose a limit of elasticity, *Pe* point is positioned on the orange curve representing the 3D course of the hill before its deformation. A new grey curve faithfully follows this orange curve from point 1 to point *Pe* and ends directly at the end 2 (point hooked to the sternum). This grey curve represents the median curve of the rib with an integrated deformation zone at its end. We then use this other curve to impose a new course of the rib with a future integrated deformation. By this procedure, we ensure that the generic rib model is only deformed in this area, which is similar to the costal cartilage when the spine is deformed.
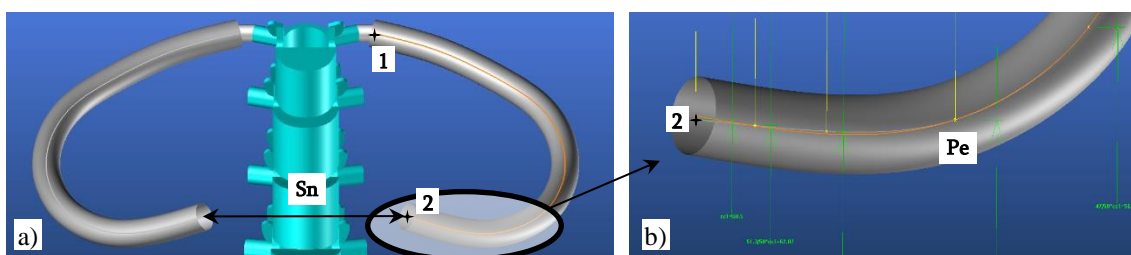
Figure 4.7: (a) Similar ribs manage by sternum width Dx, (b) Elasticity zone of the costal cartilage.

4.2.2   Generic model – Sternum model

The sternum, composed of three distinct parts, was modelled in two parts: the manubrium sternal, the body + the xiphoid process. As the thickness between the body and the xiphoid process is relatively close, we have merged these two bony parts into a single part (Figure 4.8(a)(b)). Moreover, their alignment can only justify this merger (Figure 4.8(b)). On the other hand, fusion was impossible with the manubrium since the manubrium and the body are articulated with the sternal angle. Besides, the thickness of the manubrium is greater. However, we did not take this difference in thickness into account as it does not influence our final application.

The model developed is an adaptive model that must be parameterised according to the stature of each person. The R1 rib being the main rib attached to the manubrium, it allows to position in 3D not only the manubrium but also the sternum. The first dorsal vertebra being the vertebra of attachment of the R1 rib and parametrized by D1, we decided to manage the global dimension of the sternum by the same parameter D1 (Figure 4.8(c)(d)), as we did with the R1 rib.
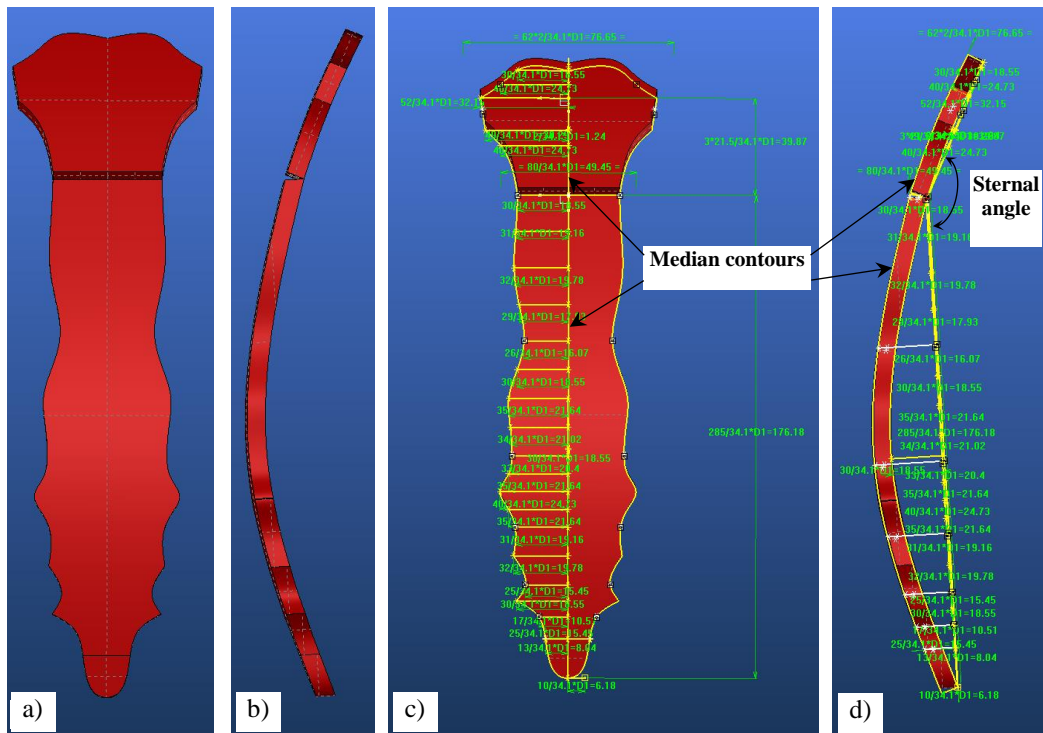
Figure 4.8: (a)(c) Adaptive sternum, anterior view, (b)(d) Left lateral view.

Following the same principle as the different ribs, the multiplicative coefficients assigned to the different dimensions parameterised by D1 make it possible to manage the morphology of the sternum in 3D employing the yellow contours (Figure 4.8(c)). These contours are defined in two planes to respect the sternal angle (Figure 4.8(d)). Certain sternum with a slight curvature in the sagittal plane, two curved yellow median contours (Figure 4.8(c)(d)) have therefore been integrated into the manubrium and body models to take into account this 3D morphological specificity.

4.2.3   Generic model – Clavicle model

The clavicle model follows a modeling strategy close to that of the coasts from the morphological point of view and to that of the sternum on the dimensional aspect. It is an adaptive model which must also be parameterized according to the stature of each person. For the same reasons defined above for the sternum, we manage the global dimension of the clavicle by the parameter D1 (Figure 4.9(b)). The multiplicative coefficients assigned to the different dimensions parameterised by D1 make it possible to manage the morphology of the clavicle in 3D (Figure 4.9(a)). Thus, in the transverse plane, these coefficients control the dimension of each grey line, the morphology of the white curve. In the vertical planes of each mark assigned at the end of these different grey lines, the coefficients *ccx* control the dimension of each yellow line, the morphology

of the white curve in other planes. This white curve represents the median curve of the clavicle. An adapted parametrization of these two types of lines makes it possible to respect the very significant S-shape of the clavicle. It will be adjusted to the correct dimensions when the model is placed inside the body surface obtained by the body scanner because the clavicle is in contact with the skin and follows the ventral contour of the chest. The connection to the manibrium is made by a marker placed on the base surface of the model (articular facet) at the end and perpendicular to the white median line of the clavicle.
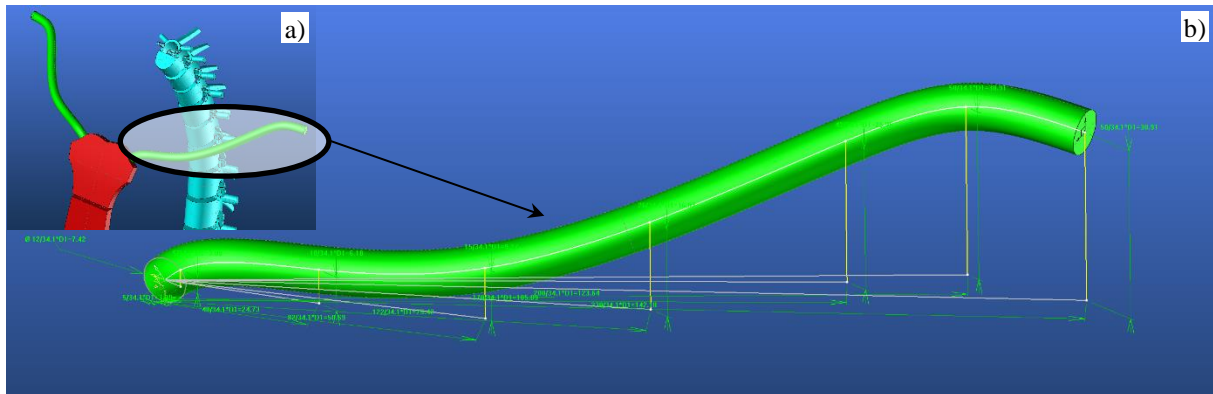
Figure 4.9: Adaptive clavicule model.

4.2.4   Generic model – Scapula model

It is a complex model composed of 3 sub-models to describe the three bone parts, namely supraspinous & infraspinous fossa (1), spine with acromion process (2), coracoid process (3), as shown in Figure 4.11. The scapula modeling process starts with the design of the two upper and lower triangles whose characteristic shape is defined by the three edges (upper, medial, lateral) managed by the three associated angles (upper, medial, lateral).
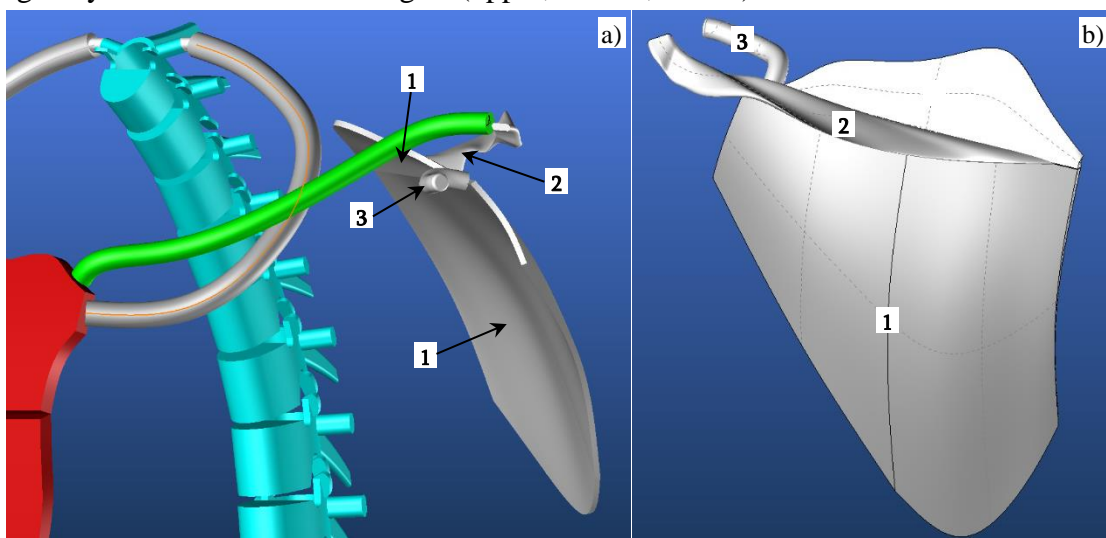
Figure 4.10: (a) The rib R1, sternum, clavicle, scapula, vertebra, (b) Scapula.

Figure 4.12 presents an improved version of the outer shape of the supraspinous and infraspinous fossa defined by two orange contours (1) relative to the upper and lower parts. A pivot axis (2: yellow line) joins them and manages the angle between these two entities to obtain a global shape of the model which follows the morphology of the ribs, the convexity of the thorax.
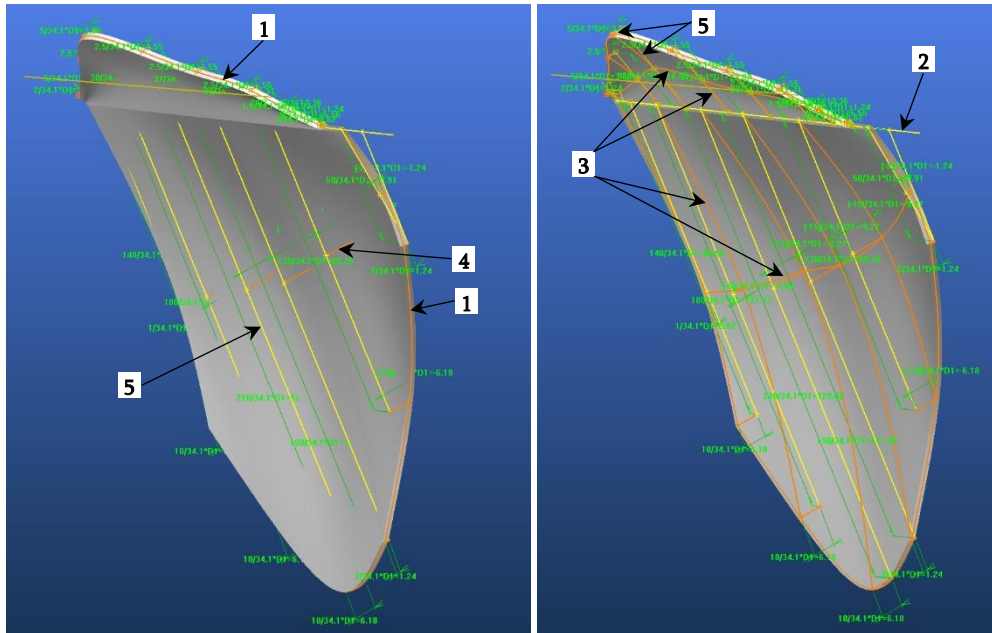
Figure 4.11: The two views of the scapula with the supraspinous and infraspinous fossa.

Eacentity is defined by a network of curves in two main directions attached to the different contours to distinctly manage the supraspinous and infraspinous fossa. Each network is composed of orange lines (3) to describe the double curvature of the shape, some of which manage the depth of the concavity of the pit (4). These orange lines (3) are connected to yellow lines (5) which manage the dimension of the contours parameterized by D1. The multiplicative coefficients assigned to the different dimensions parameterized by D1 make it possible to manage the morphology of the contours and therefore the morphology of the main parts of the scapula.

The anatomy of the spine with acromion process is a more complex 3D shape (Figure 4.12) which starts on the pivot line of the supraspinous and infraspinous fossas with a wide and shallow base surface (1) and ends with another slightly thicker and narrower base surface (2) specific to the acromion process. The morphology of the edges of this 3D shape, impacted by this starting and ending conditions, requires the ends of the base surfaces to follow two 3D curves ((3): purple and orange curves). The purple and orange curves are connected respectively to a set of purple (4) and white (5) lines. Some (4) manage the global dimension of the 3D shape by the parameter D1, and others (5) manage the 3D wavy morphology. As previously, the morphology

86

of this bone part is managed by the multiplicative coefficients assigned to the different dimensions parameterized by D1.
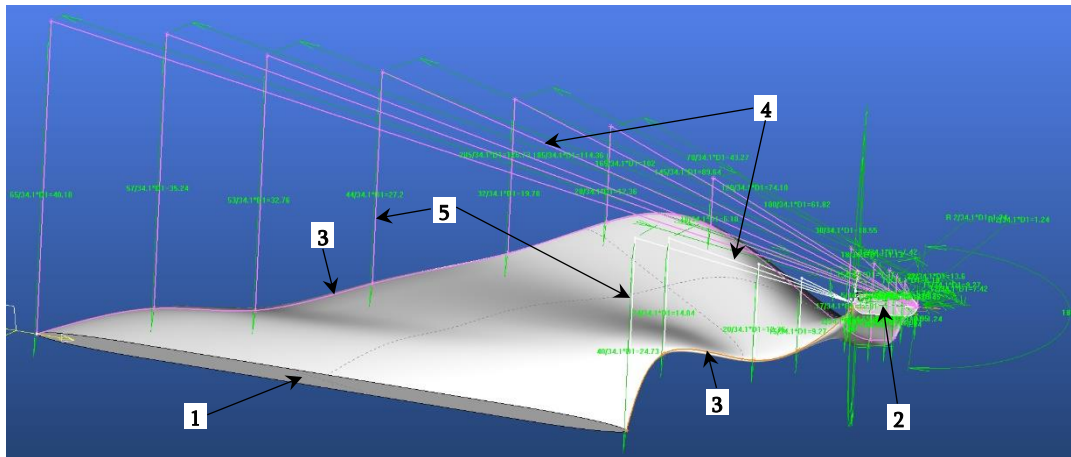
Figure 4.12: The Scapula spine with acromion process.

To obtain the curved shape of the Coracoid process (Figure 4.13), a model uses main ribs, i.e., two types of purple lines which manage the dimension and then the morphology of the median curve of the 3D shape of the model. It is by D1 that the global dimension of the shape is managed, by the multiplicative coefficients of D1 that the 3D morphology of this element is managed.
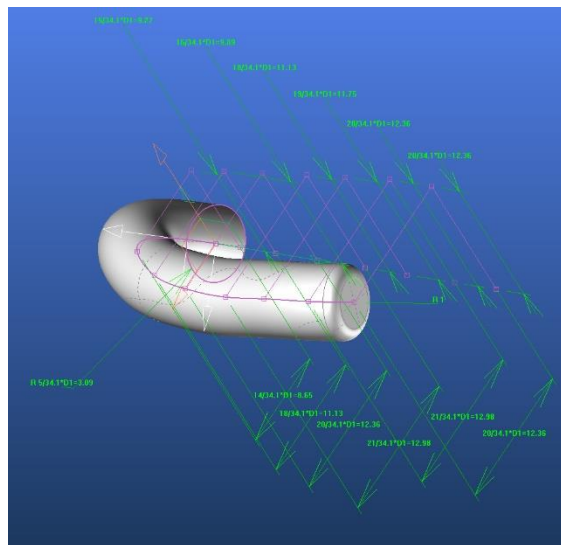
Figure 4.13: The Caracoid process.

4.3 3D modelling of thorax without any scoliosis-related deformity

The models we have created do not pretend to represent exactly the morphology of the thorax, but they aim to be dimensionally, proportionally, and functionally close to it. Figure 4.14 shows the developed thorax model under different views in standard spine condition, without any scoliosis-related deformities.
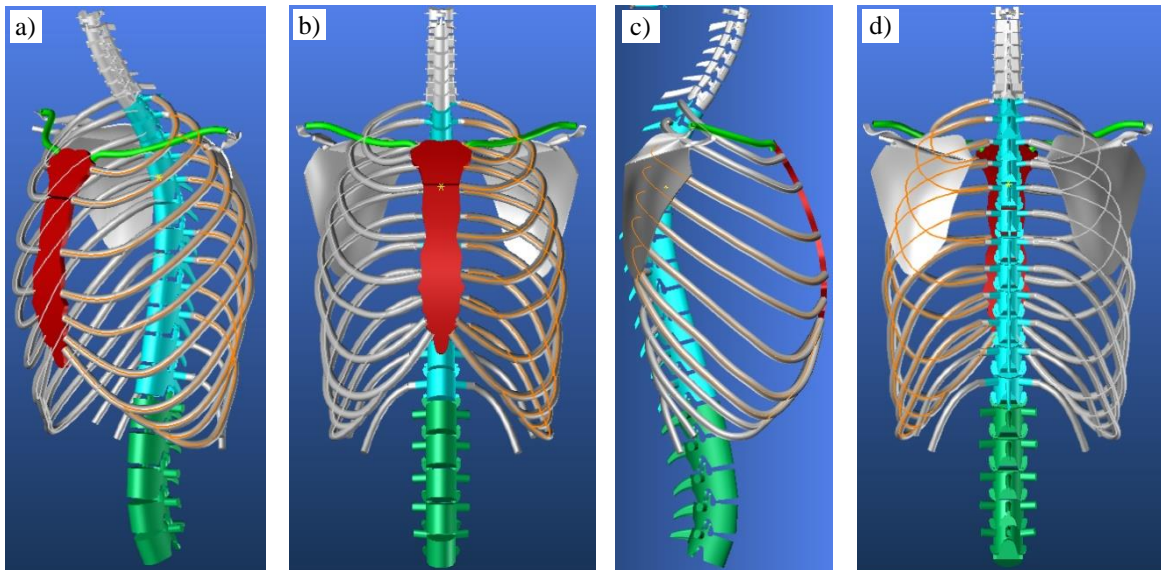
Figure 4.14: (a)Trunk model, 3D view, (b) front view, (c) back view, (d) right lateral view.

This trunk model is controlled by the spine. In our previous results, the total length L_t of the spine is the only parameter to give the model for parameterizing the length l_{tn} of each vertebra/disk Table 4.1 . In this notation, t represents the type of vertebra (C: cervical, D: dorsal, L: lumbar) and the number of the vertebra in its category. Each vertebra was dimensioned by the parameter D_x (x: number of vertebrae out of category). Since the dimension of each bony part of the thorax was managed by this common parameter D_x, the complete model of the thorax could then evolve in all three dimensions (3D) with each modification of the spine. To obtain the value of the spinal column parameters, an analysis of the images, in the frontal and coronal plane, of the patient's spinal column X-rays is necessary.

Our first result was to test the limits of our model by imposing a perfect vertical rectilinear alignment of the spine. This case is a textbook case which is not found, hence a rather improbable thorax deformation. Under these conditions, we were able to verify the flexibility of our model's adaptation to change its stature, the length of the spinal column. The passage of a spinal column length of L_t=650mm to L_t=750mm imposes length (l_{tn}) values of each vertebra/disk doneness in the Table 1: H650, H750. The test was carried out without any rotation in the 3 characteristic planes of the human being (Figure 4.15). The images were taken under identical image capture conditions. The results show a consistent increase in the length and volume of each bony part (spine and thorax).

Table 4.1: Values of L_{tn} for the different values of L_t, Values of the deformation angles.

Segment	H_{750}	H_{650}	Sagittal	H_{650}	Coronal	H_{650}	Transverse	H_{650}
l_{C1}	18	15.6	α_{C1}	10	β_{C1}	-26	γ_{C1}	15
l_{C2}	18.75	16.25	α_{C2}	15	β_{C2}	-23	γ_{C2}	12
l_{C3}	19.5	16.9	α_{C3}	20	β_{C3}	-20	γ_{C3}	9
l_{C4}	20.25	17.55	α_{C4}	25	β_{C4}	-17	γ_{C4}	6
l_{C5}	20.25	17.55	α_{C5}	28	β_{C5}	-14	γ_{C5}	3
l_{C6}	19.5	16.9	α_{C6}	30	β_{C6}	-11	γ_{C6}	0
l_{C7}	23.25	20.15	α_{C7}	36	β_{C7}	-8	γ_{C7}	-3
l_{D1}	25.5	22.1	α_{D1}	33	β_{D1}	-6	γ_{D1}	-6
l_{D2}	27.75	24.05	α_{D2}	27	β_{D2}	-3	γ_{D2}	-9
l_{D3}	27.75	24.05	α_{D3}	17	β_{D3}	0	γ_{D3}	-12
l_{D4}	29.25	25.35	α_{D4}	14	β_{D4}	3	γ_{D4}	-15
l_{D5}	29.25	25.35	α_{D5}	8	β_{D5}	6	γ_{D5}	-18
l_{D6}	31.5	27.3	α_{D6}	1	β_{D6}	9	γ_{D6}	-21
l_{D7}	32.25	27.95	α_{D7}	-10	β_{D7}	12	γ_{D7}	-24
l_{D8}	33.75	29.25	α_{D8}	-13	β_{D8}	15	γ_{D8}	-27
l_{D9}	34.5	29.9	α_{D9}	-14	β_{D9}	18	γ_{D9}	-24
l_{D10}	36	31.2	α_{D10}	-15	β_{D10}	21	γ_{D10}	-21
l_{D11}	38.25	33.15	α_{D11}	-16	β_{D11}	18	γ_{D11}	-18
l_{D12}	40.5	35.1	α_{D12}	-18	β_{D12}	15	γ_{D12}	-15
l_{L1}	42.75	37.05	α_{L1}	-15	β_{L1}	12	γ_{L1}	-12
l_{L2}	43.5	37.7	α_{L2}	-11	β_{L2}	9	γ_{L2}	-9
l_{L3}	42.75	37.05	α_{L3}	-8	β_{L3}	6	γ_{L3}	-6
l_{L4}	42.75	37.05	α_{L4}	4	β_{L4}	3	γ_{L4}	-3
l_{L5}	41.25	35.75	α_{L5}	20	β_{L5}	0	γ_{L5}	0

Figure 4.15 : Evolution of the thorax model for a variation in spine length from L_t =650mm to a length L_t =750mm.

89

The other three tests were to show separately the deformation of the spinal column in the three characteristic planes: sagittal, coronal and transverse. These deformations were carried out with the same length of spinal column. L_t=650 mm. Figure 4.16 presents the three deformations carried out independently from the angular data in Table 1. The first result is used as a reference to compare each of the deformations. Each image was taken in the deformation plane concerned to better appreciate the phenomenon.
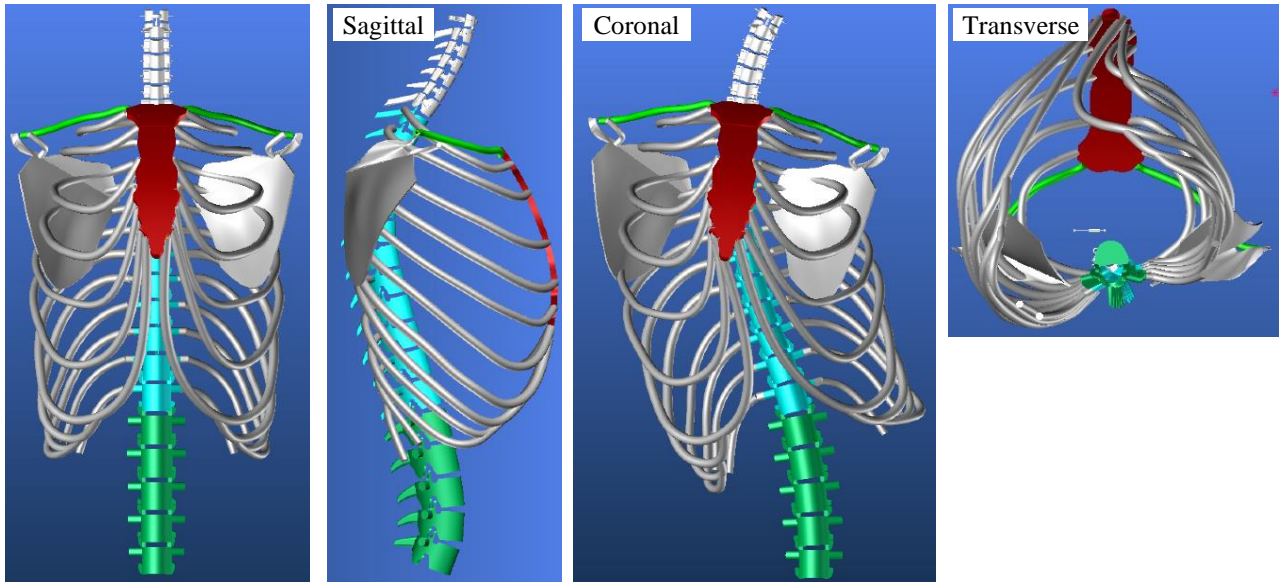
Figure 4.16 : Evolution of the thorax model in sagittal, coronal, transverse planes.

Figure 4.17 presents the same results in an identical 3D view. An analysis of these initial results shows the need to know each of the initial parameters of the spine in order to have a realistic representation of the whole thorax/spine. Taken independently, the rotations lead to unreal thorax deformation.

The results show that the scapulae are well located between the ribs R2 and R7, they also show the need to control them by adapting their position according to the deformity. Under certain conditions, one or both scapulae may pass through the ribs. We must therefore manage the relative position of the scapulae in relation to the proximal ribs, as some muscles such as: trapezius, deltoid, infraspinous, teres major, serratus anterior, levator scapula, rhomboid minor, rhomboid major.
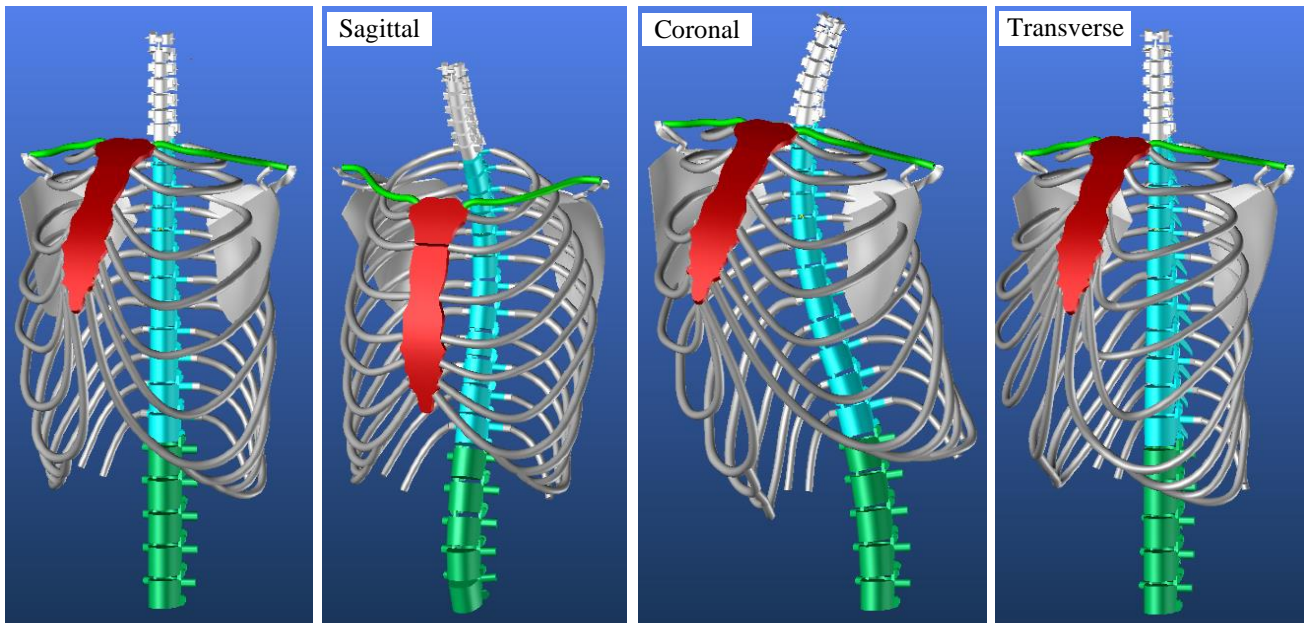
Figure 4.17: Evolution of the thorax model in sagittal, coronal, transverse planes with the same point of 3D view.

4.4 Scapulae anti-penetration management model

Two angles *Angle$_{rc}$* each associated with a marker centred on a pivot point *Pc* makes it possible to manage the two rotations of each scapula which contribute to the phenomenon of penetration of the scapula into the nearby ribs (Figure 4.18). In this notation, *r* represents the type of rotation (*1:axis1*, *2:axis2*), c represents the scapula (*G:left*, *D:right*). To avoid the penetration of a scapula, we must check the distance between two points C_1, C_2 defined on the ribs R4 and R7 in relation to their respective projection O_1, O_2 on the inner face of the scapula.
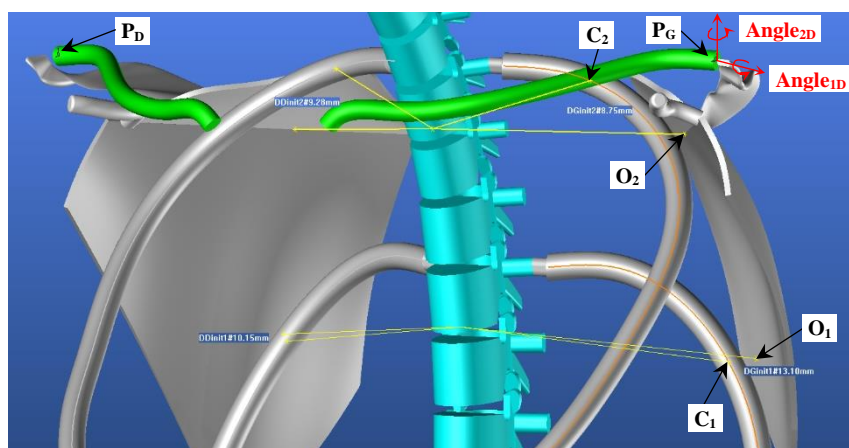
Figure 4.18: Scapula orientation mark and control points.

In the evolution of the spine, the *D$_C$init$_x$* distances of the points between those of the ribs and those of the scapulae, *x* representing the index relative to the measurement points of the

distances between the ribs and the scapulae (Figure 4.18), must be preserved as well as possible after deformation. The rotation that has the greatest impact on the phenomenon of penetration of the scapulae into the ribs is γ_{Cn} in the transverse plane Table 4.1. To estimate the value of the *Angle$_{rc}$* angles that avoid penetration, a series of tests were carried out with different values of rotation such that the gaps between each dorsal vertebra are constant

Table **4.2**.

Transverse	$\delta=-2°$	$\delta=-1,5°$	$\delta=-1°$	$\delta=-0,5°$	$\delta=0°$	$\delta=0,5°$	$\delta=1°$	$\delta=1,5°$	$\delta=2°$
$\gamma D1$	-24	-18	-12	-6	0	6	12	18	24
$\gamma D2$	-22	-16.5	-11	-5.5	0	5.5	11	16.5	22
$\gamma D4$	-18	-13.5	-9	-4.5	0	4.5	9	13.5	18
$\gamma D5$	-16	-12	-8	-4	0	4	8	12	16
$\gamma D6$	-14	-10.5	-7	-3.5	0	3.5	7	10.5	14
$\gamma D7$	-12	-9	-6	-3	0	3	6	9	12
$\gamma D8$	-10	-7.5	-5	-2.5	0	2.5	5	7.5	10
$\gamma D9$	-8	-6	-4	-2	0	2	4	6	8
$\gamma D10$	-6	-4.5	-3	-1.5	0	1.5	3	4.5	6
$\gamma D11$	-4	-3	-2	-1	0	1	2	3	4
$\gamma D12$	-2	-1.5	-1	-0.5	0	0.5	1	1.5	2

Rotations of vertebra for different gaps δ.
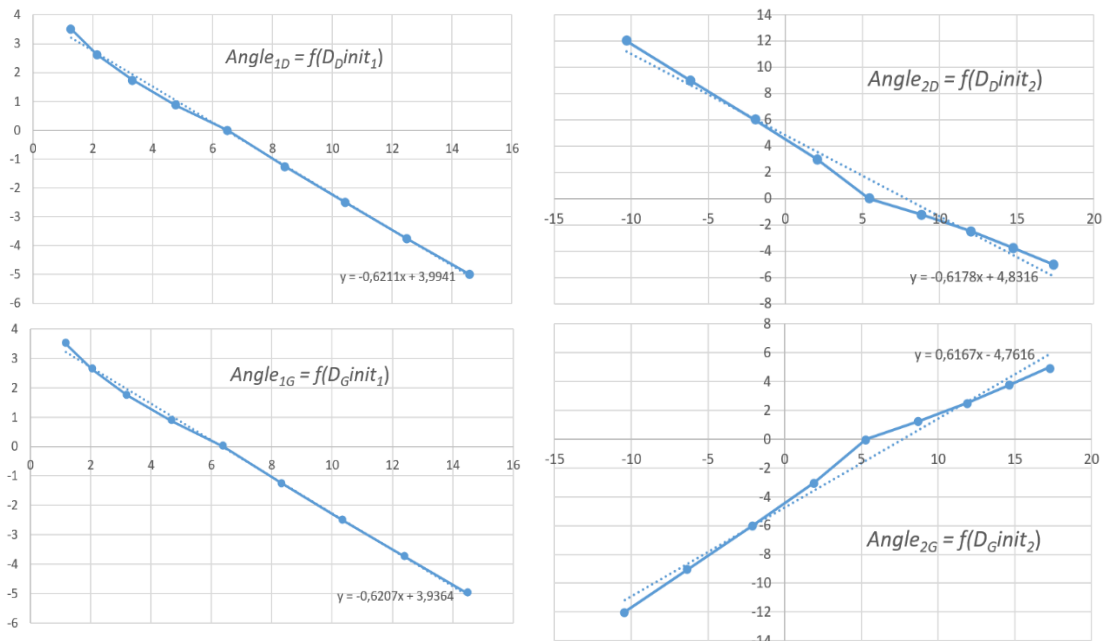
Figure 4.19: Evolution curves of *Angle$_{1D}$* , *Angle$_{2D}$* , *Angle$_{1G}$* , *Angle$_{2G}$* in function of *D$_D$init$_1$* , *D$_D$init$_2$* , *D$_G$init$_1$* , *D$_G$init$_2$* .

Figure 4.19 represents the evolution curves of the different *Angle$_{rc}$* angles as a function of the corrections to be made to the *D$_C$init$_x$* distances.

Table 4.3: Angular adjustment of the scapula according to the rotations imposed on the vertebrae. shows the value of the $Angle_{rc}$ angles to be imposed on the rotations of the scapulae to adjust their position relative to the ribs according to the distance δ imposed on the dorsal vertebrae in the transverse plane. The D_{Cinit_x} values are those obtained after each deformation. The $Angle_{rc}$ values are those to be imposed on the different rotations of the scapulae to get closer to the initial D_{Cinit_x} values for $\delta=0°$ in red

Table 4.3: Angular adjustment of the scapula according to the rotations imposed on the vertebrae.

$\delta°$	D_{Dinit_1}	$Angle_{1D}$	D_{Dinit_2}	$Angle_{2D}$	D_{Ginit_2}	$Angle_{1G}$	D_{Ginit_2}	$Angle_{2G}$
2	14.58	-5	17.39	-5	1.18	3.5	-10.41	-12
1.5	12.49	-3.75	14.77	-3.75	2.05	2.625	-6.29	-9
1	10.43	-2.5	12.04	-2.5	3.22	1.75	-2.1	-6
0.5	8.42	-1.25	8.83	-1.25	4.68	0.875	1.93	-3
0	6.5	0	5.42	0	6.41	0	5.31	0
−0.5	4.77	0.875	2.05	3	8.33	-1.25	8.72	1.25
−1	3.31	1.75	-1.98	6	10.34	-2.5	11.95	2.5
1.5	2.14	2.625	-6.17	9	12.41	-3.75	14.69	3.75
2	1.27	3.5	-10.29	12	14.5	-5	17.31	5

Figure 4.20 shows an example of correction of the position of the scapulae during a rotation of the spine with a rotation $\delta=1.5°$ between each vertebra. The Figure 4.20(a) shows the
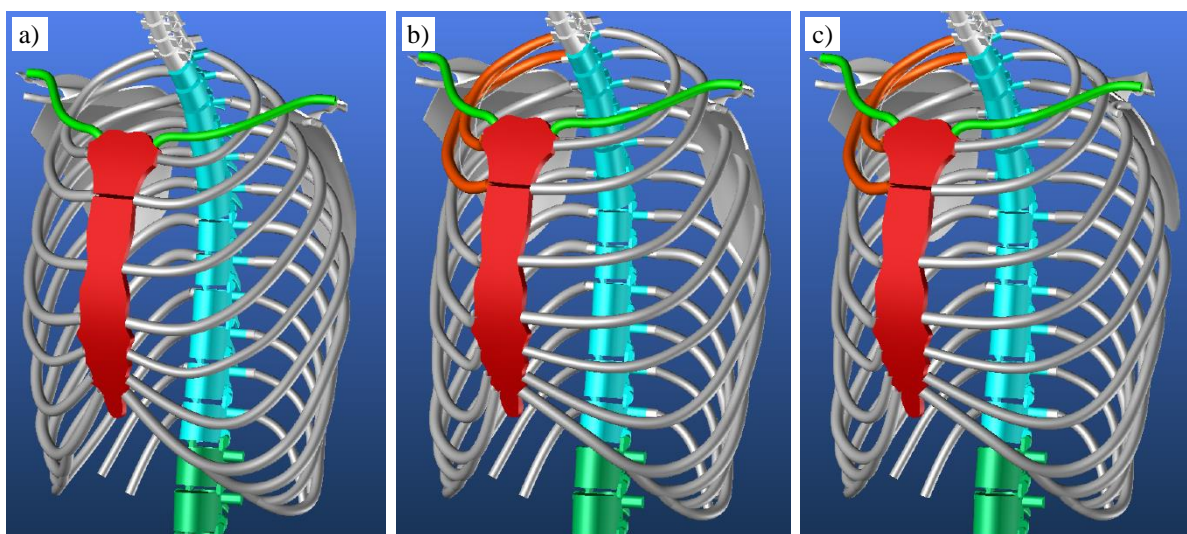
Figure 4.20: (a) Initial spine position, (b) Spine evolution of δ=1.5° without correction, (c) Spine evolution of δ=1.5° after correction.

initial state of our thorax model for $\delta=0°$ with an evolution of the vertebrae in the sagittal plane identical to Table 4.1 (sagittal, H_{650}).

The Figure 4.20(b) shows the thorax model for $\delta=1.5°$. We can clearly see that the left scapula penetrates the ribs while the right scapula moves away from the ribs. Figure 4.20(c) shows that the left scapula has returned to a position close to the initial state after correction of the $Angle_{rc}$ angles.

4.5 3D modelling of thorax withscoliosis-related deformitie

It is from the coronal and sagittal images from the EOS medical scanner that we have extracted the measurements relating to the patient's skeleton in order to reconstruct it digitally with our adaptive thorax model. Figure 4.21(a) presents the measurements of each vertebra taken in the sagittal plane. Figure 4.21(b)(c)(d) shows the measurements of the cervical, dorsal, and lumbar vertebrae respectively in the coronal plane.
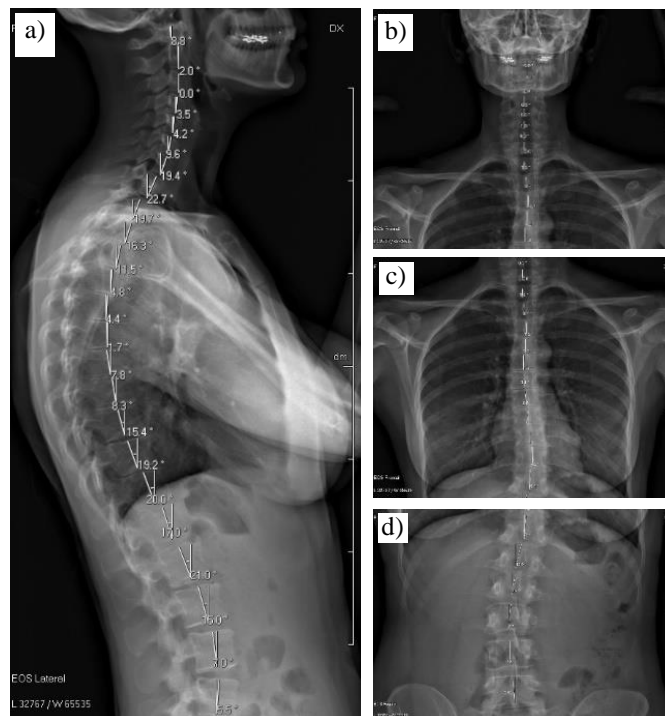
Figure 4.21: EOS medical images, (a) manual Sagittal angles, (b)(c)(d) automatic Coronal angles.

Table 4 summarises all the measures l_{tn}, α_{tn}, β_{tn}, γ_{tn}, obtained from EOS medical images.

Segment		Sagittal		Coronal		Transverse	
l_{C1}	18.1	α_{C1}	-8.8	β_{C1}	0	γ_{C1}	0
l_{C2}	22.7	α_{C2}	-2	β_{C2}	1.1	γ_{C2}	0
l_{C3}	18.1	α_{C3}	0	β_{C3}	0	γ_{C3}	0
l_{C4}	17.8	α_{C4}	3.5	β_{C4}	0.0	γ_{C4}	0
l_{C5}	17.1	α_{C5}	4.2	β_{C5}	-1	γ_{C5}	0
l_{C6}	17.4	α_{C6}	9.6	β_{C6}	1.3	γ_{C6}	0
l_{C7}	19.7	α_{C7}	19.4	β_{C7}	0	γ_{C7}	0
l_{D1}	23.8	α_{D1}	22.7	β_{D1}	0	γ_{D1}	0
l_{D2}	24	α_{D2}	29.7	β_{D2}	-1.2	γ_{D2}	0
l_{D3}	22	α_{D3}	16.3	β_{D3}	-3.7	γ_{D3}	0
l_{D4}	23.1	α_{D4}	11.5	β_{D4}	-1.6	γ_{D4}	0
l_{D5}	23.2	α_{D5}	4.8	β_{D5}	0	γ_{D5}	0
l_{D6}	25.5	α_{D6}	4.4	β_{D6}	1.8	γ_{D6}	0
l_{D7}	26.7	α_{D7}	-1.7	β_{D7}	-3	γ_{D7}	0
l_{D8}	25.8	α_{D8}	-7.8	β_{D8}	-6.7	γ_{D8}	0
l_{D9}	29.1	α_{D9}	-8.3	β_{D9}	-5.7	γ_{D9}	0
l_{D10}	27.2	α_{D10}	-15.4	β_{D10}	-3.7	γ_{D10}	0
l_{D11}	32.7	α_{D11}	-19.2	β_{D11}	-2.5	γ_{D11}	0
l_{D12}	36.1	α_{D12}	-20	β_{D12}	5.4	γ_{D12}	0
l_{L1}	35.9	α_{L1}	-17	β_{L1}	13	γ_{L1}	0
l_{L2}	37.1	α_{L2}	-21	β_{L2}	9.3	γ_{L2}	0
l_{L3}	38.7	α_{L3}	-15	β_{L3}	5.8	γ_{L3}	0
l_{L4}	38.9	α_{L4}	-7	β_{L4}	-1.2	γ_{L4}	0
l_{L5}	39.5	α_{L5}	5.5	β_{L5}	-3.5	γ_{L5}	0

These data were imported into our thorax model.

Table 4.4: Summarizes all the measures l_{tn}, δ_{tn}, δ_{tn}, δ_{tn}.

Figure 4.22 shows the integration of the thorax model into the scanned body of a patient with mild scoliosis. Figure 4.22(a) shows that the overall volume of the model is well adjusted to the volume of the person. The spine follows the midline of the back perfectly. The sternum is very close to the front of the patient and follows the front midline correctly. Figure 4.22(b) shows that the orientation of the spine in the coronal plane is consistent with the course of the Figure 4.21(b)(c)(d). The dorsal ribs point to the right as they follow the orientation of the spine. They appear to be slightly offset from the contour of the scanned body. This can be explained by the fact that the patient did not take the same position when scanned by the body scanner and the EOS scanner. Each of the devices requires a specific position to be taken, which we can correct by

detecting the exit of the model outside of the scanned body envelope. Figure 4.22(c) is a representation of our 3D thorax model for this patient which we will later use to define the position
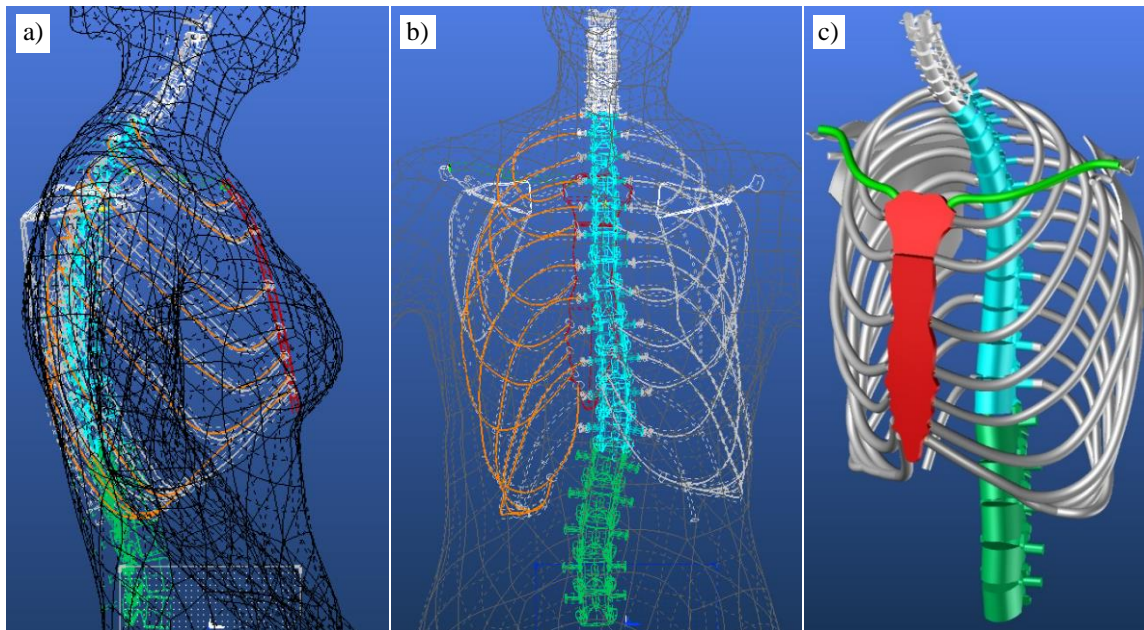
Figure 4.22: The Thorax model parametrized by measured data inside patient scanned body.

of the anthropometric points and morhological curves necessary for the design of his basic evolutionary pattern.

4.6   Conclusion

The current study presents a method for building a fully parametric 3D adaptive model of the upper part of the human skeleton. The parameters make it possible to dimension the skeleton of the thorax and to adapt the morphology of the different bones that make it up. The interest of this operation is to be able to adapt it to the global morphology of a patient suffering from more or less strong scoliosis.

This model is designed from the spine and follows the deformation of the spine. The interest of this concept is to adapt the thorax skeleton according to the temporal evolution of the spinal column deformation.

An EOS scan of the patient is carried out regularly for his medical follow-up, hence this strategic departure of analysis and processing of his scanned images to control the global model of a patient over time

The integration of the 3D thorax model adjusted to the patient's data in his 3D body scan enables the chain of acquisition, processing and global model to be validated. It is always possible to improve the fit of the model from a morphological point of view for the different bones at the start of the integration. Afterwards, it will only be necessary to modify the angles of the spine to see the evolution of the disease.

At this stage of the study, we have the possibility of detecting the anthropometric points on certain bony parts of the skeleton and of locating the morphological curves in relation to certain bones. These data represent the starting point of our 3D garment model which is the subject of the next chapter.

CHAPTER 5 : 3D ADAPTIVE GARMENT MODEL

This chapter is devoted to the implementation of a new process for designing body-hugging clothing in a digital 3D environment. It is intended for people with physical disabilities such as scoliosis. It can be considered as a draping techniques derivative heavily used by designers of fashion houses who create directly on mannequin or human body.

The specificity of this process is that it must be directly connected to the skeleton and the body scan of the person. This makes it possible to follow the patient's morphology and to take into account his atypical shape.

To create a garment, we need the people's measurements. The human skeleton is a means of knowing the measurements of the people which falls under the anthropometry of the human body. It is therefore from the anthropometric points that we can identify the measurement or control points of the garment. The body scan provides a 3D representation of the outer envelope of the body. The latter makes it possible to measure the morphological contours located by the anthropometric points. This strong connection between the skeleton and the people's body scan is therefore essential so that the garment automatically adapts to the evolution of the patient's pathology over time. Scoliosis being a deformation of the spine causing a disorder on the thoracic cage, it seems natural to control the garment by the skeleton of the trunk.

An analysis of the 2D creation process of the women's block pattern shows that this creation process mainly depends on specific anthropometric points and certain morphological curves of the trunk. One of the strategic steps will be to identify the similarities between the 2d and 3D creation process of the women's block pattern.

Among other things, when setting up the 3D creation process, we must take into account the 3D ease allowance that we perceive in the 2D creation process by adding the 2D ease allowance of the garment on the value of the morphological contours. In the case of the 3D process, this value will necessarily be defined in 3D. A 3D ease allowance model will serve as the physical interface between the 3D trunk model and the 3D garment model.

5.1 Analysis of the 2D creation process of the women's block pattern

5.1.1 2D process analysis

Different methods of flat cutting can obtain the women's block pattern. Depending on the country or the author who developed the method, the method can be very different. In the same country, we can find different methods depending on the fashion school and the teachers. Despite this diversity of design techniques depending on the perception of pattern during the transition from 3D to 2D it is flattening. The results remain relatively close because they all follow a common strategy: draping a canvas over the women's body as close as possible to it. These methods generally start with a base rectangle whose horizontal direction represents the largest morphological contour of the body and whose vertical direction represents its greatest height (Figure 1: ½ chest girth +10, full front length). This rectangle is often reduced to two perpendicular lines representative of one of the rectangle corners, having the same objective of framing the patterns according to the people's measurements.
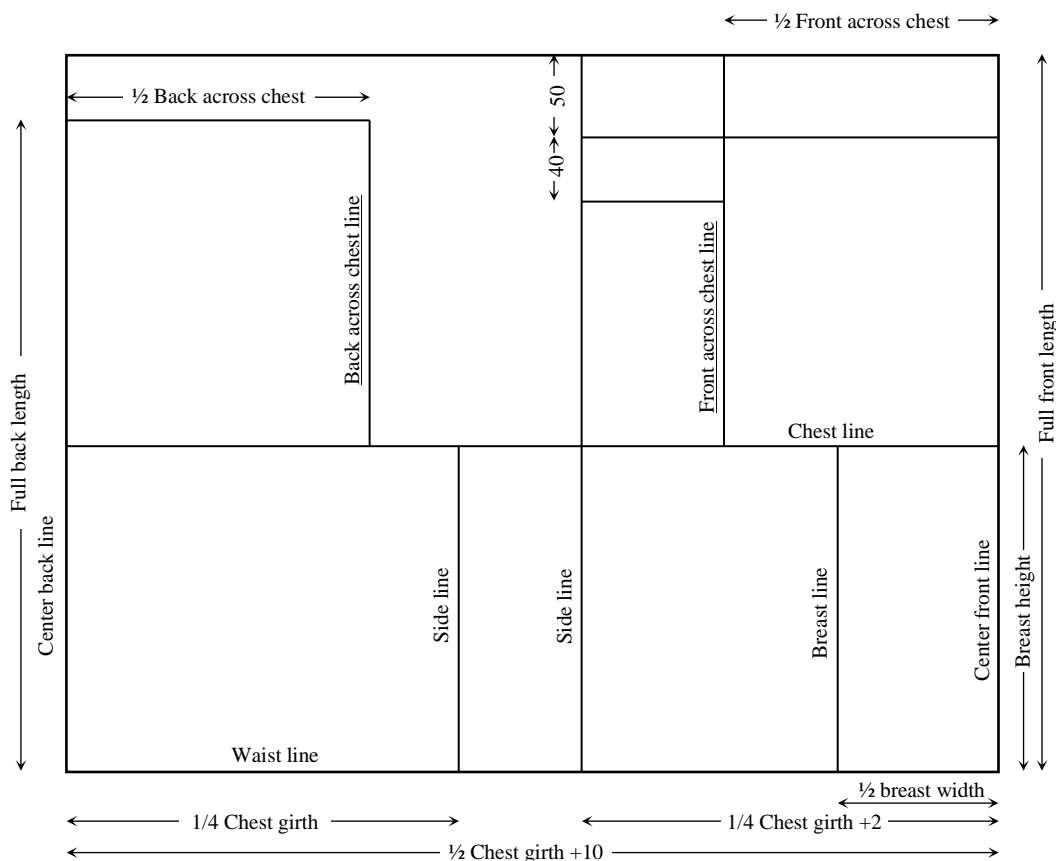
Figure 5.1: Morphological lines creation.

Then, different lines parallel to the bottom horizontal line of the rectangle (Figure 1: waistline) are created. They make it possible to position the different morphological contours concerning each other in the vertical direction (Figure 5.1: chest, breast height, full back length, shoulder slopes by the values 50-40). A similar operation is performed in the vertical direction for the rectangle's right and left vertical lines (Figure 5.1: center front and back lines) to define the other morphological lines (Figure 1: back across the chest, front across the chest, breast, side). This step separates the front and the back.

Morphological contours are not sufficient to create pattern. The human skeleton tells us about the anthropometry of the body and its morphology. Some anthropometric points such as the acromion, the 7th cervical, the manubrium, the front across the chest, the back across the chest, the underarm, the neck side (Figure 5.2: star points) represent spatial landmarks to create other lines or complementary curves (Figure 5.2: shoulder lines, neckline) and set the limits necessary for the outline of the block pattern.
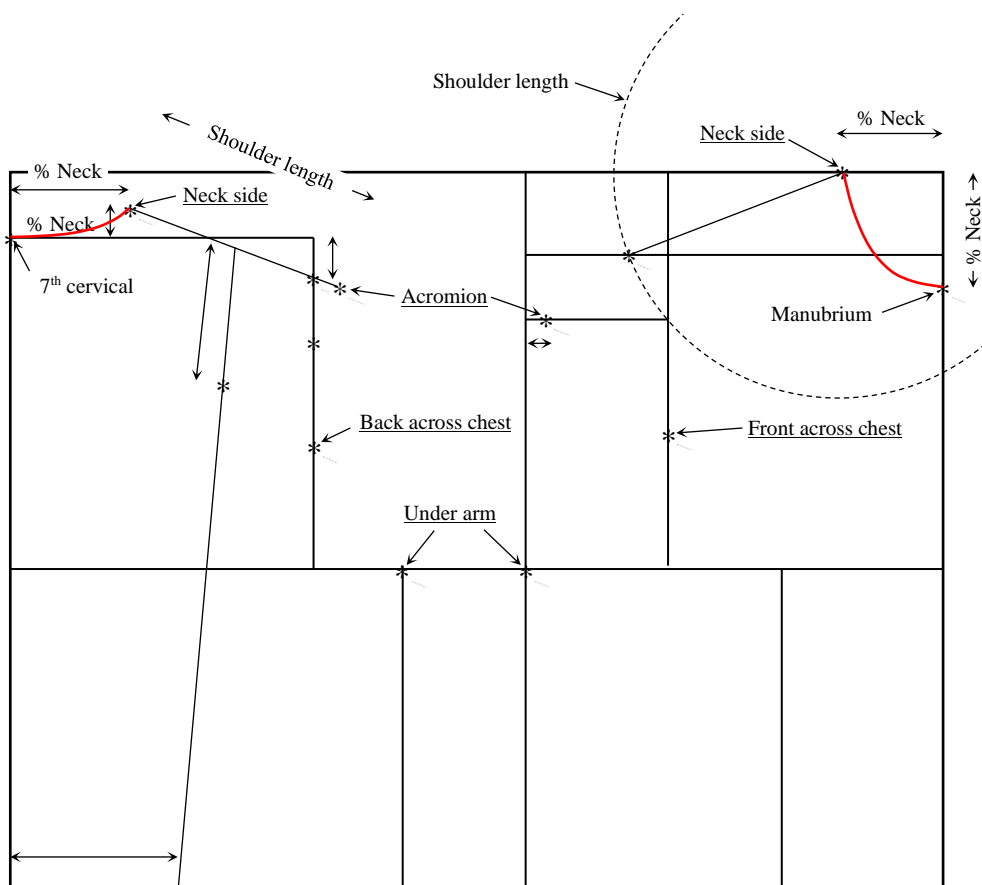
Figure 5.2: Anthropometric creation points.

To do this, it's enough to draw the front and rear contours of the block pattern (Figure 5.3: red) from the lines characterizing the morphology, passing through the anthropometric points, and integrating the clamps, which allow the flattening of the 3D pattern towards 2D. These darts are located at the chest, shoulder, and waist.
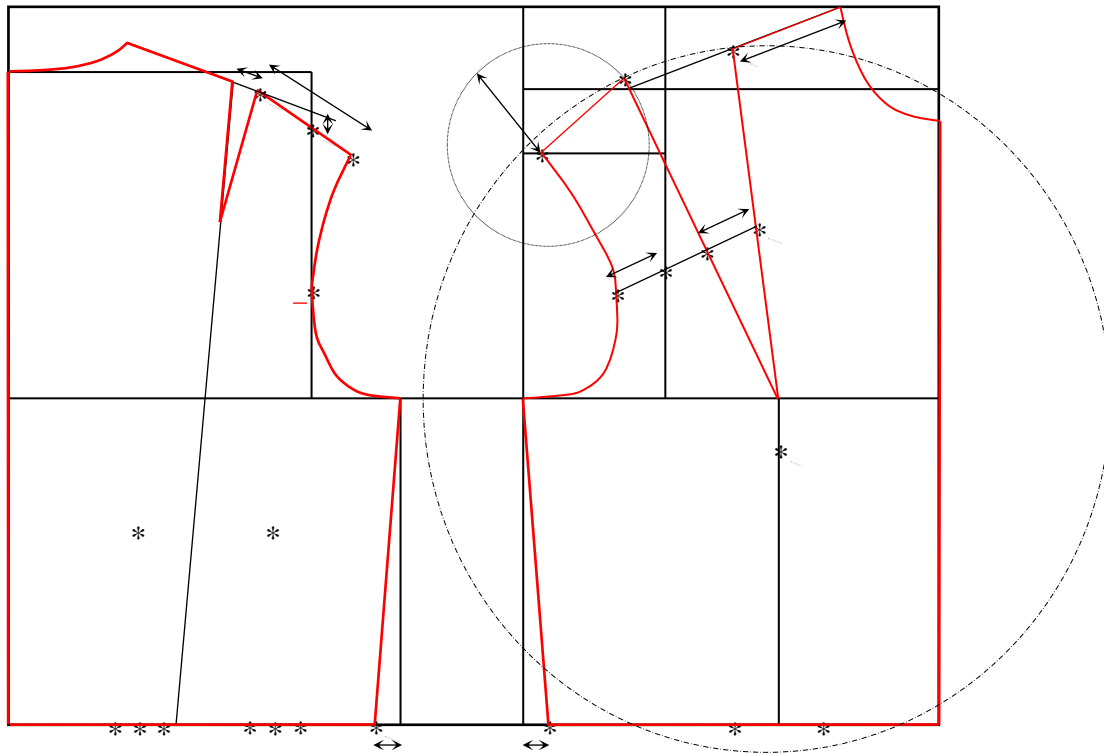
Figure 5.3: Final pattern drawing.

5.1.2   The similarity between the 3D & 2D process

The 3D creation process of the women's block pattern should follow the design logic of the 2D process. In a first step, this process should identify the morphological contours, locate the anthropometric points, and define each garment's pattern passing through these strategic points.

When creating the 3D pattern on a mannequin, some design constraints perceived in the real or virtual assembly of the product must be taken into account. These constraints located at the anthropometric point underarm are respected for the tangency of the armhole curves on the contour of the chest, a harmonious continuity of these curves between the front and the back. These constraints are not always sufficiently expressed in the 2D pattern making methods.

The difference between a 2D pattern making methods and a 3D pattern making methods is that a 2D morphological line represents a 3D morphological contour. A 2D anthropometric point is located in a 3D space. One of the biggest difference is the method to define the 3D ease

allowance of the garment. For the 2D creation process, it's enough to add a value of ease allowance on each contour or line measured on the body. On the other hand, the 3D creation process is much more precise because ease allowance is managed spatially by 3D ease allowance zones distributed over the body. We can thus manage the position, distribution, and balance of the garment relative to the wearer's body and consider morphological deformations. The 3D process also leads to the personalization of the garment. In a 2D process, these notions are considered when trying on the garment and require multiple real or virtual fittings. Their upstream integration into the 3D creation process dramatically reduces the product creation and validation cycle.

In the 3D creation process, it is imperative to anticipate the fall of the garment based on traditional methods of draping on a real body. For this, the contact and non-contact areas must be managed by 3D ease allowance by imagining that the fabric is stretched in some areas or the fabric follows a draping motion in other areas.

5.2   Analysis of the 3D creation process of the women's block pattern

The 3D garment creation process is based on a 3D graphic model developed from the conical principle of S. Efrat [138] and improved by Y.Hong [1][32] as part of the development of a product adjusted to the morphology of a person with severe scoliosis.

The women's block pattern of S. Efrat is represented by several triangular planes for the front and the back. The chest and scapulae define the four salient points of the bust (Figure 5.5(a)). These highlights represent the common starting points of each triangle for each pattern. The other two ends of the triangles are located on the outline of the relevant pattern. In accordance with the 2D pattern making methods, the contours are defined by lines (Figure 5.5(c): yellow lines) and curves (Figure 5.5(c): blue lines) created spatially and connected by their ends to the different anthropometric points of the bust (Figure 5.5(b): green dots). Other points (Figure 5.5(b): yellow dots) are strategically located on these lines and curves to improve the monitoring of the body morphology. They increase the number of triangles results in a more precise 3D surface mesh of the block pattern.
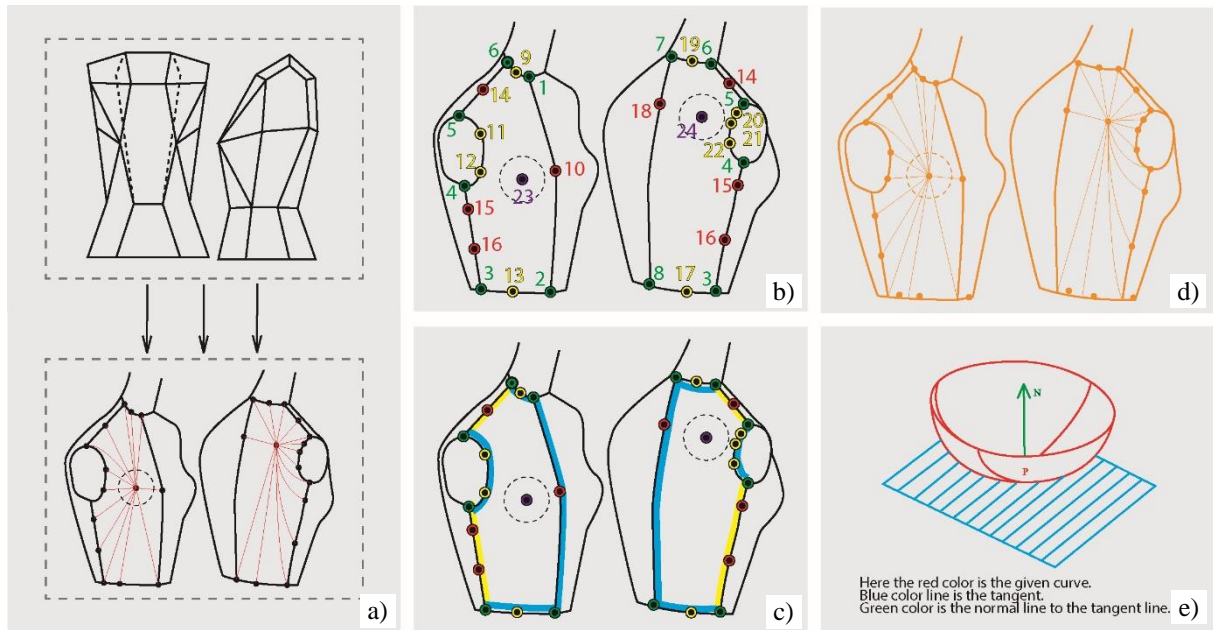
Figure 5.5: (a) classic garment block design method; (b) anatomical landmarks for garment design; (c) different shape controlling points, lines and curves; (d) garment block framework from shape controlling points of the breasts and scapular points; (e) general principle of defining the Normal Line of a curve [1][32].

A direct connection by straight lines between the four salient points and the contour points leads to flat triangles (Figure 5.5(d)), resulting in a very pronounced collision between the surface of the women's block pattern and the surface of the body. In order to avoid these collisions, the lines were then composed of a straight line at the start of the contour points. They were extended by curves tangent the zones around the salient points assimilated to spherical caps (Figure 5.5(e)). Kulinska's work also incorporates ease at the salient points (Figure 5.4) [81].
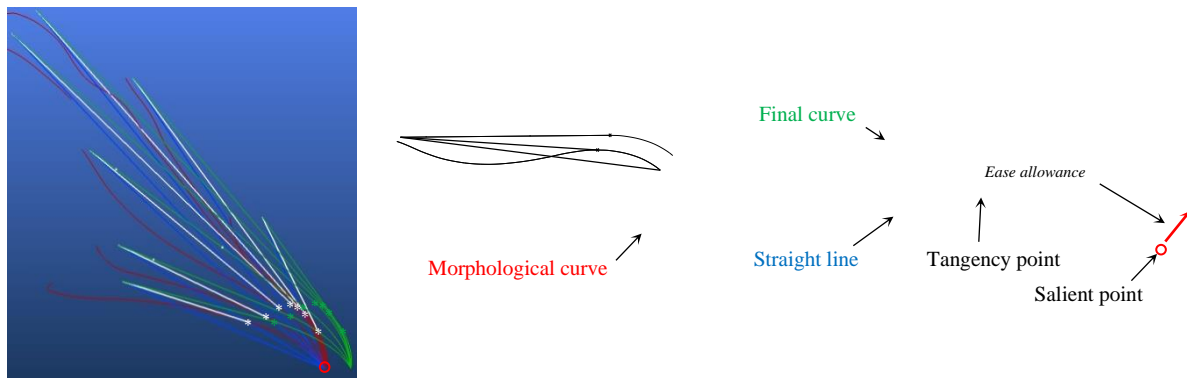
Figure 5.4: 3D ease allowance model [81].

In the case of a person with high scoliosis, tests have been carried out with the 3D graphic model by strictly following the creation strategy, which boils down to:

- Detection of anthropometric points (green star points) and adjustment of ease allowance at each anthropometric point (Figure 5.6(a)(e)),

- Detection of protruding (purple star points) and hollow parts of the body (Figure 5.6(a)(e)),

- The establishment of the limits of the garment block pattern (red lines and curves) by connecting the anthropometric points (shoulder lines, sidelines, armhole curves, the curve of the middle front, the curve of the middle back) (Figure 5.6(a)(e)),

- The positioning of strategic points on the lines and contours (red star points) defining the limits of the garment block pattern (Figure 5.6(a)(e)),

- The establishment of distribution points (red star points) between the protruding points of the chest and scapula, between the anthropometric points of the shoulder line and the sideline (Figure 5.6(a)(e)),

- The creation of straight lines (blue lines) between the salient points and the contour points of the garment block pattern (Figure 5.6(a)(e)),

- The creation of straight/curved lines (curved red lines) between the salient points and the contour points of the garment block pattern (Figure 5.6(b)(f)),

- The creation of the surfaces (red surfaces) of each pattern of the block pattern (Figure 5.6(c)(g)) on which are drawn the lines defining the location of each of the flattening clamps of each pattern (Figure 5.6(c)(g)),

- The triangular mesh of the surfaces of each pattern of the garment block pattern (Figure 5.6(d)(h)),

- The 3D-2D flattening of the meshed surfaces to obtain the four basic block patterns (Figure 5.6(i)).
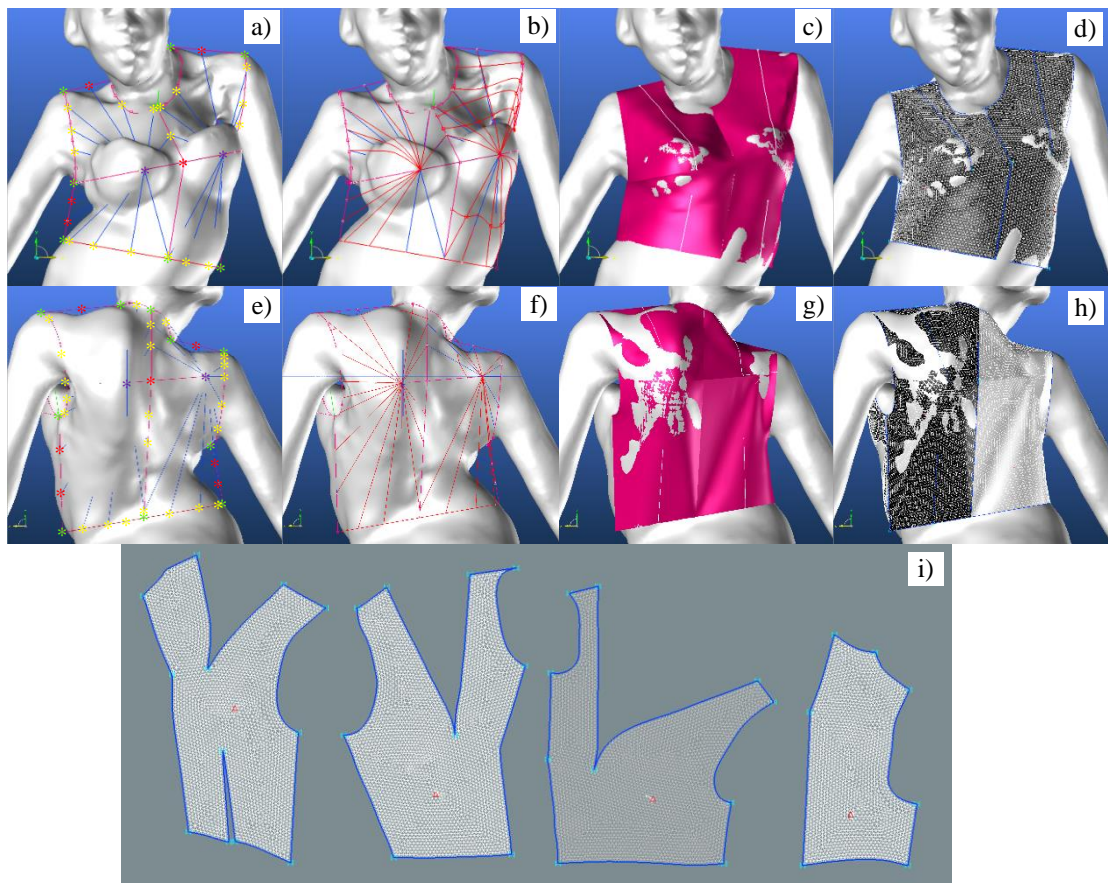
Figure 5.6: Design process for a personalized garment block.

5.3   3D creation process connected with the skeleton

The 3D creation process is interesting because it leads to a perfect garment fit for the body. It directly relates to it, with these anthropometric data and these morphological contours. We have seen that it can also be applied to atypical morphologies such as those of scoliosis or another kind of spinal disability. Numerous works show interest in this new concept of creation [2][139]. However, a drawback appears despite all these tailor-made advantages. The detection of anthropometric points and morphological contours is carried out manually and depends on the creator's finesse. Among other things, once the 3D graphic model is created, it can no longer evolve according to the evolution of the pathology.

Scoliosis is a permanent and progressive deviation of the spine. It then leads to a progressive deformation of the thorax and leads to a particular stage of the disease, a gibbosity. In the new process of creating the 3D block pattern, we must take these specifics into account. For this, the new 3D graphic model will need to be connected to the patient's skeleton with scoliosis as it completely controls the deformation of the patient's chest. Thus, the position of the

anthropometric points will be given by the bones of the skeleton. Morphological contours will be detected by cross-sections of the scanned surface of the patient's body. These contours will, of course, also be identified by the skeleton (vertebrae, sternum).

The new 3D graphic model must also consider the ease allowance of the garment. Figure 8 shows the structure of this model using the previous model's strategy with the 3D ease allowance defined by lines of ease distributed at the waist, the chest relative to the morphological contours. The 3D ease allowance is also defined on the different anthropometric points (Figure 5.7: green points). For salient points, the straight lines follow the same strategy as shown in Figure 5.7.
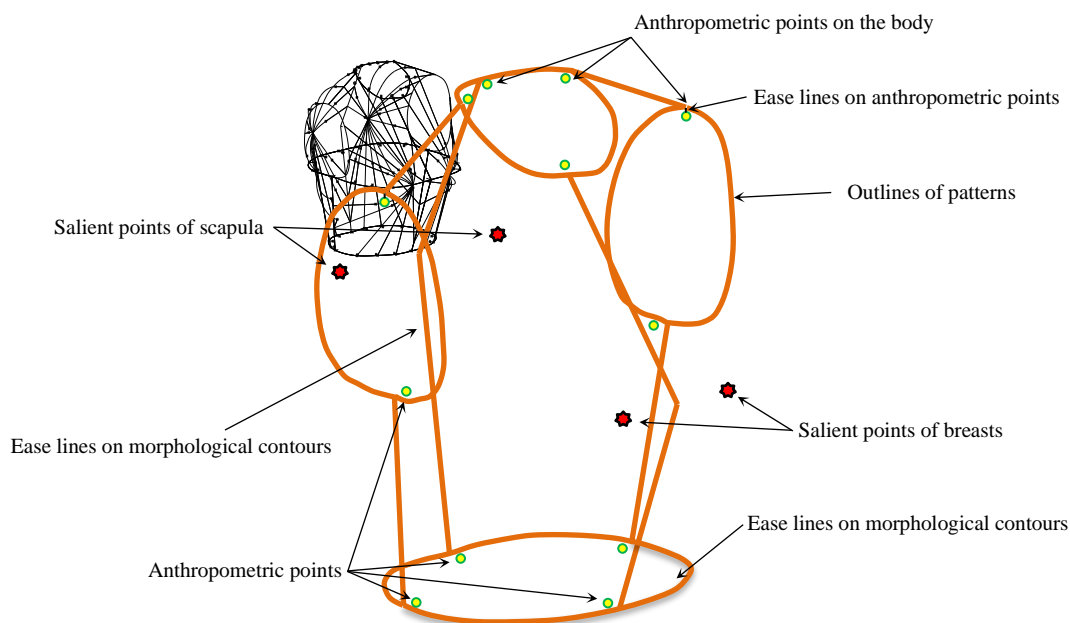
Figure 5.7: Graphic model of garment with 3D ease allowances [81].

5.3.1   3D Model of the thorax

We have seen previously that the 3D creation process must be connected with the skeleton of the thorax. We has developed an adaptive 3D thorax model, configured to adapt to any patient morphology with scoliosis. As this pathology evolves following a progressive deviation of the spine, this model adapts to the evolving deformity of the spine. As well as the angular positions of each of them under different planes (Figure 5.8(b)). The dimensional parameters of the vertebrae will then be the height and volume of the thorax. The dimensional parameters of the vertebrae will then be the height and volume of the thorax. Angular positions manage the deviation of the spine. The 3D model of each vertebra (Figure 5.8(c)) is connected to this 3D spatial path of the spine (Figure 5.8(b)). The 3D thorax model is then connected to each vertebra

via the 3D models of the ribs (Figure 5.8(d)). In parallel, a 3D scan of the patient (Figure 5.8(e)) makes it possible to obtain a 3D surface representation of the patient. We have positioned the complete 3D model of the thorax (Figure 5.8(f)). The D5 vertebra allows the 3D thorax model to be positioned with precision in the patient's scan. At this stage, we have the 3D skeleton of the patient integrated into the patient body scan and adapted to the patient's morphology at a precise moment of his pathology.
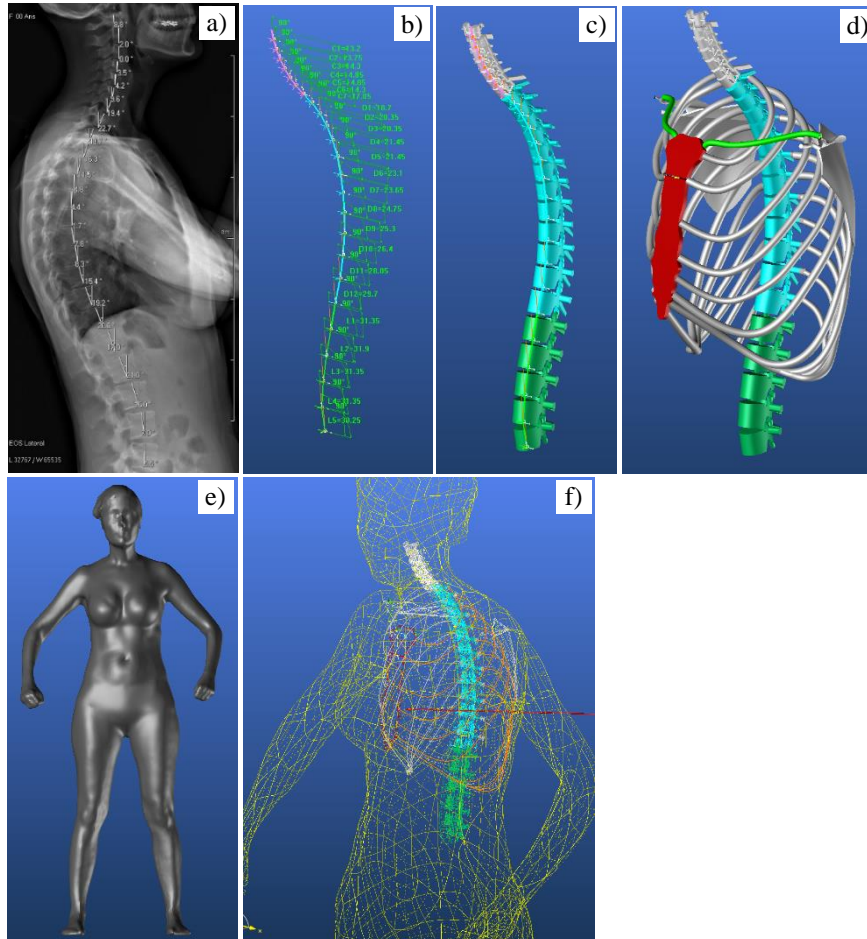
Figure 5.8: 3D model of thorax parametrized by EOS scan measurement.

Therefore, the study's objective is to use this skeleton to detect the anthropometric points and the patient's morphological contours to create a garment adjusted to this atypical morphology. This garment can then automatically adapt to the deformation of the thorax managed by the deviation of the spine.

5.3.2   Detection anthropometric points and morphological curves on the skeleton

The 3D Graphic model of a garment with 3D ease allowances starts with detecting anthropometric points on the skeleton of the 3D thorax model. We have 3 points to detect for each scapula: 1 for the acromion (Figure 5.9(a): P1), 2 for the salient points (Figure 5.9(a): P2). We have 1 point at the end of the 7th cervical (Figure 5.9(a): P3). We have 1 point on the upper/middle part of the manubrium (jugular notch between the two clavicular facets) (Figure 5.9(a): P4). Different marks are placed on the anthropometric points to create the ease allowance of each point (Figure 5.9(b): green lines).
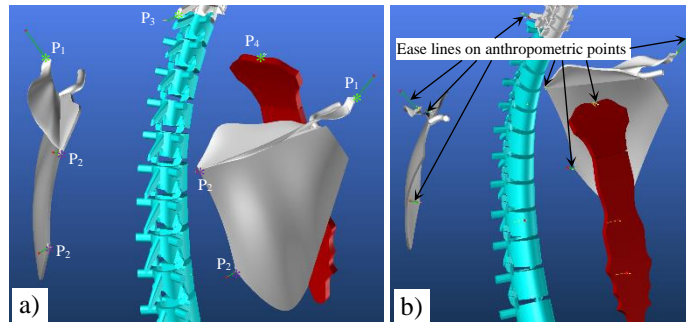
Figure 5.9: Detection anthropometric points on the skeleton, ease lines.

The next step is to detect the morphological contours (Figure 5.10(a)). For this, we created different cut marks to get the helpful cross-sections of the scanned body. A first mark, R1 placed in the middle of the lumbar vertebra L3, makes it possible to define the contour of the waist. An R2 mark placed on the sternum provides the chest contour. Its position is relative to a reference R6 located on the anthropometric point P4 (Figure 5.10(b)). The contour of the neckline is represented by two 3D curves composed of the front neckline and the back neckline defined in different planes. R6 is a pointed mark that cuts the body at the front neckline, extending the flat area above the chest. The neckline of the back uses an oriented R5 mark located on the anthropometric point P3 (Figure 5.10(b)). Two new anthropometric points, P5, can then be created at the intersection of the front and back necklines. Finally, we still must define the two middle curves of the front and the back. A reference R3 is defined as the reference R2. This mark makes
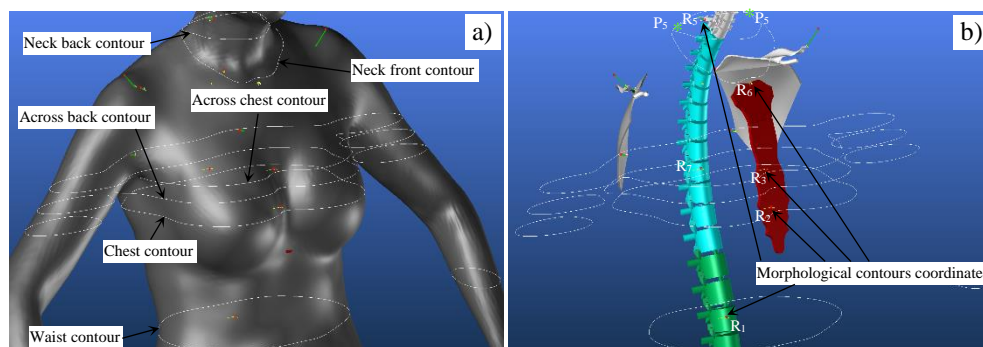
Figure 5.10: Detection morphological contours with coordinates on skeleton.

it possible to cut the body at the level of the middle part of the front. The middle of the back is obtained from the mark R7 located in the middle of the dorsal D9.

5.3.3   3D Model of Garment

With the anthropometric points and morphological curves that we detected previously, we created the different lines and curves defining the network of curves of the garment graphic model with 3D ease allowances.

The contour of the neck is a 3D curve passing through the end of the ease lines of points P3, P5, P4, P5 (Figure 5.11(a)). The shoulder lines are between P5 and the end of the point lines P1 (Figure 5.11(a)).

The different morphological contours have been shifted outwards to take into account the 3D ease of the garment. Two points P7 are then defined on the new chest contour to represent the armpit points (Figure 5.11(a)). Likewise, on the new size contour are defined two points P8 to create with P7 the two sidelines (Figure 5.11(a)). P7 and P8 result from the intersection between a distribution plan defining the proportion of the pattern of the front in relation to the back and the morphological contours of the chest and the waist [reference plan distribution]. In the same spirit, P9, P11, P10, and P12 are also the result of the intersection between a plane of symmetry and these exact contours (Figure 5.11(a)). Of course, these plans are still possible before the deformation of the spine. However, they are then adjusted according to the deformation thereof. For example, P4, P11, P9 must follow the middle front while P3, P12, P10 must follow the middle back, the spine (Figure 5.11(a)).

The armholes are positioned relative to points P1 and P7. If we analyze one side, a straight line joins the points P1 and P7, which is defined as a center of distribution of the contour points of the armhole (Figure 5.11(a)). This center point is located at the intersection between P1, P7, and the front middle plane (Figure 5.10: reference R3). Since the armhole on the front is not in the same plane as the armhole on the back, we then defined two design marks in P7, pivoting on an axis represented by the lines P1 and P7. The orientation of the benchmarks is conditioned by the position of the front and back shoulders. On each plane are created lines starting at the central point with a length such that it can define one of the contour points of the armhole of the front or the back according to the mark. The angular distribution of these lines makes it possible to position all the points necessary to create the half-contours of the armholes on the front and back.

The protruding points P6 of the front are detected on the new chest contour to create the straight lines joining the contour points of the block pattern at the level of the middle of the shoulder and the waist contour (Figure 5.11(a)). The protruding points P2 on the back are used to create the curves joining the contour points of the block pattern at the level of the middle of the shoulder and the waist contour.
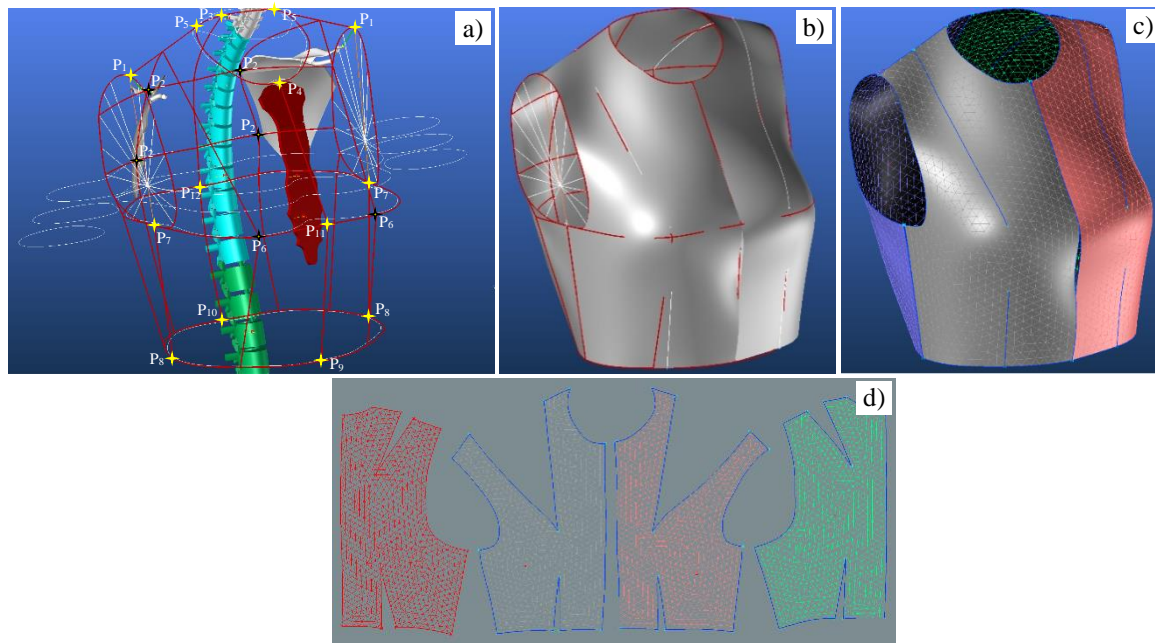
Figure 5.11: 3D Model of Garment and 2D patterns.

The network of curves and lines (Figure 5.11(b): red lines & curves) allows to create and limit the four surfaces of the women's block pattern (Figure 5.11(b)). These surfaces are meshed (Figure 5.11(c)) by integrating flattening pliers (Figure 5.11(c): blue lines). The flattening result of the four patterns is presented in Figure 5.11(d).

5.4 Results

The Graphic model of the garment with 3D ease allowances was first tested on morphology with low scoliosis (Figure 5.8). Figure 5.12 shows that overall, the basic bodice correctly follows the morphology if the dimensional parameters of the patient from the EOS scan are applied to it. Since we did not use the angles of deformation of the spine in this first phase, we notice at the end of the shoulders a slight shift caused by the asymmetry of the patient's posture (Figure 5.12(a)(c)). After applying the spinal deformation angles, the Graphic model of the garment corrected the defect in the shoulders (Figure 5.12(b)(b)). There are also other corrections to the mid-back and mid-front courses that are no longer considered linear. The middle back of the garment perfectly follows the spine.
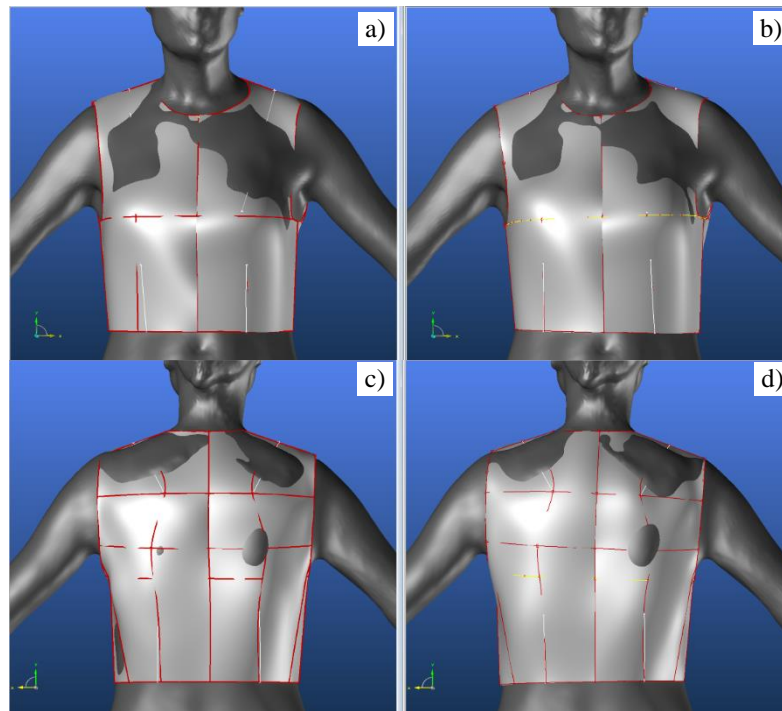
Figure 5.12 : Patient wearing garment, results before (a)((c) and after (b)(d) correction of the spine.

In the case of a more pronounced evolution of the spine, such as that of the patient of Figure 5.6, it would be sufficient to apply only the angles of deformation of the patient's spine. Figure 5.14(a)(b) gives a possible example of the evolution of the patient's basic bodice with a deformity of his spine evolving towards that of the patient with a strong deformation. This prediction makes it possible to compare the results of the flattening of this deformation (Figure 5.14(c)) with that directly obtained by the patient with high scoliosis (Figure 5.6(i)).

The 3D and 2D results of the basic bodice, in this case, are similar. They allow us to validate our Graphic model of the garment with 3D ease allowances.

This validation is all the more appreciated by creating a complementary rotation in the transverse plane. A shift is detected in the upper part of the shoulder blades when comparing Figure 5.14(b) and Figure 5.13(a). This shift is reflected directly on the dart opening of each scapula by comparing Figure 5.14(c) and Figure 5.13(b).
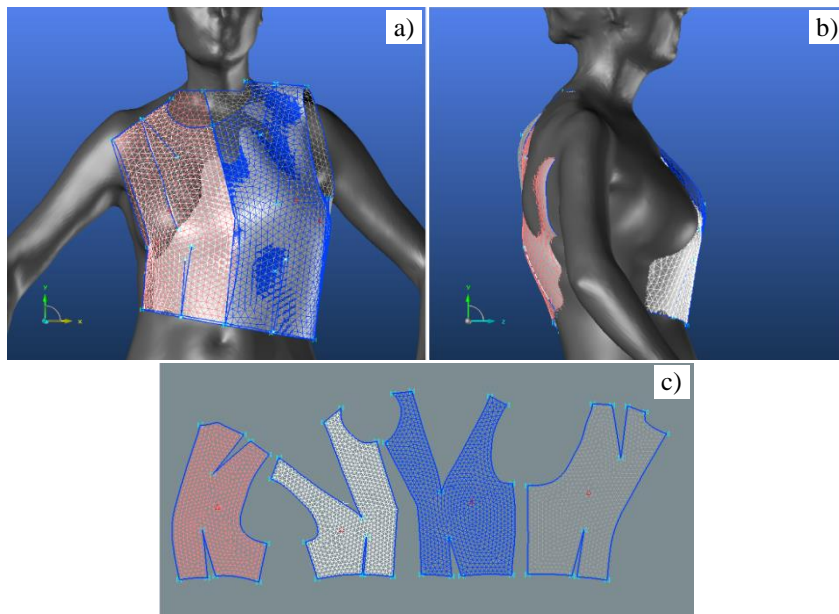
Figure 5.14: 3D predictive Model of Garment and 2D patterns.
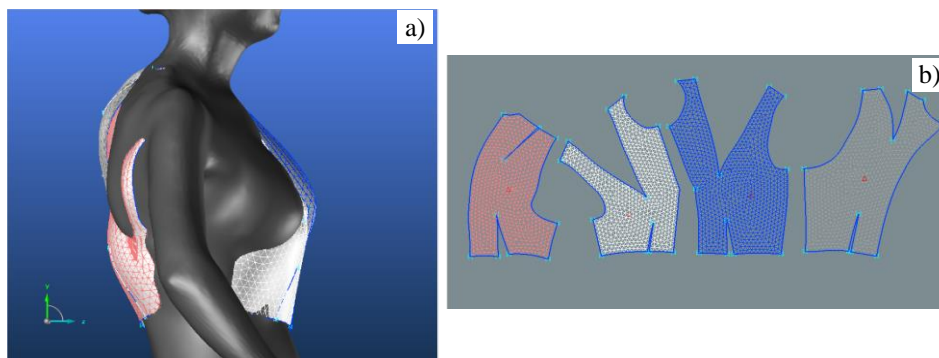
Figure 5.13: 3D/2D Model with transverse rotation.

5.5 Conclusion

This study offers a new 3D garment creation process from the skeleton and a 3D scan of a patient's body with scoliosis. This work aims to automatically obtain the new 3D block pattern each time the patient's pathology is detected. Among other things, expertise was necessary to create the product in 3D directly on the patient. In addition, the patient also had to be scanned each time to obtain the new morphology. This new process is based on a Graphic model of the garment with 3D ease allowances.

The Graphic model of the garment is connected to a 3D model of the thorax to give us the exact position of the anthropometric points. The 3D model of the thorax also gives us the position of the morphological curves on the 3D body scan. The results show that all of this data is necessary and sufficient to create a patient's block pattern. They also show that, during the spine

deformation, this phenomenon is transmitted to the 3D model of the thorax and then to the 3D graphic model of the garment. It was from the patient's EOS scan and the analysis of the spatial position of each vertebra that we were able to correct the shape of the spine.

It is important to clarify that it is essential to initialize the process with the two scans coming from EOS scanner and the body scanner. Then, the images from EOS scanner are sufficient to control the spine's shape and predict the new 3D block pattern by our two models: 3D model of thorax, 3D Graphic model of the garment.

This technique of controlling ease allowance in a 3D space is essential because it will make it possible to manage comfort by zone, as will be presented in the next chapter.

CHAPTER 6: THERMAL COMFORT FOR HUMAN BODY

The comfortable climate is usually defined as "the condition of mind that expresses satisfaction with the thermal environment" [140][141]. The human climate experience is essentially an interaction between six parameters, air temperature, mean radiant temperature, relative air movements, air humidity, activity level, and thermal properties of clothing and seat. It is also possible to further divide the physical comfort sensation into two categories, local and whole-body thermal comfort. The whole-body value only consists of a mean value, while the local values consider effects on different body parts.

Human thermal comfort is a combination of mental feeling and several goals interaction with the environment (rate of heat transfer and mass) regulated by the brain. Comfort depends on several physical quantities that we may group as:

Person-related. Deep body temperature in humans is always close to 37 ºC independent of environmental temperature, as first measured in the 1660s by Boyle. It may depart a few degrees under unhealthy circumstances, particularly above that value, as with fever or during heavy physical exercise. We must continuously evacuate heat through our skin to the ambient to compensate for our metabolic dissipation, with a baseline rate of about 1 W/kg, increasing with physical activity up to 5 W/kg. It is around 100 W for an adult in office work. Skin temperature is usually below 33 ºC, allowing the heat outflow, but it depends on external conditions, clothing, and actual and previous activity levels. Besides, age and risk groups (babies, elders, ill persons), previous accommodation (changing from indoors to outdoors), habits (difference among seasons and sex), personal preferences (some people feel comfortable, cold or hot), and actual mood (the state of mind, feeling happy or nervous) may have an influence.

Environment-related. Air temperature, radiant background temperature (of walls, sky, and Sun, if any), air relative humidity, and wind speed. And not only average values matter, but their gradients and transients too. Non-thermal environmental variables like ambient light and noise may affect the thermal sensation too. The most difficult measure of thermal comfort parameters is the radiant background temperature, which depends on direct solar irradiance, wall solar reflectance, sky temperature, wall temperature, and all the geometric view factors involved.

The nature of the human body is to maintain a constant body core temperature under different thermal disorders. Under adequate conditions, a constant core body temperature of 36.5

°C is maintained within a narrow range between 36 °C – 38 °C (normal range at rest), and up to 41 °C for heavy exercise. Body temperature regulation represents the balance between heat production from metabolic sources and heat loss (evaporation, radiation, convection, and conduction). Exposure of the human body to extreme environmental conditions can result in poor regulation of the core body temperature, thus inducing hyperthermia and hypothermia. In addition, if the body core temperature exceeds the normal narrow range, human body functions could be severely affected.

Humans can survive exposure to a remarkably broad range of environmental thermal stressors and alterations in the distribution and magnitude of internal energy generation, all while maintaining the nearly constant core temperature necessary for health and well-being. The thermoregulatory system consists of thermal sensors and diverse actuators located throughout the body. A continual stream of input signals is integrated and processed in a multicomponent distributed controller that regulates blood flow magnitude and distribution throughout the body in coordination with various metabolic activities while balancing other control needs such as maintaining blood pressure. Maintenance of homeostasis depends directly on effective thermoregulation, and therefore, it has been the subject of widespread research for many, many years. There is a compelling rationale for modeling and simulation of the thermoregulatory behavior in humans, including enhancing the ability to understand foundational physiological principles and processes, to design systems and processes that interface with or enhance thermoregulatory function, and to identify performance limitations and conditions of danger both for stressful environments and for devices to provide thermal therapies or physical performance amplification.

6.1   The human temperature regulation

The human temperature regulation system allows physiological alteration to a thermal tension and the establishment of thermal comfort of the body under an assortment of situations. The heat is mainly produced by metabolism, which originates from ingestion and muscle activity. In normal situations, this results in an average temperature of the body of about 37 °C. Inside a particular interval, the human temperature control system tries to keep this temperature when internal or external thermal disturbances occur. The effects resulting from a change in climatic conditions produce a reaction within the body regarding independent physiological responses and activate behavioral regulation. The hypothalamus controls the autonomic regulation, controlling

the different avenues of heat loss with the skin, blood, sweating, and breathing. Behavioral regulation can be active body movements and adjustment of clothing.

A person at rest produces around 100 W of heat. If clothing and ambient conditions are suitable, the same amount of heat is lost to the environment. Whole-body heat balance is sufficient, and the person is in natural thermal condition. With increasing ambient temperature, convection and radiation diminish. Sweat evaporation must recompense to balance the heat production of 100 W. Sweating is related to a sensation of warmth and eventually discomfort. In a cold environment, convection and radiation are efficient, making total heat losses bigger than 100 W. The physiological response reduces through the skin and extremity blood flow to lower the external temperature incline. In this case, the person feels cold and uncomfortable. In other words, for comfortable climatic conditions, the dry heat loss can only vary within a certain narrow interval. Similarly, the heat balance of a skin segment can be analyzed. Only for a certain narrow range of convective, radiative, and conductive heat losses, an optimal local heat balance and a "comfortable" skin temperature maintained. Higher local heat losses will be felt as cool or cold and lower local heat losses as warm.

The human response to the thermal environment can be found to depend mainly on six factors:

- Air temperature
- Mean radiant temperature
- Air velocity
- Relative humidity
- Physical activity
- Clothing thermal resistance.

In terms of thermal feeling in the face of changing environmental factors, human body modeling is a topic that researchers have considered for years in terms of applications in architecture, design of cooling and heating systems, aerospace industry, medical sciences, etc. In recent decades, many models have been proposed in thermal comfort modeling, which each has capabilities and limitations [142]. Most existing models for predicting body temperature conditions are based on the energy balance equation for the body. These models divide the body into different parts and layers and evaluate the body's thermal conditions by writing the energy

balance equation and obtaining the temperature for each part and layer. Among the available models to predict the thermal comfort of residents can be used Fangar model [83] and is mentioned as the most famous steady model, and the Gage model [143] as the most well-known non-steady model. In addition, these two models use a relatively simple approach to assess body temperature conditions and, because of this simplicity, have been cited in the ISO [144] and Ashrae [140] standards. In these models, the clothes are modeled very simply and in the form of a uniform coating on the skin's entire surface. However, part of the body surface is covered in real conditions, and the other part is not covered.

The thermophysiological models include two systems (Figure 6.1), a controlled passive system and the active system [85]:
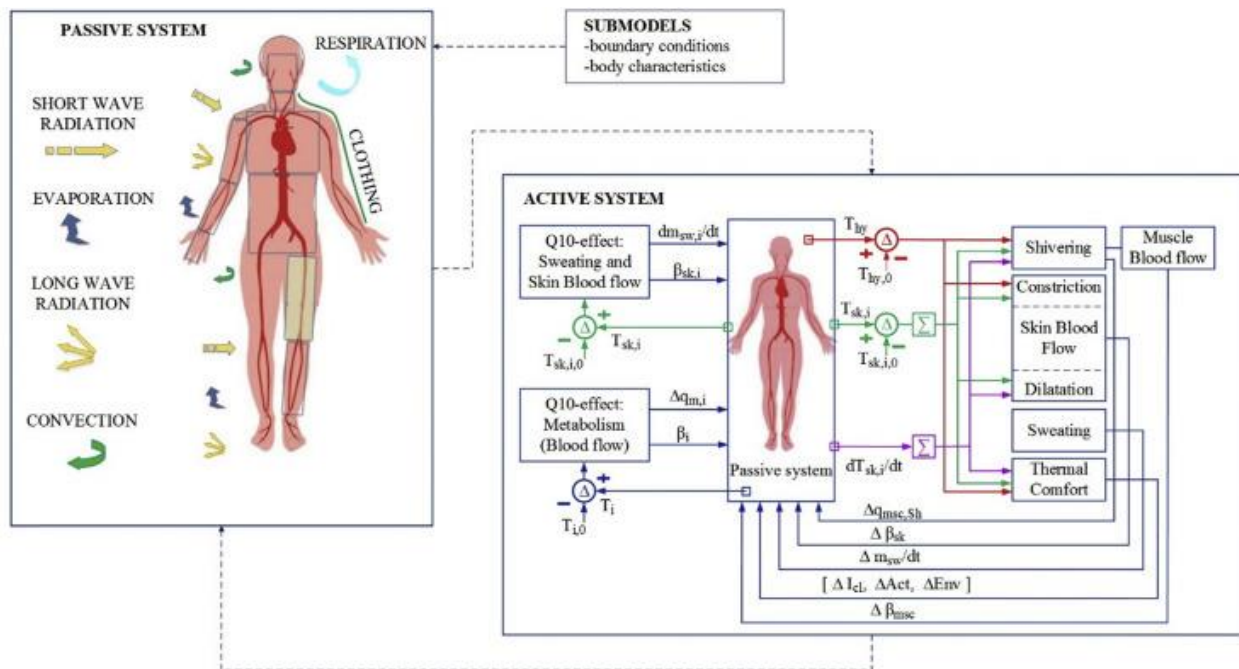
Figure 6.1: Schematic diagram of the thermophysiological models.

• The passive system simulates the physical human body and models heat transfer within the human body and between the human body and its environment [145]. Heat is continuously generated in the human body by metabolic processes and distributed over the body areas by blood circulation. For the calculation of internal heat transfer and body heat exchange, thermal properties of the blood, muscle, fat, and bones are critical parameters [146]. Through the body tissue layers, heat is transferred to the clothing-insulated body surface by conduction [85]. Heat is then exchanged with the environment through a complex combination of conduction, convection, radiation, and evaporation[147]. The clothing worn by humans is an influential factor in heat exchange with the environment as well.

• The active system is controlled by a human body's active system in order to regulate the temperature in a changing environment [148]. The active system simulates the human body's regulatory responses of vasoconstriction, vasodilation, shivering, and sweating [86]. The mean skin temperature, core temperature, and the rate of the change in skin temperature are the main signals for the active system [145]. The change in brain temperature above the set point results in vasodilation. When vasodilation is not sufficient to lose heat from the body, sweating is activated for the heat loss process. Vasoconstriction is a result of the reduction in skin temperature [146]. However, if the body is exposed to a cold environment and vasoconstriction is not enough to maintain the heat in the body, the body will start to shiver to retain heat. Furthermore, the skin blood flow is controlled by the mechanisms of vasodilation and vasoconstriction.

The thermal balance of the body is influenced by local environmental conditions and individual physiological characteristics. The environmental parameters (air temperature, mean radiant temperature, air velocity, and relative humidity) and human physiological inputs (metabolic rate, height, weight, fat percentage, blood flow rate, gender, skin surface area, etc.) serve as model inputs (Figure 6.2). As output, the models can predict local skin temperature and the body's core temperature.
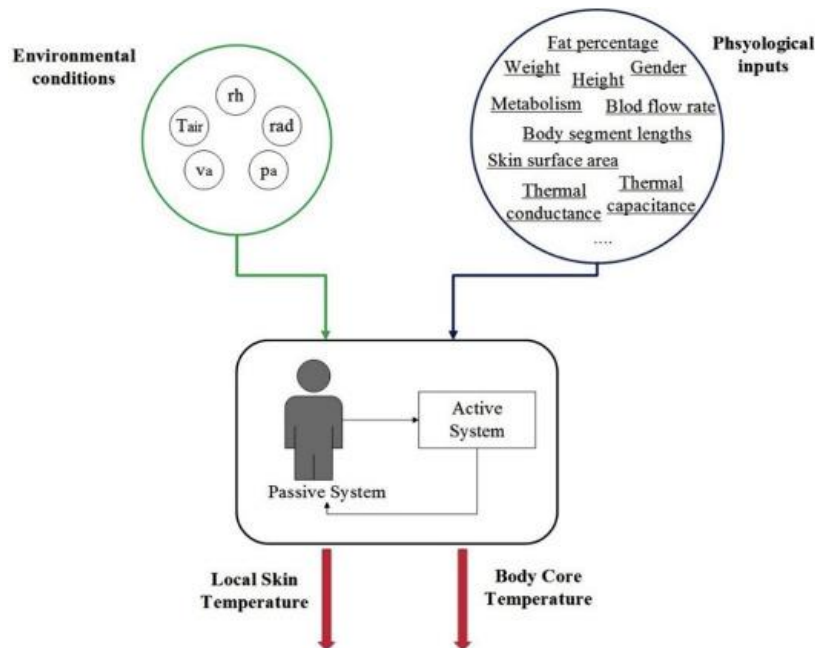
Figure 6.2: Schematic view of the inputs and outputs for thermophysiological model.

In the past 60 years of study in thermal comfort, predicting the comfort situation and standards were more supported as indoor thermal comfort indices that are still the most widely utilized in the field today [149][83]. Both indices modeled the human body as a uniform heating

element and clothing as the uniform heat resistance on the human body surface, limiting the application of these indices to uniform conditions with few distributions. However, people are often exposed to non-uniform thermal environments, and each human body segment has physiological and geometric characteristics and clothing insulation of each segment. Therefore, a thermoregulation model of the human body, which enables detailed consideration of non-uniform conditions, is required to assess such environments as car cabins, air-conditioned task spaces, and outdoors.

In this study, to understand the human body's comfort in different conditions, the multi-node thermoregulation model was used, and it was developed based on the Stolwijk model [84]. The multi-node model has 16 body segments corresponding to the segmented thermal manikin.

6.2 Air Gaps

Air gaps entrapped between the skin and inner surface of clothing can be considered a microclimate, influencing the thermal feeling of the human body and thermoregulatory response of the body [150]. Some researchers have investigated the influence of air gap distributions on the protective performance of thermal protective clothing. Most of the research is based on measuring temperature and the value of moisture in different air gap and different garments.

The clothing system's heat and mass transfer comprise several physical processes, such as dry heat exchange (conduction, convection, and radiation), evaporation and condensation, sorption, and vapor and liquid water transfer. Also, factors associated with the construction and use of the garment, such as air penetration and compression by wind, body posture and movement, and clothing fit, significantly influence these processes. This is achieved mainly by changing the size and the shape of the layers of air trapped between the skin and clothing, the clothing layers, and the air layer adjacent to the outer surface of clothing. Thus, the thermal, wicking, and evaporative properties of clothing depend not only on the properties of the fabric used for the garment but also on the magnitude of the contact area and air layers' thickness and change. Clothing is generally flexible, and it drapes and sags with its weight. Effectively, the air layer's thickness is inhomogeneous and varies over body parts and changes with body shape, established posture, and movement. The air layers' inhomogeneous thickness within the clothing system influences the local intensity of heat and vapor exchange. Moreover, the air trapped underneath garments adjacent to the outer layer provides the bulk of both thermal and evaporative resistances.

When exposed to a cold environment, the warm and relatively still air layer prevented the human body from freezing. In a hot environment, the air gaps under the garment provided thermal insulation from the heat and protected the body from heat stress. Thus, air gaps played an important role in the process of heat transference from the human body to the environment.

Guowen Song used a three-dimensional body scanning technique to measure the air gap layer distribution between different-sized protective garments and the body of a manikin used to evaluate garment thermal protective performance [151]. Jun Li proved that the thermal insulation of experimental shirts increased with air gap sizes but began to decrease due to natural convection when the air gap thickness was higher than 1 cm or the air gap volume was greater than 6000 cm3 [152].
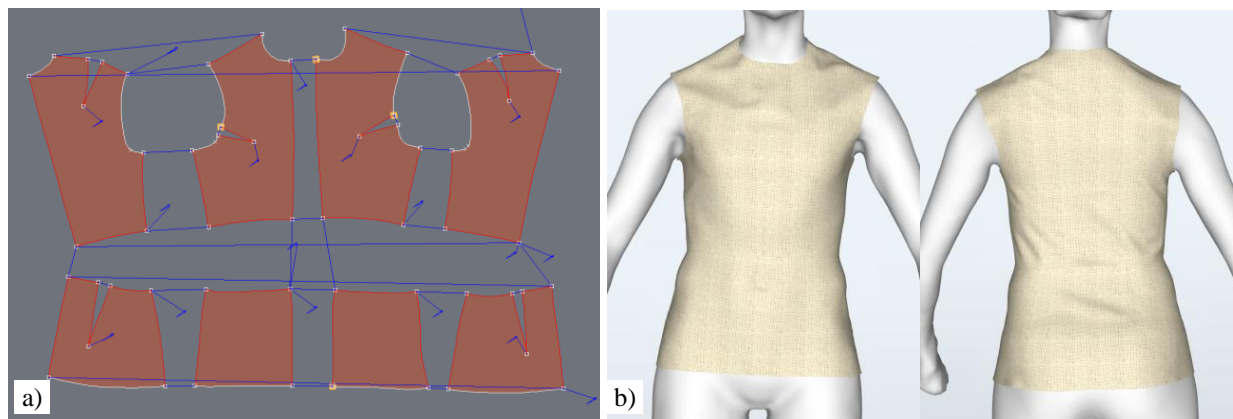
Figure 6.3: (a) 2D pattern from Design concept, (b) Garment [sewn] on 3D virtual model.

In this study through the air gap thickness of different fit clothing obtained from our Graphic model of garment which have the capability to adjust the 3D ease allowance for different zone of garment, a mathematical model to predict the effect of the air gap on the clothing temperature and heat loss of a clothed human body, the suitable in the air gap in term of comfort temperature can be optimized. Figure 6.3a shows the 2D pattern of the garment come from the flattening of 3D garment model, which can change in different fit, and the Figure 6.3b shows the 3D virtual try on of the garment in different fit, in this figure, the garment is close to the body.

Five different fits for a shirt were tested (A, B, C, D, E). All the garments have the same pattern design and are made of the same cotton plain fabric   . The only difference is the the value of 3D ease allowance. The ease allowance we have defined previously in the graphical model of garment (Figure 5.7) can be considered a 2D/3D ease allowance per zone as shown in Figure 6.4. Two techniques of ease allowance management are proposed, i.e.: by contact, by anthropometric curves [81]. The ease allowance by contact appears in a level of the chest and scapula's. It is a 3D ease allowance which is widely distributed on these two zones. The 2D ease allowance by anthropometric curves is defined in the contour plane concerned. At the level of the neck, the ease allowance is in 3D.

Table 6.1: Fabric specification [153].

Fiber type	Cotton
Weight, g/m^2	126
Thickness, mm	0.312
Warp density, 1/10 cm	585.6
Weft density, 1/10 cm	284
Thermal resistant, clo	0.155
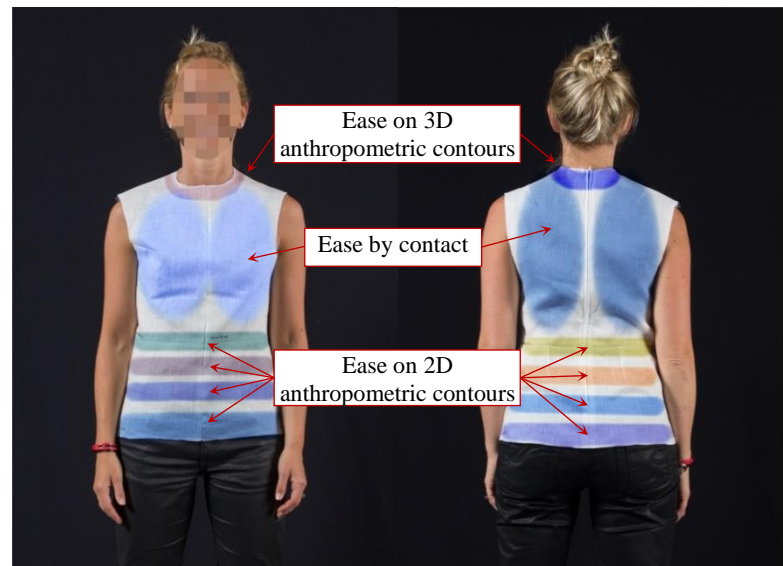
Figure 6.4: Ease allowance managed by zone.

Table **6.2** shows that the five garments' air gap thickness and value increased with the

Garment code	A	B	C	D	E
Air gap thickness, cm	0.5	0.8	1.15	1.55	1.95

garment size.

Table 6.2: Average airgap size.

Garment code	A	B	C	D	E
Air gap thickness, cm	0.5	0.8	1.15	1.55	1.95

6.3   Multi-node model with garment layer

Human beings can adjust heat balance with the environment through thermoregulation and behavioral regulation. Human skin temperature changes dynamically according to human metabolic heat production, the air gap, clothing insulation, and environmental conditions, influencing heat loss from a clothed human body.

To simulate the effect of air gap thickness on heat exchange between the human body and the environment, a mathematical model is developed to include human thermoregulatory and dry and evaporative heat transfer from the skin to the environment through clothing.

The starting point is Stolwijk's model of thermoregulation, which has been developed to 65 nodes by 16 segments four layers and central blood (Figure 6.5). In this thesis with additional a model is proposed by developing the 65 node model by adding two more layers, inner layer, and outer layer of clothing.

Core, muscle, fat and skin layers
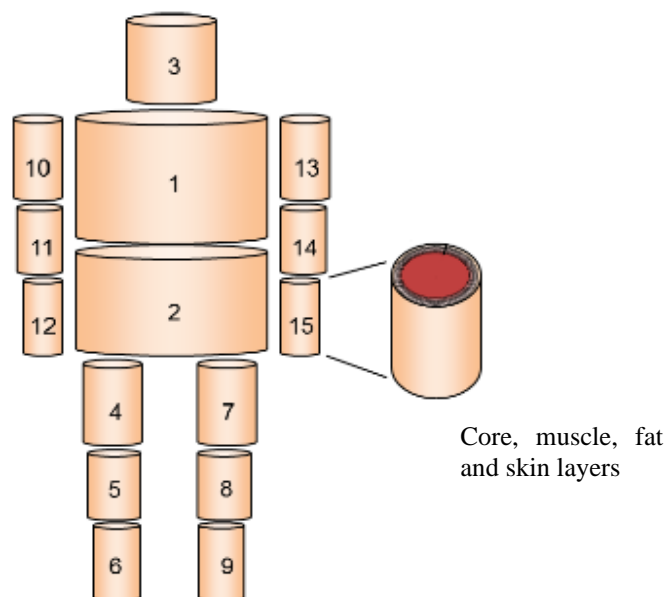
Figure 6.5: Segmentation of 65 nodes model.

This new model has 16 segments corresponding to the segmented thermal manikin , and each segment is composed of six concentric layers: core, muscle, fat, skin, and inner and outer layer of clothing, plus central blood compartment. Heat balance equations for the six layers and central blood compartment can be expressed as following equation by defining for each layer and segment heat capacity $C(i,j)$, heat production $Q(i,j)$, heat transfer by blood flow to layers, heat transmitted by conduction $D(i,j)$ between layers, heat loss by respiration $RES(i,1)$ in core layer and evaporation heat loss at the skin surface $E(i,4)$:

Core layer:

$$C(i,1)\frac{dT(i,1)}{dt} = Q(i,1) - B(i,1) - D(i,1) - RES(i,1) \qquad (6.1)$$

Muscle layer:

$$C(i,2)\frac{dT(i,2)}{dt} = Q(i,2) - B(i,2) + D(i,1) - D(i,2) \qquad (6.2)$$

Fat Layer:

$$C(i,3)\frac{dT(i,3)}{dt} = Q(i,3) - B(i,3) + D(i,2) - D(i,3) \qquad (6.3)$$

Skin layer:

$$C(i,4)\frac{dT(i,4)}{dt} = Q(i,4) - B(i,4) + D(i,3) - Q_t(i,4) - E(i,4) - Q_{nc}(i) \quad (6.4)$$

And for two new layers:

Inner layer:

$$A_n(i)L_{nc}(i)C_{nc}(i)\frac{dT(i,5)}{dt} = Q_{nc}(i) - Q_f(i) \qquad (6.5)$$

Outer layer:

$$A_{cl}(i)M_f(i)C_f(i)\frac{dT(i,6)}{dt} = Q_f(i) - Q_a(i) \qquad (6.6)$$

Central blood:

$$C(central\ blood)\frac{dT(central\ blood)}{dt} = \sum_{i=1}^{16}\sum_{j=1}^{4} B(i,j) \qquad (6.7)$$

Where,

$i(1\ to\ 16)$ represents the sixteen segments of the body,

$j(1\ to\ 6)$ represents the six concentric layers,

$Q_{nc}(i)$ is the direct heat transfer from the skin to the inner layer of the fabric for a clothed body segment,

$Q_f(i)$ is the direct heat transfer from the inner layer to the outer layer of the fabric,

$Q_a(i)$ is the direct heat flux transfer from the outer fabric layer to the environment,

$A_n(i)$, $A_{cl}(i)$ (Table 6.3: $An(i)$ and $Acl(i).$) are the surface area of the body and clothing, respectively,

$L_{nc}(i)$ is the air gap thickness of segment I,

$C_{nc}(i)$ is the volume heat capacity of air,

C_f is the specific heat of the fabric,

M_f is the mass of the fabric.

Table 6.3: $A_n(i)$ and $A_{cl}(i)$.

i	Segment (i)	A_n (i) (m²)	A_{cl} (i)(m²)
1	Head	0.140	0.1400
2	Chest	0.175	0.1886
3	Back	0.161	0.1735
4	Pelvis	0.221	0.2347
5	L-shoulder	0.096	0.1020
6	R-shoulder	0.096	0.1020
7	L-arm	0.063	0.0669
8	R-arm	0.063	0.0669
9	L-hand	0.050	0.0500
10	R-hand	0.050	0.0500
11	L-thigh	0.209	0.2220
12	R-thigh	0.209	0.2220
13	L-leg	0.112	0.1189
14	R-leg	0.112	0.1189
15	L-foot	0.056	0.0560
16	R-foot	0.056	0.0560

Figure 6.6 illustrates this new system by considering the new two layers for cloth and the connection between body and cloths and how they effect on each other and how the environment and the temperature of core of body can effect on skin and garment.

6.3.1   Heat capacity

$C(i,j)$ and $C(central\ blood)$ are the heat capacity of the body node and central blood node, and $T(i, j)$ is the temperature of the body and clothing layer; $T(central\ blood)$ is the temperature of the central blood node. $C(i,j)$ calculated from the specific heat of tissues that constitute each node is shown in Table 6.4.The specific heat of individual tissue was assumed as follows: bone 0.580 Wh/(kg °C), fat 0.696 Wh/(kg °C), other tissues 1.044 Wh/(kg °C). Blood volume in the central blood compartment was assumed as [154] .
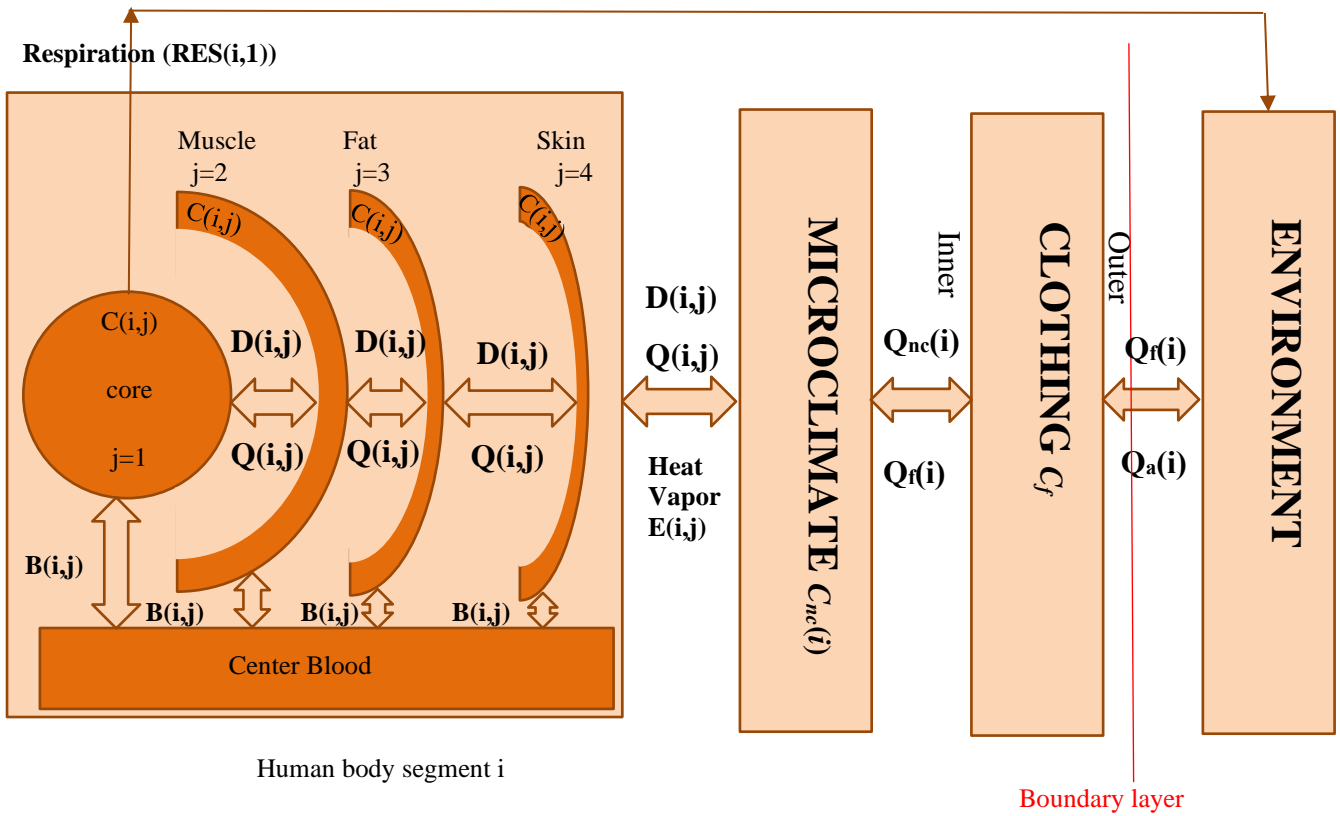
Figure 6.6: Human body/ clothing / environment system.

6.3.2   Heat production

$Q(i, j)$ is the total metabolic heat production, $Q(i, j)$ is the sum of the basal metabolic rate $QB(i, j)$, heat production due to external work $W(i, j)$ and shivering $CH(i, j)$. As the extra work and shivering only occur in the muscle layer ($j = 2$), and $W(i, j) = CH(i, j) = 0$ for other layers ($j \neq 2$) [155]:

$$Q(i,j) = QB(i,j) + W(i,j) + CH(i,j) \tag{6.8}$$

$$W(i,2) = 58.2(met - QB)A_n Metf(i) \tag{6.9}$$

Where,

met is the metabolic rate of the whole body,

QB the basal metabolic rate,

A_n is the surface area of the body.

125

QB is obtained from the sum of the basal metabolic rate of all nodes, 0.778 met. When the value of *W(i, 2)* is negative, it is considered 0. *Metf(i)* is the distribution coefficient of individual muscle layer for heat production by external work, and the values are also shown in Table 6.5.

Table 6.4: *C(i,j)* (Wh/°C) for central blood=2.610.

i	Segment (i)	Core	Muscle	Fat	Skin
1	Head	2.576	0.386	0.258	0.282
2	Chest	2.915	5.669	1.496	0.418
3	Back	2.471	5.022	1.322	0.386
4	Pelvis	6.017	7.997	2.102	0.606
5	L-shoulder	0.503	1.078	0.207	0.151
6	R-shoulder	0.503	1.078	0.207	0.151
7	L-arm	0.321	0.681	0.131	0.099
8	R-arm	0.321	0.681	0.131	0.099
9	L-head	0.082	0.037	0.052	0.099
10	R-head	0.082	0.037	0.052	0.099
11	L-thigh	1.665	3.604	0.560	0.423
12	R-thigh	1.665	3.604	0.560	0.423
13	L-leg	0.793	1.715	0.268	0.204
14	R-leg	0.793	1.715	0.268	0.204
15	L-foot	0.139	0.037	0.077	0.125
16	R-foot	0.139	0.037	0.077	0.125

Table 6.5 *QB(i,j)* (W) and *Metf*(i).

i	Segment (i)	Core	Muscle	Fat	Skin	Metf(i)
1	Head	16.843	0.217	0.109	0.131	0.000
2	Chest	21.182	2.537	0.568	0.179	0.091
3	Back	18.699	2.537	0.501	0.158	0.080
4	Pelvis	8.050	4.067	0.804	0.254	0.129
5	L-shoulder	0.181	0.423	0.610	0.050	0.026
6	R-shoulder	0.181	0.423	0.610	0.050	0.026
7	L-arm	0.094	0.220	0.031	0.026	0.014
8	R-arm	0.094	0.220	0.031	0.026	0.014
9	L-hand	0.045	0.022	0.023	0.050	0.005
10	R-hand	0.045	0.022	0.023	0.050	0.005
11	L-thigh	0.343	0.824	0.151	0.122	0.201
12	R-thigh	0.343	0.824	0.151	0.122	0.201
13	L-leg	0.102	0.220	0.035	0.023	0.099
14	R-leg	0.102	0.220	0.035	0.023	0.099
15	L-foot	0.122	0.035	0.056	0.100	0.005
16	R-foot	0.122	0.035	0.056	0.100	0.005
	Total	–	–	–	84.652	1.000

6.3.3   Heat transfer by blood flow

$B(i, j)$ is the heat exchanged between each node and central blood compartment and is expressed by $B(i,j) = a\rho CBF(i,j) - T(central\ blood)$ $\qquad$ (6.10). a is the ratio of counter-current heat exchange, and ρC is the volumetric specific heat of blood. In this paper, it is assumed that $a=1.000$, $\rho C=1.067$ Wh/(l °C). $BF(i, j)$ is the blood flow rate. $BF(i,j) = BFB(i,j) + (W(i,j) + CH(i,j)1.16$ $\qquad$ (6.11) expresses the blood flow rate for each layer except for the skin. T(central blood) is the blood temperature in the central blood compartment.

$$B(i,j) = a\rho CBF(i,j) - T(central\ blood) \qquad (6.10)$$

$$BF(i,j) = BFB(i,j) + (W(i,j) + CH(i,j)1.16 \qquad (6.11)$$

In $B(i,j) = a\rho CBF(i,j) - T(central\ blood)$ $\qquad$ (6.10), $BFB(i, j)$ is the basal blood flow rate, and values used in this model are shown in Table 6.6. It was assumed that the blood flow of 1.0 l/h was required for 1.16 W heat production.

Table 6.6: $BFB(i, j)$ (l/h).

i	Segment (i)	Core	Muscle	Fat	Skin
1	Head	45.000	0.870	0.340	2.240
2	Chest	77.850	7.660	1.340	1.800
3	Black	76.340	7.660	1.340	1.350
4	Pelvis	18.190	12.280	2.160	2.080
5	L-shoulder	0.320	1.280	0.160	0.860
6	R-shoulder	0.320	1.280	0.160	0.860
7	L-arm	0.160	0.670	0.085	0.450
8	R-arm	6.160	0.670	0.085	0.450
9	L-hand	0.091	0.078	0.042	0.910
10	R-hand	0.091	0.078	0.042	0.910
11	L-thigh	0.364	0.855	0.150	0.380
12	R-thigh	0.364	0.855	0.150	0.380
13	L-leg	0.071	0.070	0.019	0.110
14	R-leg	0.071	0.070	0.019	0.110
15	L-foot	0.049	0.010	0.019	0.450
16	R-foot	0.049	0.010	0.019	0.450
	Total	–	–	–	273.805

$D(i, j)$ is the heat transmitted by conduction to the neighboring layer within the same segment and is expressed by $D(i,j) = C_d(i,j)(T(i,j) - T(i,j+1))$ $\qquad$ (6.12). $C_d(i, j)$ is the thermal conductance between the node and its neighbor. The values shown in Table 6.7: $Cd(i, j)$ (W/°C).

i	Segment (i)	Core-muscle	Muscle-fat	Fat-skin

1	Head	1.601	13.224	16.008
2	Chest	0.616	2.100	9.164
3	Back	0.594	2.018	8.700
4	Pelvis	0.379	1.276	5.104
5	L-shoulder	0.441	2.946	7.308
6	R-shoulder	0.441	2.946	7.308
7	L-arm	0.244	2.227	7.888
8	R-arm	0.244	2.227	7.888
9	L-hand	2.181	6.484	5.858
10	R-hand	2.181	6.484	5.858
11	L-thigh	2.401	4.536	30.160
12	R-thigh	2.401	4.536	30.160
13	L-leg	1.891	2.656	7.540
14	R-leg	1.891	2.656	7.540
15	L-foot	8.120	10.266	8.178
16	R-foot	8.120	10.266	8.178

were used in this model.

$$D(i,j) = C_d(i,j)\big(T(i,j) - T(i,j+1)\big) \tag{6.12}$$

Table 6.7: $C_d(i, j)$ (W/°C).

i	Segment (i)	Core-muscle	Muscle-fat	Fat-skin
1	Head	1.601	13.224	16.008
2	Chest	0.616	2.100	9.164
3	Back	0.594	2.018	8.700
4	Pelvis	0.379	1.276	5.104
5	L-shoulder	0.441	2.946	7.308
6	R-shoulder	0.441	2.946	7.308
7	L-arm	0.244	2.227	7.888
8	R-arm	0.244	2.227	7.888
9	L-hand	2.181	6.484	5.858
10	R-hand	2.181	6.484	5.858
11	L-thigh	2.401	4.536	30.160
12	R-thigh	2.401	4.536	30.160
13	L-leg	1.891	2.656	7.540
14	R-leg	1.891	2.656	7.540
15	L-foot	8.120	10.266	8.178
16	R-foot	8.120	10.266	8.178

6.3.4   Heat loss by respiration

The heat loss by respiration is supposed to occur only at the core layer of the chest segment node (2, 1). *RES(2, 1)* is expressed by $RES(2,1) = \{0.0014(34 - t_a(1)) + 0.017(5.867 - p_a(1))\}\sum i = 116 \sum j = 14Q(i,j)$ (6.13):

$$RES(2,1) = \{0.0014(34 - t_a(1)) + 0.017(5.867 - p_a(1))\}\sum i = 116\sum j = 14Q(i,j) \quad (6.13)$$

where $t_a(1)$ and $p_a(1)$ are air temperature and vapor pressure at the head segment, respectively.

6.3.5   Evaporative heat loss at the skin surface

$E(i, 4)$ is evaporative heat loss at the skin surface and is expressed by $E(i,4) = E_b(i,4) + E_{sw}(1,4)$ (6.14). $E_b(i, 4)$ is the heat loss by water vapor diffusion through the skin. The skin diffusion is assumed to be 6% of $E_{max}(i)$, as shown in $E_b(i,4) = 0.061 - E_{sw}(i,4)E_{max}(i)$ (6.15). In the Stolwijk model, $E_b(i, 4)$ values were given as constants, which correspond to about 3–4% of $E_{max}(i)$. $E_{sw}(i, 4)$ is the heat loss by evaporation of sweat.

$$E(i,4) = E_b(i,4) + E_{sw}(1,4) \qquad (6.14)$$

$$E_b(i,4) = 0.061 - E_{sw}(i,4)E_{max}(i) \qquad (6.15)$$

where $E_{max}(i)$ is maximum evaporative heat loss and is shown by Eq. (16).

$$E_{max} = h_e(i)\big(p_{sk,s}(i) - p_a(i)A_n\big) \qquad (6.16)$$

$$h_e = LRi_{cl}(i)0.155I_{cl}(i) + \left(\frac{i_{cl}(i)}{h_c(i)f_{cl}}\right) \qquad (6.17)$$

where $h_e(i)$ is the evaporative heat transfer coefficient from the skin surface to the environment, expressed as a function of clothing vapor permeation efficiency $i_{cl}(i)$ by $h_e = LRi_{cl}(i)0.155I_{cl}(i) + \left(\frac{i_{cl}(i)}{h_c(i)f_{cl}}\right)$ (6.17). $p_{sk,s}(i)$ is the saturated vapor pressure on the skin surface, $p_a(i)$ the ambient vapor pressure.

In $h_e = LRi_{cl}(i)0.155I_{cl}(i) + \left(\frac{i_{cl}(i)}{h_c(i)f_{cl}}\right)$ (6.17), $i_{cl}(i)$ is the clothing thermal insulation factor for the individual segment, and thermal insulation plays an important role in determining clothing's thermal comfort and human thermal stress. Existing studies have demonstrated that clothing's thermal insulation is largely affected by wind speed, wind direction, human body movement, body posture and sweating, and such clothing physical

parameters as fabric properties (thickness, weight, density and air permeability), clothing area factor and clothing design features (covering the area, clothing combinations, and apertures, wearing style, air gap size and distribution, and air volume) of all aforementioned factors, the air layer underneath the garment has a much greater effect on clothing insulation than basic fabric properties (thickness and thermal conductivity). Many documented studies have shown that clothing's thermal insulation is affected by the fit. Generally, loose-fitting clothing provides higher thermal insulation than tight-fitting clothing [156] and $f_{cl}(i)$ is clothing area factor.

The procedure follows advice from the literature [157] and uses the analysis of photographs of clothed and nude Manikins. Pictures were taken at a 0° and 90° angle, and the surface areas of the clothed or the nude manikin were determined by analyzing the projection of the areas in Adobe Photoshop. The value for f_{cl} was then calculated as the ratio between clothed and nude areas:

$$f_{cl}(i) = \frac{A_{cl}(i)}{A_n(i)} \qquad (6.18)$$

In all laboratories, the thermal insulation of the nude manikin was determined as the value of the surface air insulation thermal resistance (I_a). The dry heat insulation I_T $\left(\frac{square\ meter\ .Kelvin}{watt} = m^2.K.W^{-1}\right)$ was determined as follows for the dry manikins (Loughborough and Lund Universities) [158].

$$I_T = Dry - heat\ insulation\ (resistance) = \frac{T_{skin} - T_{ambient}}{Dry\ heat\ loss} \qquad (6.19)$$

The intrinsic clothing insulation I_{cl} can be determined as:

$$I_{cl} = I_T - \frac{I_a}{f_{cl}} \qquad (m^2.K.W^{-1}) \qquad (6.20)$$

Conversion from SI units to Clo units can be performed by :

$$I(clo) = \frac{I(SI\ units)}{0.115} \qquad (6.21)$$

It is one of the main parameters as an input in all thermoregulatory models, which is related to garment position, $h_c(i)$ in $\boldsymbol{h_e = LRi_{cl}(i)0.155I_{cl}(i) + (\frac{i_{cl}(i)}{h_c(i)f_{cl}})}$ (6.17) is the convective heat transfer coefficient, and LR is the Lewis ratio.

6.3.6 Sensible heat exchange at the skin surface

$Q_t(i, 4)$ is the convective and radiant heat exchange rate between the skin surface and the environment, described by $\boldsymbol{Q_t(i,4) = h_t(i)\big(T(i,4) - t_o(i)\big)A_n(i)}$ (6.22). $h_t(i)$ is the total heat transfer coefficient from the skin surface to the environment and is expressed by $\boldsymbol{h_t(i) = 0.155I_{cl}(i) + \big(h_c(i) + h_r(i)\big)f_{cl}(i)}$ (6.23). $t_o(i)$ is the operative temperature and $h_r(i)$ is the radiant heat transfer coefficient. Convective and radiant heat transfer coefficients were derived from the thermal manikin experiment [159]:

$$Q_t(i,4) = h_t(i)\big(T(i,4) - t_o(i)\big)A_n(i) \qquad (6.22)$$

$$h_t(i) = 0.155I_{cl}(i) + \big(h_c(i) + h_r(i)\big)f_{cl}(i) \qquad (6.23)$$

6.3.7 Control system of multi-node model

The error signal $Err(i, j)$ is calculated by $\boldsymbol{Err(i,j) = T(i,j) - T_{set}(i,j)}$ (6.24). The set-point temperature $T_{set}(i, j)$, which plays a role of "control target temperature" in this study assumed that the first, second body is in the comfort temperature, so it is the initial temperature, is shown in Table 6.8.

$$Err(i,j) = T(i,j) - T_{set}(i,j) \qquad (6.24)$$

Table 6.8: *Tset(i,j)* (W/°C) , Central blood temperature = 36.7°C.

i	Segment	Core	Muscle	Fat	Skin	Inner surface fabric(A)	Outer surface fabric(A)
1	Head	36.9	36.1	35.8	35.6	35.6	35.6
2	Chest	36.5	36.2	34.5	33.6	31.5	29.2
3	Back	36.5	35.8	34.4	33.2	31.5	29.2
4	Pelvis	36.3	35.6	34.5	33.4	31.4	29
5	L-Shoulder	35.8	34.6	33.8	33.4	31.4	29
6	R-Shoulder	35.8	34.6	33.8	33.4	31.4	29
7	L-arm	35.5	34.8	34.7	34.6	32.5	30.5
8	R-arm	35.5	34.8	34.7	34.6	32.5	30.5
9	L-hand	35.4	35.3	35.3	35.2	35.2	35.2
10	R-hand	35.4	35.3	35.3	35.2	35.2	35.2
11	L-thigh	35.8	35.2	34.4	33.8	31.8	29
2	R-thigh	35.8	35.2	34.4	33.8	31.8	29
13	L-leg	35.6	34.4	33.9	33.4	31.6	29.3
14	R-leg	35.6	34.4	33.9	33.4	31.6	29.3
15	L-foot	35.1	34.9	34.4	33.9	33.9	33.9
16	R-foot	35.1	36.7	34.4	33.9	33.9	33.9

Warm signal *Wrm(i, j)* and cold signal *Cld(i, j)*, corresponding to warm and cold receptors, respectively, are defined by Eq. (25) (when *Err(i,j)>0*) and Eq. (26) (when *Err(i,j)<0*).

$$Wrm(i,j) = Err(i,j) , \qquad Cld(i,j) = 0 \qquad\qquad (6.25)$$

$$Cld(i,j) = -Err(i,j) , \qquad Wrm(i,j) = 0 \qquad\qquad (6.26)$$

6.3.8   Integrated signal

It is supposed that integrated sensor signals from skin thermoreceptors are used as the control variable. Integrated warm signal (Wrms, °C) and integrated cold signal (Clds, °C) are defined by *SKINR(i)* is the weighting coefficient for integration and is shown in Table 6.9.

$$Wrms = 116\big(SKINR(i) \times Wrm(i,4)\big) \qquad\qquad (6.27)$$

$$Clds = 116\big(SKINR(i) \times Cld(i,4)\big) \qquad\qquad (6.28)$$

Table 6.9: Weighting and distribution coefficients.

i	Segment (i)	SKINR(i)	SKINS(i)	SKINV(i)	SKINC(i)	Chit(i)
1	Head	0.070	0.081	0.32	0.022	0.020

2	Chest	0.149	0.146	0.098	0.065	0.258
3	Back	0.132	0.129	0.086	0.065	0.227
4	Pelvis	0.212	0.206	0.138	0.065	0.365
5	L-shoulder	0.023	0.051	0.031	0.022	0.004
6	R-shoulder	0.023	0.051	0.031	0.022	0.004
7	L-arm	0.012	0.026	0.016	0.022	0.026
8	R-arm	0.012	0.026	0.016	0.022	0.026
9	L-hand	0.092	0.016	0.061	0.152	0.000
10	R-hand	0.092	0.016	0.061	0.152	0.000
11	L-thigh	0.050	0.073	0.092	0.022	0.023
12	R-thigh	0.050	0.073	0.092	0.022	0.023
13	L-leg	0.025	0.036	0.023	0.022	0.012
14	R-leg	0.025	0.036	0.023	0.022	0.012
15	L-foot	0.017	0.018	0.050	0.152	0.000
16	R-foot	0.017	0.018	0.050	0.152	0.000
	Total	1.000	1.000	1.000	1.000	1.000

6.4 Thermoregulatory system

All control equations consist of three terms. One is related to head core signal, another with skin signal, and the third term is related. The thermoregulatory system consists of four control processes: vasodilation, vasoconstriction, perspiration, and shivering heat production.

6.4.1 Sensible heat loss from the skin

The heat loss from skin to the environment $Q_{nc}(i)$ is different for clothed and unclothed body segments. For the covered part of the body by clothing, heat transfer occurs from the skin through the air gap, the fabric layer, and the outer surface air layer of the clothing. Whereas for the unclothed body segments, heat transfer occurs through the boundary air layer of naked skin and is directly dissipated into the environment by natural convection and radiation.

Heat is transferred from the skin to the inner layer of clothing by conduction or convection through the air gap layer and the radiation between the skin and the inner surface of clothing. According to Catton's theory [160], for air in a vertical enclosure of thickness δ, heat transfers by conduction when Ra is less than 1000; when the value is more, natural convection will occur. The Nusselt number Nu_δ can be expressed as

$$Nu_\delta = \begin{cases} 1 & Ra \leq 10^3 \\ 0.22 \left(\dfrac{Pr}{0.2 + Pr} Ra \right)^{0.28} \left(\dfrac{H}{\delta} \right)^{-\frac{1}{4}} & 10^3 \leq Ra \leq 10^{10} \end{cases} \qquad (6.29)$$

133

Then, the heat transfer coefficient through the air gap $h_{nc}(i)$ can be deduced,

$$h_{nc}(i) = Nu_{\delta}\frac{k_a}{L_{nc(i)}} = 0.22\left(\frac{Pr}{0.2 + Pr}\frac{g\beta T((i,4) - T(i,5))H(i)^3}{\alpha v}\right)^{0.28}\left(\frac{H(i)}{L_{nc}}(i)\right)^{-1/4}\frac{k_a}{L_{nc}(i)} \quad (6.30)$$

Where,

Ra is the Rayleigh number,

Pr is the Prandtl number,

$H(i)$ is the height of the body segment i (Table 6.10),

ka is the thermal conductivity of air,

g is the gravitational acceleration,

β is the thermal coefficient of volume expansion,

α is the thermal diffusivity,

v is the kinematic viscosity.

Table 6.10: *H(i)* Height of the body segment.

i	Segment (*i*)	*H(i)* (m²)
1	Head	0.1894
2	Chest	0.5504
3	Back	0.5023
4	Pelvis	0.2134
5	L-shoulder	0.1750
6	R-shoulder	0.1750
7	L-arm	0.4735
8	R-arm	0.4735
9	L-hand	0.1950
10	R-hand	0.1950
11	L-thigh	0.4490
12	R-thigh	0.4490
13	L-leg	0.4280
14	R-leg	0.4280
15	L-foot	0.2565
16	R-foot	0.2565

Then the total sensible heat transfer from the skin to the inner layer of clothing can be expressed as:

$$Q_{nc}(i) = A_n(i) \left\{ h_{nc}(i)\big(T(i,4) - T(i,5)\big) + \frac{\sigma(T^4(i,4) - T^4(i,5)}{\left(\frac{1}{e_n} + \frac{1}{e_f}\right) - 1} \right\} \qquad (6.31)$$

Where,

σ is the StefanBoltzman constant,

e_n is the emissivity of skin,

e_f is the emissivity of the fabric.

The first term on the right side represents the thermal conduction or natural convection through the air gap, the second term, the radiant heat transfer between the skin and inner layer of clothing.

Influenced by the intrinsic thermal insulation of fabric R_f, the dry heat transfer through fabric is determined by:

$$Q_f(i) = A_{cl}(i) \frac{T(i,5) - T(i,6)}{R_f} \qquad (6.32)$$

The dry heat transfer from the outer layer of fabric to the environment is composed of convective and radiant heat:

$$Q_a(i) = A_{cl}(i) h_a(i)(T(i,6) - T_a + \sigma e_f(T^4(i,6) - T^4) \qquad (6.33)$$

Where the first term represents natural convection from the outer layer of clothing to the environment, the second term-radiant heat transfer, and $h_a(i)$ is the natural convective heat transfer coefficient, which can be calculated using Kyunghoon's theory [12]:

$$Nu = \frac{h_a(i)H(i)}{k_a} = 0.518 \left(\frac{c_p \rho^2 g \beta(T(i,6) - T_a)H^3(i)}{k_a \mu} \right)^{1/4} \qquad (6.34)$$

$$h_a(i) = 0.518 \left(\frac{c_p \rho^2 g \beta (T(i,6) - T_a) H^3(i)}{k_a \mu} \right)^{1/4} \tag{6.35}$$

Where,

C_p is the heat capacity at constant pressure,

ρ the density,

μ is the viscosity.

Based on the energy conversation law, we establish heat balance equations for the clothing's inner layer $A_n(i) L_{nc}(i) C_{nc}(i) \frac{dT(i,5)}{dt} = Q_{nc}(i) - Q_f(i)$ (6.5) and outer layer $A_{cl}(i) M_f(i) C_f(i) \frac{dT(i,6)}{dt} = Q_f(i) - Q_a(i)$ (6.6).

6.5 Results

By solving the heat balance equations of the human body and clothing, the effects of the air gap on human body heat transfer, as well as the interaction between the human, clothing, and the environment, can be predicted, which by comparing them with the standard of comfort we can predict in which value of air gap can provide comfort for the human body.

6.5.1   Effect of air gap thickness

For a standing human body, metabolic heat production is around 1.7Met (100.4 W/m2) [14]. The heat loss from a clothed human body under the reference condition is simulated based on five garments measured air gap thickness (Table 6.2), i.e. different value of 3D ease allowance. The apparent clothing temperatures in the chest and back of the body after a thirty-minute simulation are shown in Figure 6.7: Inner layer & Outer layer temperature of five garments size in chest segment.**Error! Reference source not found.**.
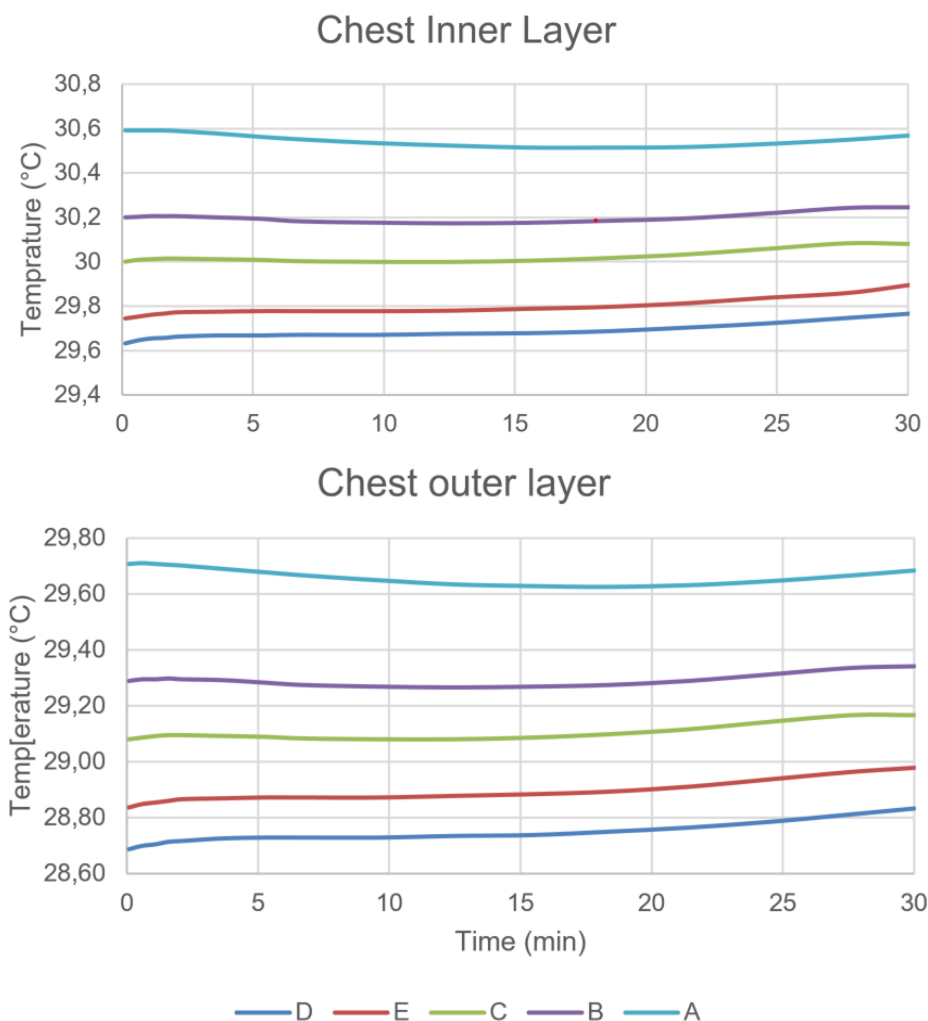
Figure 6.7: Inner layer & Outer layer temperature of five garments size in chest segment.

The temperature at the inner and outer clothing surfaces decreases with the air gap thickness when the garment size is smaller than 1.55 cm. The air gap behaves like insulating material, blocking heat transfer from the skin to the clothing surface. However, the temperature goes up when the garment size reaches E with an air gap thickness of 1.95 cm. From the simulated results, it can be observed that natural convection appears when the air gap thickness is bigger than 15 mm. The onset of natural convection increases heat transfer from the skin to the inner layer of clothing, elevating the apparent temperature of garment E. In the back segment, due to less parentage of fat and muscles, the only difference between back and chest is that the skin and

garment temperature is less than the chest (in indoor temperature, no high activity), but the changing behavior is the same (Figure 6.8).

Back Inner Layer
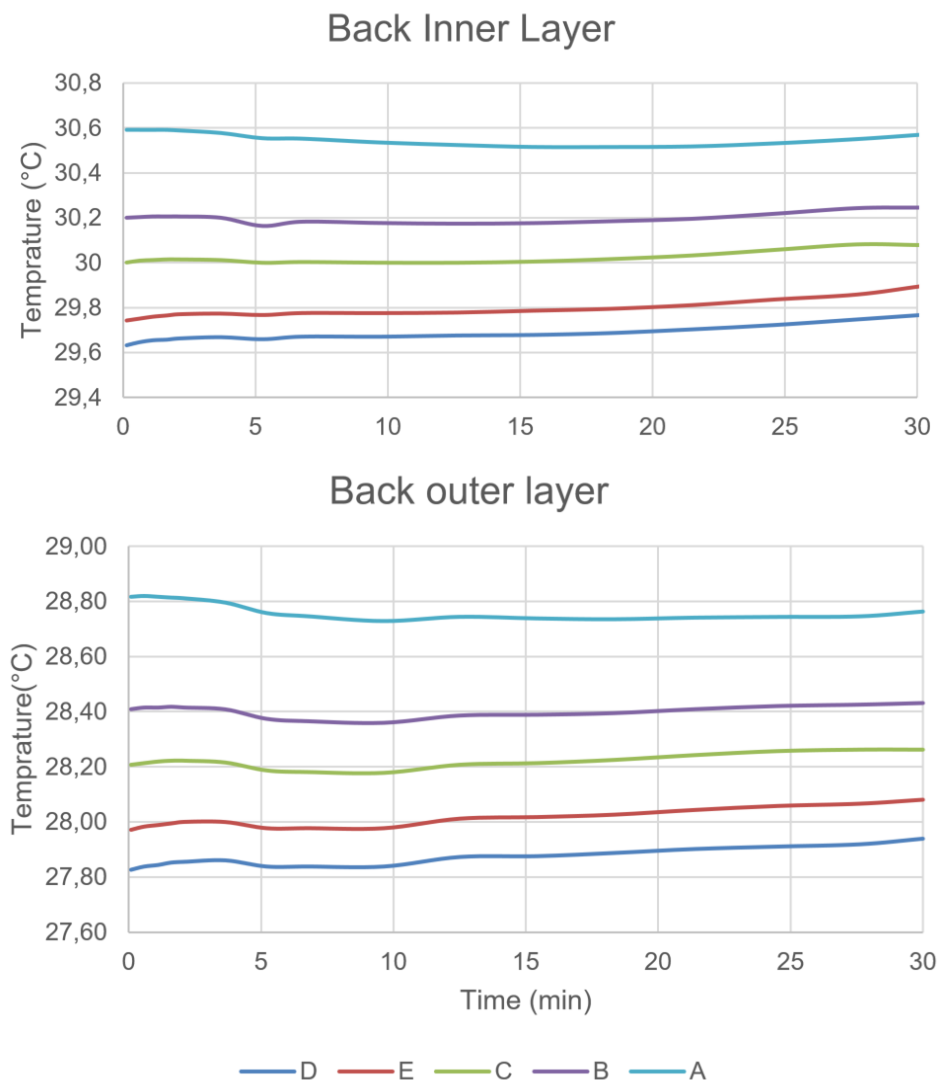
Back outer layer

Figure 6.8: Inner layer & Outer layer temperature of five garments size in back segment.

The effect of air gap thickness on sensible heat loss through the air gap is shown in Figure 6.9. It can be seen that the total dry heat flux densities from skin decrease until the garment size are larger than D, among which the conductive component decreases from 50% to 18% of the total sensible heat flux densities. In comparison, the radiant heat increases from 55% to 88%. Since the radiation is independent of the air gap thickness, the radiant heat loss through the air gap increases with an increase in the temperature difference between the skin and clothing surface. A large rate of reduction in the conductive component leads to a decrease in the total heat gain. The total and conductive heat flux of garment E increases due to natural convection.

Consequently, the radiant component decreases. It seems that the air gap thickness increases linearly with the garment size, from tight to loose, whereas heat transfer from the human body to the environment occurs irregularly. The air gap undergarment D can efficiently block heat loss from the human body, creating the lowest apparent temperature of clothing.
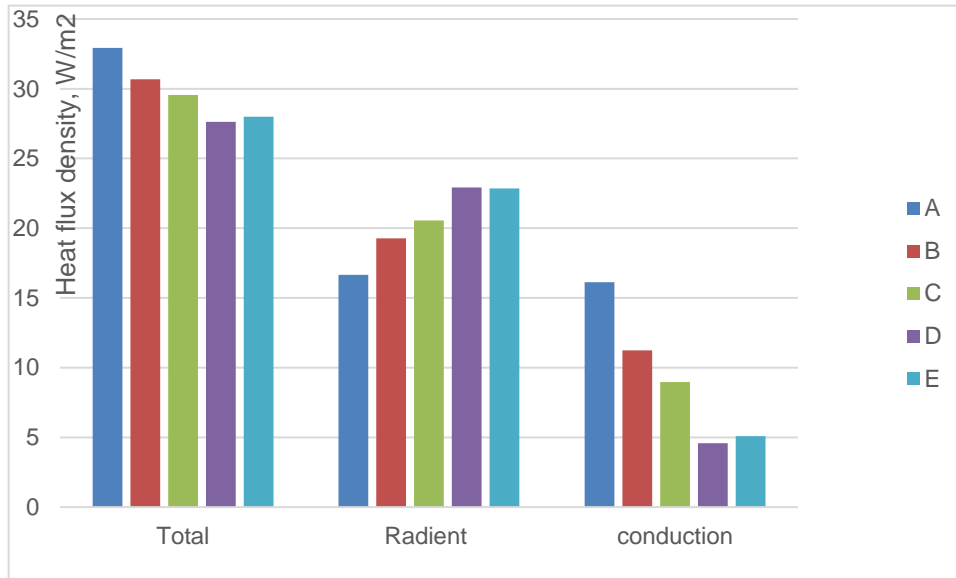
Figure 6.9: Dry heat loss of the different size of garments.

6.6 Conclusion

Air gaps between the body and the garment effects on heat loss from skin to the environment. In this chapter, we have proposed a thermoregulatory model, which is able to predict the temperature and heat for different size of garments. The main difference in garment and skin temperatures from segment to segment is the result of the uneven distribution of air layers under garments. This research describes the effect of the air gap on the heat transfer of a clothed human body. Thanks to the 3D adaptive garment, which can adjust in the different air gaps (ease allowance) through this model, the heat transfer between the human body and the temperature of skin and cloths (inner and outer layer) can be predicted. Even though heat transfer from the human body to the environment occurs irregularly, we can propose a suitable airgap in different ambient temperatures. Since also, the fabric properties is the input of the model, the model can predict the temperature and heat transfer from body to the garment for different material and fabric. Our result would be ingesting by testing with the thermal manikin and optimizing the size of garment.

General Conclusion and prospect

People with scoliosis don't have the chance that every one of us has, to be able to choose fashionable garment. Garment adapted to their atypical morphology, which can be found in real or virtual stores on the website, are garment very far from the spirit of fashion. The problem is that the 2D pattern making designer have no knowledge of their very atypical morphology, which has huge differences from person to person. Also, the block pattern representative of human morphology, the starting point for the creation of a fashion garment, is far from being adapted to the morphology of people suffering from scoliosis. Solving this sartorial problem necessarily requires tailoring in this specific case of morphology. For this, the objective of our study was to set up a set of adaptive morphological models connected to each other to create a tailor-made garment for people suffering from scoliosis.

The first steps were to develop a 3D model of the complex anatomical shape of human vertebrae and a 3D model of the upper part of the human skeleton. The first advantage of these models is to be configured to take into account the deformity and size of each person. Another advantage of these models is the precise detection of the different anthropometric points and morphological curves necessary for the garment creation. Obtaining the position of the extreme points of the scapulae and the tip of the breasts is essential when creating garment for women with strong deformities of the thoracic cage.

With regard to the spine model, model juxtaposition of the vertebrae, it was necessary to understand the functions of these, in particular the lumbar, dorsal and cervical parts. Using the different functionalities of the vertebrae, an innovative 3D design process has been introduced to develop the adaptive 3D model of the spine. Depending on the people's morphology, the developed adaptive model can be adjusted by introducing various values of radiological image data of the spine. From a database of medical images from the EOS scanner, a specific methodology was put in place to analyze and process the radiological images to extract the path of each vertebra and their dimensions.

For the 3D model of the upper part of the human skeleton, it is made up of the models of the thorax, clavicles and scapulae. The size, position and time course of each model is managed by the spine model. The path of the spine helps the deformation of the entire skeleton, but the size

of each bone must be partially adjusted so that the overall skeleton integrates perfectly with the dimension of the scanned human body envelope.

The 3D garment model is connected to the 3D model of the upper part of the human skeleton. This connection integrates the notion of 3D ease allowance of garment by creating a spatial interface between these two models. Since the starting point of fashion garment creation is the block pattern, we have chosen this type of garment representation. The new process of creating 3D garment based on the human skeleton can be seen as a variation of the draping techniques heavily used by fashion house designers who create directly on a mannequin or human body. This makes it possible to follow the people's morphology and take into account his atypical shape.

Thermal comfort is essential for people with disabilities. Feeling good about yourself with a fashionable item of clothing adapted to your morphology and offering quality thermal comfort plays a huge role in the well-being that is essential to the people. The air gap trapped between the human body and clothing influences heat loss from the skin to the environment. This air gap is not only controllable with the 3D ease allowance of our garment modeling strategy, but also zonable as required by the thermal model. We have therefore presented a transient thermal model of the human body / clothing / environment system, which can be used to predict the apparent temperature and heat loss of clothing of different sizes. This research sheds light on the effect of the air gap on the heat transfer of a clothed human body. However, further examination with experiences remains as future work. For example, a thermal mannequin and thermal infrared camera can be used to measure the heat loss and the apparent temperature of a clothed human body.

For future work, the image processing process needs to grow into having a comprehensive database that integrates both radiological images of the spine in the sagittal and coronal planes. This add-in automates the image processing process. Additionally, since all deep learning algorithms are extremely data dependent, increasing the number and quality of images to train the model will result in more accurate results. The extension of adaptive 3D modeling to the full skeleton is a possible direction to create a garment with sleeves, as well as pants. Thus, the thermoregulatory model will be able to develop for the other segments of the body thanks to the 3D ease allowance applied to the garment with sleeves or to the pants and to predict their comfort situation.

Bibliography

[1] Y. Hong, P. Bruniaux, X. Zeng, A. Curteza, and K. Liu, "Design and evaluation of personalized garment block for atypical morphology using the knowledge-supported virtual simulation method," *Text. Res. J.*, vol. 88, no. 15, 2018.

[2] Y. Hong, X. Zeng, P. Brunixaux, and Y. Chen, "Evaluation of Fashion Design Using Artificial Intelligence Tools," 2018.

[3] X. Ling, Y. Hong, and Z. Pan, "Development of a dress design knowledge base (DDKB) based on sensory evaluation and fuzzy logic," *Int. J. Cloth. Sci. Technol.*, vol. 33, no. 1, pp. 137–149, Jan. 2021.

[4] E. Melhem, A. Assi, R. El Rachkidi, and I. Ghanem, "EOS® biplanar X-ray imaging: concept, developments, benefits, and limitations," *J. Child. Orthop.*, vol. 10, no. 1, pp. 1–14, 2016.

[5] S. C. N. Hui *et al.*, "Radiation dose of digital radiography (DR) versus micro-dose x-ray (EOS) on patients with adolescent idiopathic scoliosis: 2016 SOSORT- IRSSD 'John Sevastic Award' Winner in Imaging Research," *Scoliosis Spinal Disord.*, vol. 11, no. 1, pp. 1–8, 2016.

[6] M. Kulinska, "Online 3d Unsupervised and 2d Supervised Classification in Clients?Pattern Recognition.," *J. Text. Sci. Eng.*, vol. 08, no. 05, 2018.

[7] K. C. Parsons, "Environmental ergonomics: A review of principles, methods and models," *Appl. Ergon.*, vol. 31, no. 6, 2000.

[8] H. J. Song, E. Design, A. Branch, and T. S. Division, "Overview of Human Thermal and Thermal Comfort at NASA," 2019.

[9] U. R. Liljenqvist, T. Allkemper, L. Hackenberg, T. M. Link, J. Steinbeck, and H. F. H. Halm, "Analysis of vertebral morphology in idiopathic scoliosis with use of magnetic resonance imaging and multiplanar reconstruction.," *J. Bone Joint Surg. Am.*, vol. 84, no. 3, pp. 359–368, Mar. 2002.

[10] Y. J. Liu, D. L. Zhang, and M. M. F. Yuen, "A survey on CAD methods in 3D garment design," *Comput. Ind.*, vol. 61, no. 6, pp. 576–593, 2010.

[11] B. Allen, B. Curless, and Z. Popović, "The space of human body shapes: Reconstruction and parameterization from range scans," in *ACM SIGGRAPH 2003 Papers, SIGGRAPH '03*, 2003.

[12] P. R. M. Jones and M. Rioux, "Three-dimensional Surface Anthropometry: Applications to the Human Body," *Opt. Lasers Eng.*, vol. 28, no. 2, 1997.

[13] "Physical status: The use and interpretation of anthropometry," *World Health Organization - Technical Report Series*, no. 854. 1995.

[14] N. Hantos, S. Iván, P. Balázs, and K. Palágyi, "Binary image reconstruction from a small number of projections and the morphological skeleton," *Ann. Math. Artif. Intell.*, vol. 75, no. 1–2, 2015.

[15] N. C. Bird and P. M. Mabee, "Developmental Morphology of the Axial Skeleton of the Zebrafish, Danio rerio (Ostariophysi: Cyprinidae)," *Developmental Dynamics*, vol. 228, no. 3. 2003.

[16] A. C. Burke, C. E. Nelson, B. A. Morgan, and C. Tabin, "Hox genes and the evolution of vertebrate axial morphology," *Development*, vol. 121, no. 2, 1995.

[17] E. Manfreda, P. Mitteroecker, F. L. Bookstein, and K. Schaefer, "Functional morphology of the first cervical vertebra in humans and nonhuman primates," *Anat. Rec. - Part B New Anat.*, vol. 289, no. 5, 2006.

[18] H. Lim, C. L. Istook, and N. L. Cassill, "Advanced mass customization in apparel," *J. Text. Apparel, Technol. Manag.*, vol. 6, no. 1, 2009.

[19] N. O. Burns, Leslie Davis; Mullet, Kathy K; Bryant, *The Business of Fashion: Designing, Manufacturing and Marketing*. Bloomsbury Publishing USA, 2016.

[20] C. C. L. Wang and M. M. F. Yuen, "Editorial: CAD methods in garment design," *CAD Comput. Aided Des.*, vol. 37, no. 6, pp. 583–584, 2005.

[21] M. A. Abtew *et al.*, "A systematic pattern generation system for manufacturing customized seamless multi-layer female soft body armour through dome-formation (moulding) techniques using 3D warp interlock fabrics," *J. Manuf. Syst.*, vol. 49, 2018.

[22] M. A. Abtew *et al.*, "Female seamless soft body armor pattern design system with innovative reverse engineering approaches," *Int. J. Adv. Manuf. Technol.*, vol. 98, no. 9–12, 2018.

[23] M. A. Abtew, P. Bruniaux, F. Boussu, C. Loghin, I. Cristian, and Y. Chen, "Development of comfortable and well-fitted bra pattern for customized female soft body armor through 3D design process of adaptive bust on virtual mannequin," *Comput. Ind.*, vol. 100, 2018.

[24] D. Protopsaltou, C. Luible, M. Arevalo, and N. Magnenat-Thalmann, "A body and Garment Creation Method for an Internet Based Virtual Fitting Room.," in *Advances in Modelling, Animation and Rendering*, 2002.

[25] A. Cichocka, P. Bruniaux, and I. Frydrych, "3D Garment Modelling - Creation of a virtual mannequin of the human body," *Fibres Text. East. Eur.*, vol. 22, no. 6, pp. 123–131, 2014.

[26] S. Y. Baek and K. Lee, "Parametric human body shape modeling framework for human-centered product design," *CAD Comput. Aided Des.*, vol. 44, no. 1, 2012.

[27] C. C. L. Wang, "Parameterization and parametric design of mannequins," *CAD Comput. Aided Des.*, vol. 37, no. 1, 2005.

[28] M. Javadi Toghchi *et al.*, "Virtual Mannequin Simulation for Customized Electromagnetic

Shielding Maternity Garment Manufacturing," *Designs*, vol. 3, no. 4, p. 53, 2019.

[29]   B. Azouz, M. Rioux, C. Shu, and R. Lepage, "Analysis of human shape variation using volumetric techniques," in *The 17th Annual Conference on Computer Animation and Social Agents (CASA2004)*, 2004.

[30]   A. M. Kubicka and J. Stefaniak, "Reliability of measurements performed on two dimensional and three dimensional computed tomography in glenoid assessment for instability," pp. 2581–2588, 2016.

[31]   Y. Hong, X. Zeng, P. Bruniaux, and K. Liu, "Interactive virtual try-on based three-dimensional garment block design for disabled people of scoliosis type," *Text. Res. J.*, vol. 87, no. 10, 2017.

[32]   Y. Hong, P. Bruniaux, X. Zeng, K. Liu, A. Curteza, and Y. Chen, "Visual-Simulation-Based Personalized Garment Block Design Method for Physically Disabled People with Scoliosis (PDPS)," *Autex Res. J.*, vol. 18, no. 1, 2018.

[33]   Y. Hong, X. Zeng, P. Bruniaux, K. Liu, and Y. Chen, "Collaborative 3D-To-2D tight-fitting garment pattern design process for scoliotic people," *Fibres Text. East. Eur.*, vol. 25, no. 5, 2017.

[34]   P. Thiriet *et al.*, *3D Human Anatomy Learning - Demonstration of 3D Tools used in Teaching: 3D Videos, Podcasts*. 2011.

[35]   G. Morvan *et al.*, "Standardized way for imaging of the sagittal spinal balance.," *European spine journal : official publication of the European Spine Society, the European Spinal Deformity Society, and the European Section of the Cervical Spine Research Society*, vol. 20 Suppl 5. 2011.

[36]   T. Illés, M. Tunyogi-Csapó, and S. Somoskeöy, "Breakthrough in three-dimensional scoliosis diagnosis: Significance of horizontal plane view and vertebra vectors," *Eur. Spine J.*, vol. 20, no. 1, 2011.

[37]   T. Illés and S. Somoskeöy, "The EOS^{TM} imaging system and its uses in daily orthopaedic practice," *Int. Orthop.*, vol. 36, no. 7, pp. 1325–1331, 2012.

[38]   R. Harmouche, F. Cheriet, H. Labelle, and J. Dansereau, "3D registration of MR and X-ray spine images using an articulated model," *Comput. Med. Imaging Graph.*, vol. 36, no. 5, 2012.

[39]   J. Kubicek, F. Tomanec, M. Cerny, D. Vilimek, M. Kalova, and D. Oczka, "Recent trends, technical concepts and components of computer-assisted orthopedic surgery systems: A comprehensive review," *Sensors (Switzerland)*, vol. 19, no. 23. 2019.

[40]   N. Vitković *et al.*, "Software Framework for the Creation and Application of Personalized Bone and Plate Implant Geometrical Models," *J. Healthc. Eng.*, vol. 2018, 2018.

[41]   H. K. Uhthoff, P. Poitras, and D. S. Backman, "Internal plate fixation of fractures: Short history and recent developments," *Journal of Orthopaedic Science*, vol. 11, no. 2. 2006.

[42]   Y. C. Lai, Y. W. Tarng, C. J. Hsu, W. N. Chang, S. W. Yang, and J. H. Renn, "Comparison of dynamic and locked compression plates for treating midshaft clavicle fractures," *Orthopedics*, vol. 35, no. 5, 2012.

[43]   R. Frigg, "Locking compression plate (LCP). An osteosynthesis plate based on the dynamic compression plate and the point contact fixator," *Injury*, vol. 32, pp. 63--66, 2001.

[44]   M. J. Gardner, D. L. Helfet, and D. G. Lorich, "Has locked plating completely replaced conventional plating?," *American journal of orthopedics (Belle Mead, N.J.)*, vol. 33, no. 9. 2004.

[45]   C. R. Berkin and D. V. Marshall, "Three-sided plate fixation for fractures of the tibial and femoral shafts. A follow-up note.," *J. Bone Joint Surg. Am.*, vol. 54, no. 5, 1972.

[46]   S. Donzelli *et al.*, "State of the art of current 3-D scoliosis classifications: a systematic review from a clinical perspective," *J. Neuroeng. Rehabil.*, vol. 12, no. 1, 2015.

[47]   V. H. Nguyen, M. A. Leroux, J. Badeaux, K. Zabjek, C. Coillard, and C. H. Rivard, "[Classification of left thoracolumbar scoliosis according to its radiologic morphology and its postural geometry].," *Ann. Chir.*, vol. 52, no. 8, 1998.

[48]   "Three-dimensional terminology of spinal deformity:A report presented to the scoliosis research society by the scoliosis research society working group on 3-d terminology of spinal deformity," *Spine (Phila. Pa. 1976).*, vol. 19, no. 2, 1994.

[49]   P. Poncet, J. Dansereau, and H. Labelle, "Geometric torsion in idiopathic scoliosis: Three-dimensional analysis and proposal for a new classification," *Spine (Phila. Pa. 1976).*, vol. 26, no. 20, 2001.

[50]   I. A. F. Stokes, L. C. Bigalow, and M. S. Moreland, "Measurement of axial rotation of vertebrae in scoliosis," *Spine (Phila. Pa. 1976).*, vol. 11, no. 3, 1986.

[51]   I. A. F. Stokes, L. C. Bigalow, and M. S. Moreland, "Three-dimensional spinal curvature in idiopathic scoliosis," *J. Orthop. Res.*, vol. 5, no. 1, 1987.

[52]   H. Akiyama, S. Nukui, M. Akamatu, Y. Hasegawa, O. Nishikido, and S. Inoue, "Effectiveness of spinal cord stimulation for painful camptocormia with Pisa syndrome in Parkinson's disease: A case report," *BMC Neurol.*, vol. 17, no. 1, 2017.

[53]   P. Barone, G. Santangelo, M. Amboni, M. T. Pellecchia, and C. Vitale, "Pisa syndrome in Parkinson's disease and parkinsonism: clinical features, pathophysiology, and treatment," *The Lancet Neurology*, vol. 15, no. 10. 2016.

[54]   L. Humbert, J. A. De Guise, B. Aubert, B. Godbout, and W. Skalli, "3D reconstruction of the spine from biplanar X-rays using parametric models based on transversal and longitudinal inferences," *Med. Eng. Phys.*, vol. 31, no. 6, pp. 681–687, Jul. 2009.

[55]   R. Lechner, D. Putzer, D. Dammerer, M. Liebensteiner, C. Bach, and M. Thaler, "Comparison of two- and three-dimensional measurement of the Cobb angle in scoliosis," *Int. Orthop.*, vol. 41, no. 5, 2017.

[56]   K. P. Lee and J. Hu, "XML Schema representation of DICOM structured reporting," *J. Am. Med. Informatics Assoc.*, vol. 10, no. 2, 2003.

[57]   B. H. Munro, "Statistical Methods for Health Care Research, 1. cilt," *Fourth Ed.*, vol. Fourth Edi, no. Fourth Ed., 2005.

[58]   N. Chung *et al.*, "Spinal phantom comparability study of Cobb angle measurement of scoliosis using digital radiographic imaging," *J. Orthop. Transl.*, vol. 15, 2018.

[59]   Z. Q. Zhao, P. Zheng, S. T. Xu, and X. Wu, "Object Detection with Deep Learning: A Review," *IEEE Trans. Neural Networks Learn. Syst.*, vol. 30, no. 11, pp. 3212–3232, 2019.

[60]   A. R. Pathak, M. Pandey, and S. Rautaray, "Application of Deep Learning for Object Detection," *Procedia Comput. Sci.*, vol. 132, no. Iccids, pp. 1706–1717, 2018.

[61]   R. L. Galvez, A. A. Bandala, E. P. Dadios, R. R. P. Vicerra, and J. M. Z. Maningo, "Object Detection Using Convolutional Neural Networks," in *IEEE Region 10 Annual International Conference, Proceedings/TENCON*, 2019, vol. 2018-October.

[62]   "VERTEBRA-FOCUSED LANDMARK DETECTION FOR SCOLIOSIS ASSESSMENT Jingru Yi, Pengxiang Wu, Qiaoying Huang, Hui Qu, Dimitris N. Metaxas Department of Computer Science, Rutgers University, Piscataway, NJ 08854, USA."

[63]   W. Ouyang *et al.*, "DeepID-Net: Deformable deep convolutional neural networks for object detection," in *Proceedings of the IEEE Computer Society Conference on Computer Vision and Pattern Recognition*, 2015, vol. 07-12-June-2015.

[64]   K. He, X. Zhang, S. Ren, and J. Sun, "Spatial Pyramid Pooling in Deep Convolutional Networks for Visual Recognition," *IEEE Trans. Pattern Anal. Mach. Intell.*, vol. 37, no. 9, 2015.

[65]   F. Yang, W. Choi, and Y. Lin, "Exploit All the Layers: Fast and Accurate CNN Object Detector with Scale Dependent Pooling and Cascaded Rejection Classifiers," in *Proceedings of the IEEE Computer Society Conference on Computer Vision and Pattern Recognition*, 2016, vol. 2016-December.

[66]   G. Gillen, *Stroke rehabilitation: a function-based approach*. Elsevier Health Sciences, 2015.

[67]   G. Nilsen, Dawn M and Donato, Susan M and Pulaski, Karen Halliday and Gillen, "Standing Postural Control: Supporting Functional Independence," *Stroke Rehabil. E-b. A Funct. Approach*, p. 381, 2020.

[68]   B. E. Fliegel and R. G. Menezes, *Anatomy, Thorax, Cervical Rib*. 2020.

[69]   Ł. Spadliński *et al.*, "The Epidemiological, Morphological, and Clinical Aspects of the Cervical Ribs in Humans," *BioMed Research International*, vol. 2016. 2016.

[70]   S. Mhatre, M. Muranjan, and S. Karande, "Short rib thoracic dysplasia without polydactyly due to novel variant in IFT172 gene," *Journal of Postgraduate Medicine*, vol. 66, no. 4.

2020.

[71] G. Hammer, S. Hall, and P. J. Davis, "Anesthesia for General Abdominal, Thoracic, Urologic, and Bariatric Surgery," in *Smith's Anesthesia for Infants and Children*, 2011.

[72] J. R. Clinkingbeard, "Anatomy of the Human Body by Henry Gray 29th ed," *Phys. Ther.*, vol. 54, no. 2, 1974.

[73] P. Lewis, TL and Burnett, B and Tunstall, RG and Abrahams, "Complementing anatomy education using three-dimensional anatomy mobile software applications on tablet computers," *Clin. Anat.*, vol. 27, no. 3, pp. 313--320, 2014.

[74] A. Fedorov *et al.*, "3D Slicer as an image computing platform for the Quantitative Imaging Network," *Magn. Reson. Imaging*, vol. 30, no. 9, pp. 1323–1341, Nov. 2012.

[75] R. M. Carew, R. M. Morgan, and C. Rando, "A Preliminary Investigation into the Accuracy of 3D Modeling and 3D Printing in Forensic Anthropology Evidence Reconstruction," *J. Forensic Sci.*, vol. 64, no. 2, 2019.

[76] N. Magnenat-Thalmann *et al.*, *Modeling and simulating bodies and garments*. 2010.

[77] K. Liu *et al.*, "3D interactive garment pattern-making technology," *CAD Comput. Aided Des.*, vol. 104, 2018.

[78] D. Protopsaltou, C. Luible, M. Arevalo, and N. Magnenat-Thalmann, "A body and Garment Creation Method for an Internet Based Virtual Fitting Room.," in *Advances in Modelling, Animation and Rendering*, Springer London, 2002, pp. 105–122.

[79] M. Kulinska, P. Bruniaux, A. Ainamo, X. Zeng, and Y. Chen, "Virtual mannequins and garment parametrization," in *Uncertainty Modelling in Knowledge Engineering and Decision Making - Proceedings of the 12th International FLINS Conference, FLINS 2016*, 2016, pp. 984–989.

[80] D. Protopsaltou, C. Luible, M. Arevalo, and N. Magnenat-Thalmann, "A body and Garment Creation Method for an Internet Based Virtual Fitting Room.," in *Advances in Modelling, Animation and Rendering*, 2002, pp. 105–122.

[81] M. Kulinska, "Digital tools for developing customized co-design platform with integration of comfort and fashion," Lille University, 2018.

[82] K. Slater, *Human comfort*. Springfield, Ill., USA: CC Thomas, 1985.

[83] P.O. Fanger, "Analysis and Applications in Environmental Engineering," *Danish Tech. Press*, 1970.

[84] STOLWIJK JAJ, "Mathematical model of physiological temperature regulation in man," *NASA Contract. Reports*, 1971.

[85] D. Fiala, K. J. Lomas, and M. Stohrer, "A computer model of human thermoregulation for a wide range of environmental conditions: The passive system," *J. Appl. Physiol.*, vol. 87,

no. 5, 1999.

[86]   D. Fiala, K. J. Lomas, and M. Stohrer, "Computer prediction of human thermoregulatory and temperature responses to a wide range of environmental conditions," *Int. J. Biometeorol.*, vol. 45, no. 3, 2001.

[87]   K. Parsons, *Human thermal environments: the effects of hot, moderate, and cold environments on human health, comfort and performance*. CRC press, 2007.

[88]   I. Holmér, H. Nilsson, G. Havenith, and K. Parsons, "Clothing convective heat exchange-proposal for improved prediction in standards and models," in *Annals of Occupational Hygiene*, 1999, vol. 43, no. 5.

[89]   K. C. Parsons, G. Havenith, I. Holmér, H. Nilsson, and J. Malchaire, "The effects of wind and human movement on the heat and vapour transfer properties of clothing," *Ann. Occup. Hyg.*, vol. 43, no. 5, 1999.

[90]   J. L. Spencer-Smith, "Physical basis of clothing comfort. III. Water vapour transfer through dry clothing assemblies." 1977.

[91]   B. Cain and B. Farnworth, "Two New Techniques for Determining the Thermal Radiative Properties of Thin Fabrics," *J. Therm. Envel. Build. Sci.*, vol. 9, no. 4, 1986.

[92]   F. Galbusera and T. Bassani, "The Spine: A Strong, Stable, and Flexible Structure with Biomimetics Potential," *Biomimetics*, vol. 4, no. 3, p. 60, 2019.

[93]   T. Takao *et al.*, "A radiographic evaluation of facet sagittal angle in cervical spinal cord injury without major fracture or dislocation," *Spinal Cord*, vol. 55, no. 5, pp. 515–517, 2017.

[94]   Nobelprize.org, "The Nobel Prize in Physics," 1992. [Online]. Available: http://nobelprize.org/nobel_prizes/%0Aphysics/laureates/1992/index.html. [Accessed: 19-Dec-2011].

[95]   D. Mitton, C. Landry, S. Véron, W. Skalli, F. Lavaste, and J. A. De Guise, "3D reconstruction method from biplanar radiography using non-stereocorresponding points and elastic deformable meshes," *Med. Biol. Eng. Comput.*, vol. 38, no. 2, pp. 133–139, 2000.

[96]   A. Le Bras, S. Laporte, D. Mitton, J. A. De Guise, and W. Skalli, "3D detailed reconstruction of vertebrae with low dose digital stereoradiography," in *Studies in Health Technology and Informatics*, 2002, vol. 91.

[97]   A. Mitulescu, I. Semaan, J. A. De Guise, P. Leborgne, and C. Adamsbaum, "Validation of the non-stereo corresponding points stereoradiographic 3D reconstruction technique," *Med. Biol. Eng. Comput.*, vol. 39, no. 2, 2001.

[98]   G. Kalifa *et al.*, "Evaluation of a new low-dose digital X-ray device: First dosimetric and clinical results in children," *Pediatr. Radiol.*, vol. 28, no. 7, 1998.

[99] A. L. Fradkov, "Early history of machine learning," in *IFAC-PapersOnLine*, 2020, vol. 53, no. 2.

[100] T. Mildenberger, "Stephen Marsland: Machine learning. An algorithmic perspective," *Stat. Pap.*, vol. 55, no. 2, 2014.

[101] D. Silver *et al.*, "Mastering the game of Go with deep neural networks and tree search," *Nature*, vol. 529, no. 7587, 2016.

[102] Z. Chen and X. Huang, "End-To-end learning for lane keeping of self-driving cars," in *IEEE Intelligent Vehicles Symposium, Proceedings*, 2017.

[103] H. Kaiming, Z. Xiangyu, R. Shaoqing, and S. Jian, "Delving Deep into Rectifiers: Surpassing Human-Level Performance on ImageNet Classification Kaiming," *Biochem. Biophys. Res. Commun.*, vol. 498, no. 1, 2018.

[104] S. S. Liu and Y. T. Tian, "Facial expression recognition method based on Gabor wavelet features and fractional power polynomial kernel PCA," in *Lecture Notes in Computer Science (including subseries Lecture Notes in Artificial Intelligence and Lecture Notes in Bioinformatics)*, 2010, vol. 6064 LNCS, no. PART 2.

[105] A. Waibel, M. T. Vo, P. Duchnowski, and S. Manke, "Multimodal interfaces," *Artif. Intell. Rev.*, vol. 10, no. 3–4, 1996.

[106] M. Pazzani and D. Billsus, "Learning and Revising User Profiles: The Identification of Interesting Web Sites," *Mach. Learn.*, vol. 27, no. 3, 1997.

[107] P. K. Chan and S. J. Stolfo, "Toward Scalable Learning with Non-uniform Class and Cost Distributions : A Case Study in Credit Card Fraud Detection 1 Introduction," *n Proc. Fourth In- ternational Conf. Knowl. Discov. Data Min.*, 1998.

[108] T. S. Guzella and W. M. Caminhas, "A review of machine learning approaches to Spam filtering," *Expert Systems with Applications*, vol. 36, no. 7. 2009.

[109] C. L. Huang, M. C. Chen, and C. J. Wang, "Credit scoring with a data mining approach based on support vector machines," *Expert Syst. Appl.*, vol. 33, no. 4, 2007.

[110] N. Srinivasa and J. M. Cruz-Albrecht, "Neuromorphic adaptive plastic scalable electronics: Analog learning systems," *IEEE Pulse*, vol. 3, no. 1, 2012.

[111] G. Weiss, *Multiagent Systems: A Modern Approach to Distributed Artificial Intelligence*, vol. 3, no. 2. 1999.

[112] W. Liu *et al.*, "SSD: Single shot multibox detector," in *Lecture Notes in Computer Science (including subseries Lecture Notes in Artificial Intelligence and Lecture Notes in Bioinformatics)*, 2016, vol. 9905 LNCS.

[113] P. F. Felzenszwalb, R. B. Girshick, D. McAllester, and D. Ramanan, "Object detection with discriminatively trained part-based models," *IEEE Trans. Pattern Anal. Mach. Intell.*, vol. 32, no. 9, 2010.

[114] R. Girshick, J. Donahue, T. Darrell, and J. Malik, "Rich feature hierarchies for accurate object detection and semantic segmentation," in *Proceedings of the IEEE Computer Society Conference on Computer Vision and Pattern Recognition*, 2014.

[115] S. Ren, K. He, R. Girshick, and J. Sun, "Faster R-CNN: Towards real-time object detection with region proposal networks," in *Advances in Neural Information Processing Systems*, 2015, vol. 2015-January.

[116] K. Van De Sande *et al.*, "Segmentation as Selective Search for Object Recognition Main objectives • Object recognition in " large " datasets," *Int. J. Comput. Vis.*, vol. 104, no. 2, 2013.

[117] J. Dai, Y. Li, K. He, and J. Sun, "R-FCN: Object detection via region-based fully convolutional networks," in *Advances in Neural Information Processing Systems*, 2016.

[118] S. Ren, K. He, R. Girshick, and J. Sun, "Faster R-CNN: Towards real-time object detection with region proposal networks," in *Advances in Neural Information Processing Systems*, 2015, vol. 2015-Janua, pp. 91–99.

[119] Z. Cai, Q. Fan, R. S. Feris, and N. Vasconcelos, "A unified multi-scale deep convolutional neural network for fast object detection," in *Lecture Notes in Computer Science (including subseries Lecture Notes in Artificial Intelligence and Lecture Notes in Bioinformatics)*, 2016, vol. 9908 LNCS.

[120] K. Simonyan and A. Zisserman, "Very deep convolutional networks for large-scale image recognition," *3rd Int. Conf. Learn. Represent. ICLR 2015 - Conf. Track Proc.*, pp. 1–12, 2015.

[121] J. Mahadeokar and G. Pesavento, "Open Sourcing a Deep Learning Solution for Detecting NSFW Images," *Yahoo Eng.*, vol. 24, 2016.

[122] S. Xie, R. Girshick, P. Dollár, Z. Tu, and K. He, "Aggregated residual transformations for deep neural networks," in *Proceedings - 30th IEEE Conference on Computer Vision and Pattern Recognition, CVPR 2017*, 2017, vol. 2017-Janua.

[123] V. Fung, "An Overview of ResNet and its Variants," *Towar. Data Sci.*, 2017.

[124] A. Newell, K. Yang, and J. Deng, "Stacked hourglass networks for human pose estimation," in *Lecture Notes in Computer Science (including subseries Lecture Notes in Artificial Intelligence and Lecture Notes in Bioinformatics)*, 2016, vol. 9912 LNCS.

[125] B. Sapp and B. Taskar, "MODEC: Multimodal decomposable models for human pose estimation," in *Proceedings of the IEEE Computer Society Conference on Computer Vision and Pattern Recognition*, 2013.

[126] P. Felzenszwalb, D. McAllester, and D. Ramanan, "A discriminatively trained, multiscale, deformable part model," in *26th IEEE Conference on Computer Vision and Pattern Recognition, CVPR*, 2008.

[127] L. Pishchulin, M. Andriluka, P. Gehler, and B. Schiele, "Strong appearance and expressive

spatial models for human pose estimation," in *Proceedings of the IEEE International Conference on Computer Vision*, 2013.

[128] L. Bourdev and J. Malik, "Poselets: Body part detectors trained using 3D human pose annotations," 2010.

[129] S. Johnson and M. Everingham, "Learning effective human pose estimation from inaccurate annotation," in *Proceedings of the IEEE Computer Society Conference on Computer Vision and Pattern Recognition*, 2011.

[130] Y. Yang and D. Ramanan, "Articulated human detection with flexible mixtures of parts," *IEEE Trans. Pattern Anal. Mach. Intell.*, vol. 35, no. 12, 2013.

[131] L. Ladicky, P. H. S. Torr, and A. Zisserman, "Human pose estimation using a joint pixel-wise and part-wise formulation," in *Proceedings of the IEEE Computer Society Conference on Computer Vision and Pattern Recognition*, 2013.

[132] K. He, X. Zhang, S. Ren, and J. Sun, "Deep residual learning for image recognition," in *Proceedings of the IEEE Computer Society Conference on Computer Vision and Pattern Recognition*, 2016, vol. 2016-December.

[133] O. Ronneberger, P. Fischer, and T. Brox, "U-net: Convolutional networks for biomedical image segmentation," in *Lecture Notes in Computer Science (including subseries Lecture Notes in Artificial Intelligence and Lecture Notes in Bioinformatics)*, 2015, vol. 9351.

[134] J. Yi, P. Wu, M. Jiang, Q. Huang, D. J. Hoeppner, and D. N. Metaxas, "Attentive neural cell instance segmentation," *Med. Image Anal.*, vol. 55, 2019.

[135] H. Law and J. Deng, "Cornernet: Detecting objects as paired keypoints," in *Lecture Notes in Computer Science (including subseries Lecture Notes in Artificial Intelligence and Lecture Notes in Bioinformatics)*, 2018, vol. 11218 LNCS.

[136] X. Zhou, J. Zhuo, and P. Krahenbuhl, "Bottom-up object detection by grouping extreme and center points," in *Proceedings of the IEEE Computer Society Conference on Computer Vision and Pattern Recognition*, 2019, vol. 2019-June.

[137] D. P. Kingma and J. L. Ba, "Adam: A method for stochastic optimization," in *3rd International Conference on Learning Representations, ICLR 2015 - Conference Track Proceedings*, 2015.

[138] S. Efrat, "Development of a method for generating patterns for garments that conform to the shape of the human body," 1982.

[139] Y. Hong, X. Zeng, P. Bruniaux, A. Curteza, M. Stelian, and Y. Chen, "Garment opening position evaluation using kinesiological analysis of dressing activities: case study of physically disabled people with scoliosis (PDPS)," *Text. Res. J.*, vol. 88, no. 20, 2018.

[140] "Thermal environmental conditions for human occupancy," *ASHRAE Stand.*, no. STANDARD 55, 2010.

[141] S. Tanabe, H. Zhang, E. A. Arens, T. L. Madsen, and F. S. Bauman, "Evaluating thermal environments by using a thermal manikin with controlled skin surface temperature," in *ASHRAE Transactions*, 1994, vol. 100, no. 1.

[142] B. W. Jones, "Capabilities and limitations of thermal models for use in thermal comfort standards," in *Energy and Buildings*, 2002.

[143] GAGGE AP, STOLWIJK JAJ, and NISHI Y, "Effective temperature scale based on a simple model of human physiological regulatory response," *ASHRAE Trans.*, vol. 77, no. pt 1 paper 2192 p 247-63, 1971.

[144] ISO, "ISO 7730:1984 Moderate thermal environments — Determination of the PMV and PPD indices and specification of the conditions for thermal comfort," *ISO*, 1984.

[145] D. Fiala, G. Havenith, P. Bröde, B. Kampmann, and G. Jendritzky, "UTCI-Fiala multi-node model of human heat transfer and temperature regulation," *Int. J. Biometeorol.*, vol. 56, no. 3, 2012.

[146] K. Parsons, *Human thermal environments: The effects of hot, moderate, andcold environments on human health,comfort, and performance, third edition*. 2014.

[147] K. P. Ivanov, "The development of the concepts of homeothermy and thermoregulation," in *Journal of Thermal Biology*, 2006, vol. 31, no. 1-2 SPEC. ISS.

[148] H. Zhang, C. Huizenga, E. Arens, and T. Yu, "Considering individual physiological differences in a human thermal model," *J. Therm. Biol.*, vol. 26, no. 4–5, 2001.

[149] A. P. Gagge, A. P. Fobelets, and L. G. Berglund, "STANDARD PREDICTIVE INDEX OF HUMAN RESPONSE TO THE THERMAL ENVIRONMENT.," in *ASHRAE Transactions*, 1986, vol. 92, no. pt 2B.

[150] M. McQuerry, E. DenHartog, and R. Barker, "Analysis of air gap volume in structural firefighter turnout suit constructions in relation to heat loss," *Text. Res. J.*, vol. 88, no. 21, pp. 2475–2484, Nov. 2018.

[151] G. Song, "Cothing air gap layers and thermal protective performance in single layer garment," *J. Ind. Text.*, vol. 36, no. 3, 2007.

[152] J. Li, Z. Zhang, and Y. Wang, "The relationship between air gap sizes and clothing heat transfer performance," *J. Text. Inst.*, vol. 104, no. 12, 2013.

[153] K. Min, Y. Son, C. Kim, Y. Lee, and K. Hong, "Heat and moisture transfer from skin to environment through fabrics: A mathematical model," *Int. J. Heat Mass Transf.*, vol. 50, no. 25–26, 2007.

[154] J. J. Vos, T. W. L. Scheeren, S. A. Loer, A. Hoeft, and J. K. G. Wietasch, "Do intravascular hypo- and hypervolaemia result in changes in central blood volumes?," *Br. J. Anaesth.*, vol. 116, no. 1, 2016.

[155] C. Huizenga, Z. Hui, and E. Arens, "A model of human physiology and comfort for

assessing complex thermal environments," *Build. Environ.*, vol. 36, no. 6, pp. 691–699, Jul. 2001.

[156] H. Akbari, G. Havenith, and A. Al-Sahhaf, "A database of static clothing thermal insulation and vapor permeability values of non-western ensembles for use in ASHRAE Standard 55, ISO 7730, and ISO 9920: Discussion," *ASHRAE Conference-Papers*, vol. 121. 2015.

[157] B. W. Olesen, "A New Simpler Method for Estimating the Thermal lnsulation of a Clothing Ensemble," *ASHRAE Trans.*, vol. HI-85-09, no. 4, 1985.

[158] Y. OSADA, "Relationship between clothing ventilation and thermal insulation. Bouskill, L. M., Havenith, G., Kuklane, K., Parsons, K. C., and Withey, W. R. AIHA J., 63(3):262-268, 2002.(Abstracts of foreign literature)," *J. Hum. living Environ.*, vol. 10, no. 2, 2003.

[159] M. OGURO, E. ARENS, R. de DEAR, H. ZHANG, and T. KATAYAMA, "CONVECTIVE HEAT TRANSFER COEFFICIENTS AND CLOTHING INSULATIONS FOR PARTS OF THE CLOTHED HUMAN BODY UNDER AIRFLOW CONDITIONS," *J. Archit. Plan. (Transactions AIJ)*, vol. 67, no. 561, 2002.

[160] W. R. Catton, "Probable collective responses to ecological scarcity: How Violent?," *Sociol. Perspect.*, vol. 27, no. 1, 1984.

Appendix

Published and submitted papers:

Communications with Proceedings in an International or National Conferences

S. Mosleh, P. Bruniaux, G.Tartare, "Creating 3D garment pattern from adaptive digital modelling of human spine for persons with spinal disability", *Textile Science and Economy 2019 French - Croatian Forum*, Zagreb, Croatia, January 23rd to 24th, 2019.

Communications In An International Or National Conferences

S. Mosleh, P. Bruniaux, G.Tartare, "A method of localization and segmentation of vertebrae in the spine EOS image", *IHIET'2019, 1st International Conference on Human Interaction and Emerging Technologies*, Nice, France, August 22rd to 24th, 2019 .

Articles in international or national peer-reviewed journals listed in international databases

S. Mosleh, A. Mulat, P. Bruniaux, G.Tartare, Y. Yukang, Y. Chen, "3D Digital Adaptive Thorax Modelling of Peoples with Spinal Disabilities: Applications for Performance Clothing Design", *Applied Sciences*. Vol. 11, no. 10: 4545. 2021.

S. Mosleh, A. Mulat, P. Bruniaux, G.Tartare, Y. Chen, "Developing an Adaptive 3D Vertebrae Model of Scoliosis Patients for Customize Garment Design", *Applied Sciences*. Vol. 11, no. 7: 3171. 2021.

S. Mosleh, A. Mulat, P. Bruniaux, G.Tartare, Y. Chen, "Customised block pattern generation for Scoliosis Patients from adaptive Model" prepared to be **submitted** in *Textile Research Journal*.